eXPRESS Polymer Letters Vol.3, No.3 (2009) 137
Available online at www.expresspolymlett.com
DOI: 10.3144/expresspolymlett.2009.17

Editorial corner – a personal view
Electrospinning – an easy way to produce nanomaterials

*Z. Sun**

Center for Micro-Engineered Materials, University of New Mexico, 1001 University Blvd. SE, Albuquerque, NM, 87106 USA

Electrospinning process is not a new technology. It was patented by John F. Cooley in 1902 (US Patent #692,631) but did not find much application at that time. With the development of polymer nanomaterials in the early 1990s, it has re-emerged as a useful technique because of its straightforward setup and execution.

Electrospinning produces polymer nanofibers, fibers with diameters in the range from nanometers to a few microns. High voltage is applied to a polymer solution stored in a syringe. A grounded electrode – a metal plate – is placed 5–20 cm away from the syringe needle. The polymer solution flows from the needle tip and is stretched into a Taylor cone due to the high electric field between the electrodes. The entangled polymer chains in the solution form a single liquid jet. Electrostatic forces within the jet cause bending instabilities that whip the jet from side to side. Concomitant evaporation of solvent allow this jet to be stretched resulting in the fabrication of uniform fibers with nanometer-scale diameters, and the lengths from centimeter to meter scale. Nanofibers are hard to be produced without the bending instability stage in electrospinning process.

In general, most polymers can be electrospun provided a suitable solvent is chosen for preparing the polymer solution. The more sensitive parameters determining the quality of the final product are strength of electric field, solution feed rate and polymer solution/viscosity, surface tension and dielectric constant, with needle diameter having less influence. Some polymers like polyethylene, poly(methyl methacrylate) can be electrospun via a melt electrospinning process but this typically generates thicker fibers. Electrospinning is not limited to the polymer field and has been extended into sol-gel systems to fabricate oxide nanofibers of silica and titania. Even some metal precursors have been added to polymer solutions to yield metal nanofibers of iron, copper, cobalt and nickel.

Nanofibers possess large surface area to unit mass ratio. Thus, non-woven fabrics of these nanofibers can be used, for example, in the filtration of submicron particles in separation industries and in biomedical applications, such as wound dressing in medical industry, tissue engineering scaffolds and artificial blood vessels. Electrospun fibers have potential as enzyme attachment surfaces and as carriers for catalytic nanoparticles.

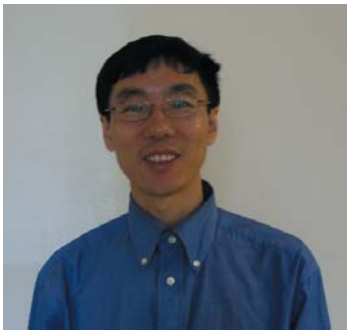

Dr. Zaicheng Sun
Member of International Advisory Board

*Corresponding author, e-mail: zaichengsun@hotmail.com

eXPRESS Polymer Letters Vol.3, No.3 (2009) 138–144
Available online at www.expresspolymlett.com
DOI: 10.3144/expresspolymlett.2009.18

A new approach to the estimation of surface free energy based on Vickers microhardness data

*M. Staneva**, *E. Nedkov*

Institute of Polymers, Bulgarian Academy of Sciences, Acad. G. Bonchev Street, bl. 103A, Sofia 1113, Bulgaria

Received 4 December 2008; accepted in revised form 24 January 2009

Abstract. A relation between surface free energy (σ^{MHV}) and Meyer's lines cut-values has been established using Vickers microhardness (MHV) method and empirical physical laws. This relation allows the calculation of σ^{MHV} only from MHV data. The parameters required are Meyer's lines cut-values and the mean value of diagonal length of the impression at different loads applied (d_{real}^{mean}). Our study of 12 samples of ultra high molecular weight polyethylene (PE-UHMW) showed that the new approach is applicable when the slope value of Meyer's lines equals 2 (i.e. $n = 2$). A γ-^{60}Co source was used for the irradiation of 11 samples (one of the samples investigated is un-irradiated) at room temperature in air. Doses of 1, 2, 5, 10, 20, 50, 100, 200, 500, 1000 and 1500 kGy were applied. The values of σ^{MHV} obtained are in a good agreement with the literature. The dependence of σ^{MHV} on the dose applied strictly corresponds to the radiation effects theory. MHV was measured at seven different loads – 0.0123, 0.0245, 0.049, 0.098, 0.196, 0.392, 0.785 N at a loading time of 30 s.

Keywords: *material testing, Vickers microhardness (MHV), surface free energy*

1. Introduction

1.1. Fundamentals of Vickers microhardness (MHV) method

The microhardness of a polymeric material – resistance to local deformation – is a complex property related to mechanical properties such as modulus, strength, elasticity and plasticity [1].

MHV test uses a square diamond pyramid, with angles α between non-adjacent faces of the pyramid of 136° ([1], p. 3). The microhardness is estimated by Equation (1):

$$MHV = \frac{2 \cdot P \cdot \sin\left(\frac{\alpha}{2}\right)}{d^2} = 1.8544 \cdot \frac{P}{d^2} \tag{1}$$

where P is the force (the load applied), [N]; d is the mean diagonal length of the impression after removing the indenter (pyramid), [mm]; MHV – in [MPa].

1.2. Fundamentals of the approach – description of deriving the equation for surface free energy (σ^{MHV})

Our new approach to estimating σ^{MHV} is based on Meyer's power law represented by Meyer's line [2], as given by Equation (2a):

$$\log P = \log a + n \cdot \log d \tag{2a}$$

where a and n are physical parameters, corresponding to elastic (strength) and plastic properties of the material [2, 3]. A critical value for n is observed ($n = 2$). At this value MHV is almost constant in depth. At $n < 2$ or $n > 2$, MHV is variable. It decreases ($n < 2$) or increases ($n > 2$), in the sample

*Corresponding author, e-mail: mstaneva@gmail.com

depth. This phenomenon has to be attributed to changes in the structure of the material [2, 4].

The dependence (2a) results in a straight line, where log*a* is the cut and *n* is the slope. Parameter *a* is determined using the antilogarithm of the cut-value: $a = 10^{\log a}$. Further on *a* is denoted as 'cut resultant parameter' (CRP).

CRP (*a*) corresponds to the elastic (strength) properties of the material and its physical meaning has not been elucidated fully yet [2–4].

The aim of this work was to calculate σ^{MHV} via CRP values applying empirical physical laws. Another form of Meyer's power law (Equation (2a)) is presented in Equation (2b):

$$P = a \cdot d^n \tag{2b}$$

The CRP value (*a*) can be calculated from Equation (1) and Equation (2b) (Equation (3)):

$$a = \frac{MHV}{1.8544} = \frac{P}{d^2} \tag{3}$$

Equation (3) is valid only when $n = 2$.

Our new approach to estimating of σ^{MHV} is based on the general requirement $n = 2$ and applies empirical physical laws.

The following nine steps were used to obtain the final result.

1.2.1. Evaluation of the experimental data viewing the fulfillment of the general requirement

Setting $n = 2$ as a general requirement is based on two considerations:

- The requirement $n = 2$ results from Equation (3), which was used for deriving the relation between σ^{MHV}, CRP (*a*) and *d* (see point (1.2.3) and (1.2.5) below).
- In the case $n \neq 2$, the unit of CRP (*a*) is unknown and has no physical meaning:
  - for $n < 2$ (i. e. $n = 1$), CRP (*a*) is measured in N/m;
  - for $n > 2$ (i. e. $n = 3$), CRP (*a*) is measured in N/m^3.

In case $n = 2$ the unit for CRP (*a*) is well defined and its physical meaning is a force applied to a unit area, [N/m^2].

1.2.2. Evaluation of the dimension of d, [μm]

As already mentioned Meyer's power law (Equation (2a)) is represented by a Meyer's line. For each straight line cut and slope can be calculated. The slope (*n*) has to be 2 (see point 1.2.1). The cut (log*a*) is calculated every time when log*d* = 0, i.e. $d = 1$. As in this case $d = 1$, if the dimension of *d* is μm, than the mean diagonal length of the impression is $d = 1$ μm. That is why a very small microscopic impression ($d = 1$ μm) has been used in our study. Further on the diagonal length of this very small microscopic impression is denoted as $d_{1\,\mu m}$.

1.2.3. Surface parameter MHV*

*MHV** was derived using Equation (3) (Equation (4)):

$$MHV^* = 1.8544 \cdot 10^{12} \cdot a;\ [\mathrm{Pa}] = \left[\frac{\mathrm{N}}{\mathrm{m}^2}\right] \tag{4}$$

*MHV** in Equation (4) is denoted as a surface parameter due to its unit [N/m^2] corresponding to surface stress.

1.2.4. Area of the very small microscopic impression with $d_{1\,\mu m}$ ($S_{1\,\mu m}$)

The equation given below was used for calculating $S_{1\,\mu m}$ (Equation (5)):

$$S_{1\mu m} = \frac{2 \cdot 0.38 \cdot d_{1\mu m}^2}{\sqrt{2}};\quad [\mathrm{m}^2] \tag{5}$$

Equation (5) was deduced after simple geometrical calculations. As the indenter is a diamond pyramid, the impression exhibits a pyramidal shape. The impression area is represented by the sum of the areas of the four pyramid walls. $d_{1\,\mu m}$ could be found on the top of the pyramid (impression).

1.2.5. Force required for the formation of a very small microscopic impression (F)

Multiplying the final results from point 1.2.3 (*MHV**) and point 1.2.4 ($S_{1\,\mu m}$) the Equation (6) is obtained:

$$MHV^{*}\cdot S_{1\mu m}=F;\ \left[\frac{\mathrm{N}}{\mathrm{m}^2}\right]=[\mathrm{m}^2] \tag{6}$$

1.2.6. Calculation of mean values (d_{real}^{mean}, h_{real}^{mean})

For each sample a mean d value for all loads applied is required to be calculated and is denoted as d_{real}^{mean}.

According to the geometry of the Vickers pyramid a relation between indentation depth (h) and d is derived (Equation (7)):

$$h=\frac{d}{7};\quad [\mathrm{m}] \tag{7}$$

Using d_{real}^{mean} and Equation (7) the mean h value for all loads applied (h_{real}^{mean}) for each sample is calculated.

1.2.7. Work required for formation of the very small microscopic impression (A)

'A' is calculated by Equation (8):

$$F\cdot h_{real}^{mean}=A;\quad [\mathrm{N}]\cdot[\mathrm{m}]=[\mathrm{J}] \tag{8}$$

1.2.8. Area of real impression (S_{real})

S_{real} is calculated from the experimentally obtained d_{real}^{mean}-values using Equation (9):

$$\frac{2\cdot 0.38\cdot (d_{real}^{mean})^2}{\sqrt{2}}=S_{real};\quad [\mathrm{m}^2] \tag{9}$$

1.2.9. Relation between σ^{MHV}, CRP (a) and d_{real}^{mean}

Having in mind the steps already mentioned, σ^{MHV} can be defined as the work, performed on a single unit area of real impression (S_{real}) as given by Equation (10):

$$\frac{A}{S_{real}}=\sigma^{MHV};\ \left[\frac{\mathrm{J}}{\mathrm{m}^2}\right] \tag{10}$$

Summarizing Equations (4)–(9) a simple expression for σ^{MHV} can be derived, as given by Equation (11):

$$\sigma^{MHV}=a\cdot K\cdot\frac{d_{1\mu m}^2}{d_{real}^{mean}};\ K=\frac{1.8544}{7};\ \left[\frac{\mathrm{J}}{\mathrm{m}^3}\right]\cdot\frac{[\mathrm{m}^2]}{[\mathrm{m}]}=\left[\frac{\mathrm{J}}{\mathrm{m}^2}\right] \tag{11}$$

Equation (11) represents a simple σ^{MHV} – dependence on d_{real}^{mean} and CRP (a).

1.3. Advantages and limitations of the new approach to the evaluation of σ^{MHV}

Another approach to calculation of surface free energy using microhardness data is described by Balta Calleja *et al*. [1, 5]. It is based on Equation (12):

$$\frac{2\sigma}{\Delta h}=l_c\cdot\left(\frac{H_c^0}{H_c}-1\right) \tag{12}$$

where σ is the surface free energy; Δh – the energy required for plastic deformation of the crystals; l_c – the average crystal thickness; H_c^0 – the microhardness of an infinitely thick crystal (maximum possible value of energy dissipated through plastic deformation); H_c – the intrinsic microhardness of the crystalline phase.

Comparing Equations (11) and (12) we should to point out that:

- Equation (11) is a very simple expression of σ^{MHV} dependence on the microhardness data. σ^{MHV} depends on two parameters (CRP (a) and d_{real}^{mean}) derived from a direct microhardness measurement. The surface free energy was calculated direct from the mean diagonal length of the impression (d) using simple mathematical transformations.
- Despite of microhardness measurement, Equation (12) requires data from other methods:
  - The average crystal thickness (l_c) has to be determined by SAXS.
  - Degree of crystallinity (determined by WAXS or DSC) is needed for calculating H_c.
- Expression (12) is applicable to semi-crystalline polymers like polyethylene samples of different structure [5, 6] and polymer blends [7]. We describe for the first time in this paper the application of Equation (11) to γ-irradiated PE-UHMW.

2. Experimental

2.1. Materials

PE-UHMW samples, prepared according to Bulgarian patent, Reg №30049 [8] (modified four component Ziegler-Natta catalytic system has been used), were supplied by Neftochim – Burgas. Molecular weight was determined by Vapor pressure osmometry ($M_n = 1.28 \cdot 10^5$) and by light scattering ($M_w = 1.2 \cdot 10^6$).

Test samples (4 mm thick) were prepared by pressing at 10–200 kN and subsequent sintering at 160–200°C.

2.2. Methods

2.2.1. γ-irradiation

The γ-irradiation was carried out by a γ-^{60}Co source at room temperature in air at a dose rate of 10 kGy/h. The samples were irradiated with 11 different doses: 1, 2, 5, 10, 20, 50, 100, 200, 500, 1000 and 1500 kGy. The doses were selected in such a way that their logarithmic values should increase linearly. In order to observe this dependence clearly and for convenience, the dose of the un-irradiated sample was selected to be 0.1 kGy. In this way the graphical presentation of the data can be easier understood and the dose dependences of the parameters calculated easier anticipated.

2.2.2. Vickers microhardness (MHV)

Microhardness was determined by the Vickers method. The experiment was carried out on a standard MHV tester mhp-160 for light microscope NU-2 (Germany). The loads applied were 0.0123, 0.0245, 0.049, 0.098, 0.196, 0.392, 0.785 N. Similarly to the dose range, the loads were selected in such a way that their logarithmic values should increase linearly. This choice is based on the fact that MHV is a linearly logarithmic dependent quantity ([1], p. 56), eq. (3.2). In all experiments loading time was 30 s.

3. Results and discussion

3.1. Meyer's lines

The Meyer's lines obtained are given on Figure 1. The dependence follows the Meyer's power law (Equation (2a)), which proves the reliability of the obtained MHV data. According to the values of the correlation coefficient (R) and standard deviation (SD), a good correlation between the load applied (P) and the indentation diagonal length (d) may be inferred from the experimental data (Table 1).

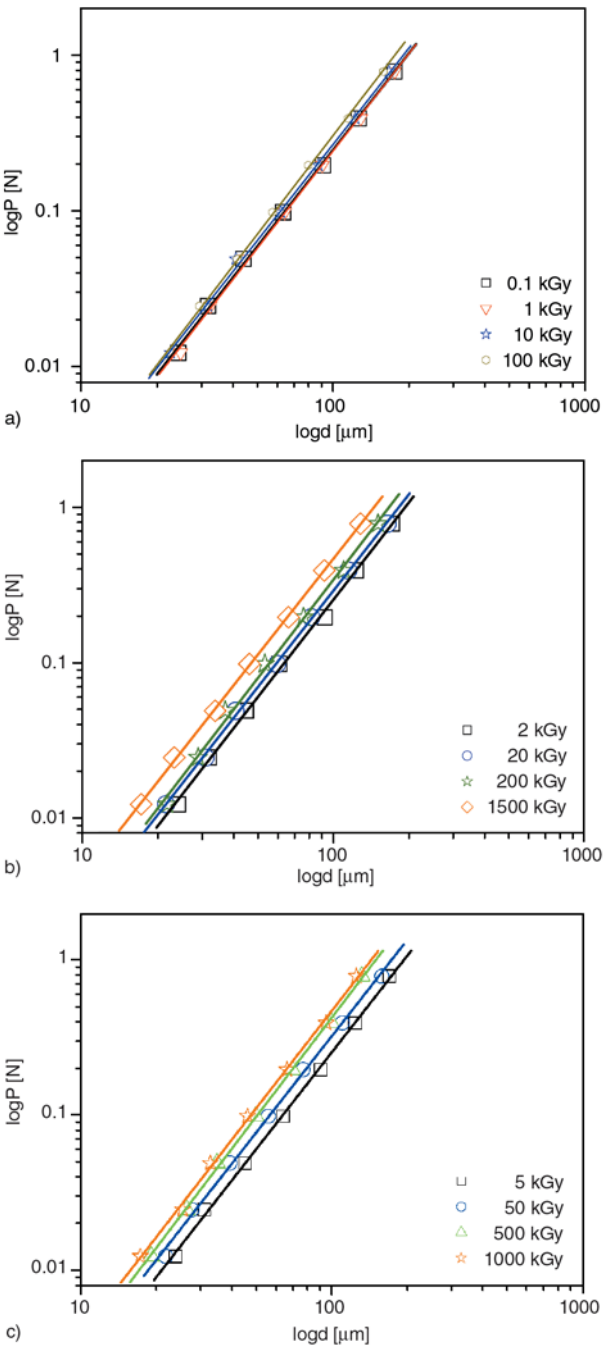

Figure 1. Meyer's lines for γ-irradiated PE-UHMW

3.2. Slope data (*n* values)

As already mentioned the general requirement is $n = 2$. The n-values (Table 2, Figure 2) of Meyer's lines for the PE-UHMW samples studied vary in the range 2.05–2.1. The mean slope-value (n_{mean}) is

2.07. 'nmean' is very close to the slope-value, required for applying Equation (11).

Table 1. Correlation coefficient (*R*) and standard deviation (SD) of the Meyer's lines

Dose [kGy]	R	SD
0.1	0.9993	0.03
1	0.9993	0.03
2	0.9992	0.03
5	0.9995	0.02
10	0.9992	0.03
20	0.9996	0.02
50	0.9989	0.03
100	0.9994	0.02
200	0.9983	0.04
500	0.9995	0.02
1000	0.9991	0.03
1500	0.9998	0.01

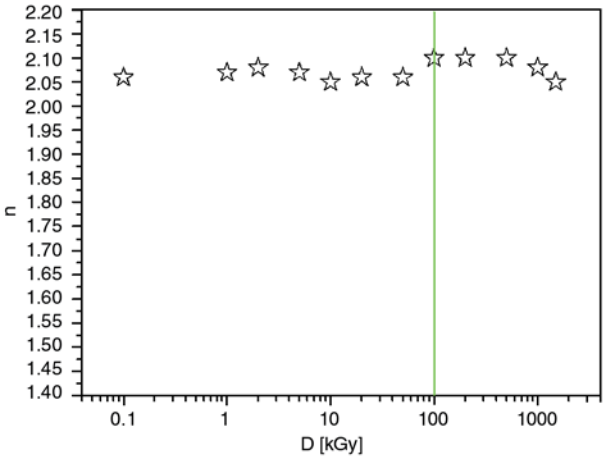

Figure 2. Dependence of the Meyer's lines slope value (*n*) on the dose (*D*); the symbol for dose is *D*, [kGy], in contrast to the mean diagonal length *d*, [μm]. Do not confuse the two parameters, please.

3.3. Surface free energy (σ^{MHV}) data and their reliability

All results are summarized in Table 2. Experimental values for surface free energy (Figure 4, σ^{MHV} = 0.057–0.173 J/m^2) show good agreement with literature data [5, 9, 10]. Balta Calleja *et al*. [5] reported σ = 0.079–0.091 J/m^2 for a series of PE samples of different molecular weights. Non-isothermal kinetics investigations [9] show similar results: $\sigma^{m,c}$ = 0.040–0.085 J/m^2. According to Wunderlich [10] σ = 0.06 J/m^2.

3.4. Radiation effects

For all samples investigated log*a* (Figure 3), CRP (Figure 4) and σ^{MHV} (Figure 5) exhibit well defined dose (*D*) dependence. It corresponds to the radiation effects theory for PE-UHMW [9] and ultra high molecular weight polyethylene oxide

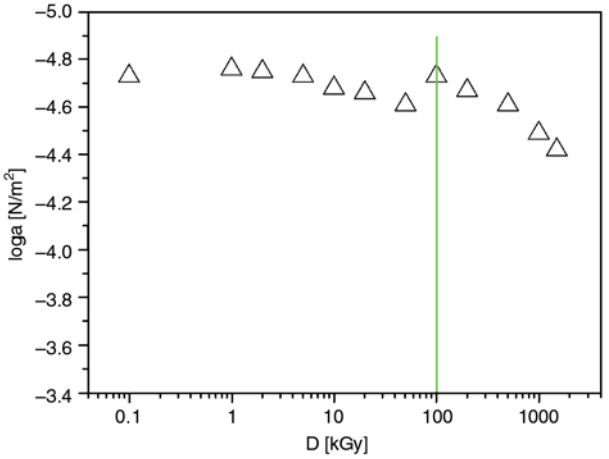

Figure 3. Dependence of the Meyer's lines cut values (log*a*) on the dose (*D*)

Table 2. Microhardness data for PE-UHMW samples γ-irradiated with different doses

D [kGy]	n	loga [N/m^2]	a·10^{-5} [N/m^2]	d_{real}^{mean}·10^{-5} [m]	σ^{MHV} [J/m^2]
0.1	2.06	–4.73	1.86	7.96	0.062
1	2.07	–4.76	1.74	8.02	0.057
2	2.08	–4.75	1.78	7.82	0.060
5	2.07	–4.73	1.86	7.83	0.063
10	2.05	–4.68	2.09	7.64	0.072
20	2.06	–4.66	2.19	7.33	0.079
50	2.06	–4.61	2.45	6.99	0.093
100	2.10	–4.73	1.86	7.21	0.068
200	2.10	–4.67	2.14	6.82	0.083
500	2.10	–4.61	2.45	6.15	0.110
1000	2.08	–4.49	3.24	5.82	0.150
1500	2.05	–4.42	3.80	5.81	0.170

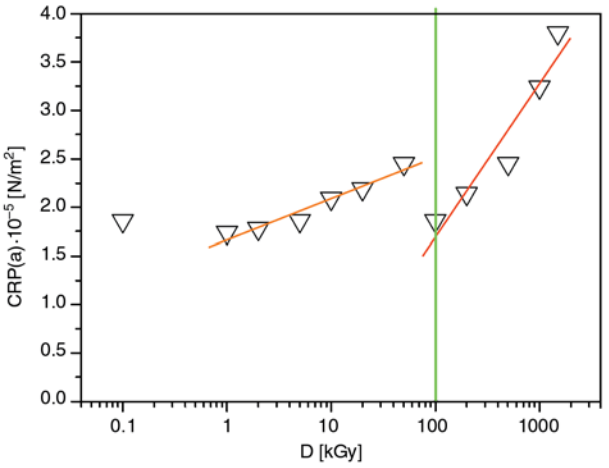

Figure 4. Dose dependence of CRP (*a*) values

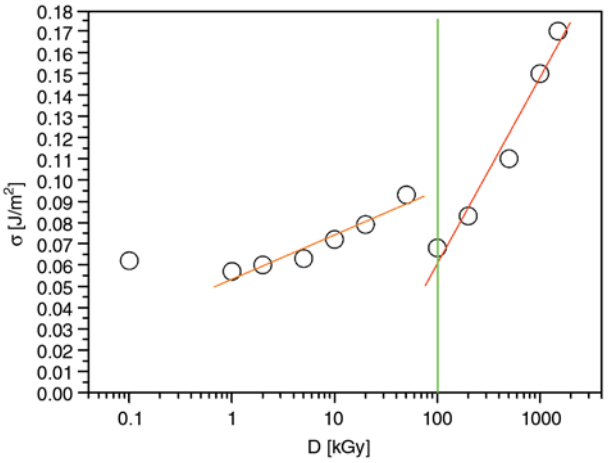

Figure 5. Dose dependence of σ^{MHV} values

(UHMWPEO) [11, 12]. Critical dose is observed at 100 kGy – the borderline between two radiation effects: radiation annealing and radiation melting.

The surface free energy (σ^{MHV}) shows a good linear dependence on the dose for each (of the) radiation effect. The first σ^{MHV} value (for the un-irradiated sample, $D = 0.1$ kGy, Figure 5) is used as a referent value. Two dose ranges were investigated and two radiation effects were observed:

– $D = 1$–50 kGy ($D < 100$ kGy): the effect of radiation annealing;
– $D = 100$–1500 kGy ($D \geq 100$ kGy): the effect of radiation melting.

The radiation effects result in changes in polymer structure. These changes proceed in the inter-crystalline (amorphous) lamellar spaces (Figure 6).

Radiation annealing and radiation melting are similar to the temperature annealing and temperature melting but the variable is the dose, not the temperature.

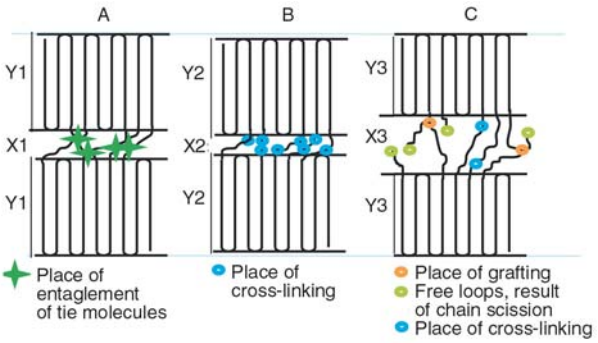

Figure 6. Lamellar structure of the polymer caused by γ-irradiation (B and C) compared to that of the un-irradiated sample (A): B – irradiated sample during radiation annealing; C – irradiated sample during radiation melting. Y_1, Y_2, Y_3 – lamellar crystal part: $Y_1 = Y_2 > Y_3$; X_1, X_2, X_3 – lamellar amorphous part: $X_1 > X_2 < X_3$

In the case of PE-UHMW the γ-irradiation causes simultaneous chain scission and recombination in the lamellar crystal parts. According to chain mechanism, chain scission and chain cross-linking proceed simultaneously in the amorphous lamellar part as well.

For these two processes, it is supposed that the macromolecules absorb energy, hence radiation defects/excitons occur.

In the range of radiation annealing ($D < 100$ kGy), excitons move along the macromolecular segments in the lamellar crystal part and are pushed out to the lamellar surface. This results in decrease of crystal defects and in increase of total crystallinity. The effect observed is denoted as radiation annealing, similar to temperature annealing. Low numbers of radiation defects/excitons are caused by irradiation doses in the range $D = 1$–100 kGy. They decrease the inter-lamellar stress due to chain-scission of the entangled and stressed tie molecules of PE-UHMW. Hence at very low doses (Figure 5, points at $D = 1$ kGy and $D = 2$ kGy) the lamellar surface free energy (σ^{MHV}) is lower compared to that of the un-irradiated sample ($D = 0.1$ kGy). At doses, close to the critical value ($D = 100$ kGy), the number of the excitons/radiation defects on the lamellar surface slightly increases. The defects cause mainly cross-linking. It slightly progresses to the surface and becomes more stressed, causing slow increase in the surface free energy (σ^{MHV}) with the increasing doses (Figure 5, orange line).

In the range of radiation melting ($D \geq 100$ kGy) much more excitons are formed. The number of

high energy excitons increases, so that the chain scission and cross-linking proceed only at the crystal-amorphous boundary. In this dose range the amorphous part thickness increases at the expense of the crystal one. The process is similar to the surface melting and therefore is denoted as radiation melting [11]. The increase of the dose (starting at D = 100 kGy) results in increase of the lamellar surface and the defects expand very quickly. Surface free energy (σ^{MHV}) increases rapidly (Figure 5, red line).

4. Conclusions

Using direct Vickers microhardness data (d) a new approach to calculating of surface free energy has been developed. After simple mathematical transformations, the parameters CRP (a) and d_{real}^{mean} were calculated and an equation for σ^{MHV} was deduced. This equation is applicable only at the general requirement (n = 2) – i.e Meyer's lines slope data (n) has to fulfill this requirement. The surface free energy (σ^{MHV}) data, obtained by applying our new approach to estimation of surface free energy based on Vickers microhardness data, show very good agreement with the literature [5, 9, 10]. It has been shown, that our new approach has rendered reliable results for the PE-UHMW samples studied. The σ^{MHV} values obtained are dose dependent and correspond to the radiation effects theory.

Acknowledgements

Maya Staneva would like to thank the Structural Funds and Educational Programs Directorate for the financial support within the frame of the Project 'Support for the development and realization of PhD-students, post-docs and young researchers in the field of polymer chemistry, physics and engineering', Grant № BG051PO001/07/3.3-02/51 51.

References

[1] Balta Calleja F. J., Fakirov S.: Microhardness of polymers. Cambridge University Press, Cambridge (2000).

[2] Zamfirova G., Dimitrova A.: Some methodological contributions to the Vickers microhardness technique. Polymer Testing, **19**, 533–542 (2000). DOI: 10.1016/S0142-9418(99)00023-9

[3] Zamfirova G., Lorenzo V., Benavente R., Pereña J. M.; On the relationship between modulus of elasticity and microhardness. Journal of Applied Polymer Science, **88**, 1794–1798 (2003). DOI: 10.1002/app.11788

[4] Zamfirova G., Pereña J. M., Benavente R., Perez E., Cerrada M. L., Nedkov E.: Mechanical properties of ultra high molecular weight polyethylene obtained with different cocatalyst systems. Polymer Journal, **34**, 125–131 (2002). DOI: 10.1295/polymj.34.125

[5] Baltá Calleja F. J., Santa Cruz C., Bayer R. K., Kilian H. G.: Microhardness and surface free energy in linear polyethylene: The role of entanglements. Colloid and Polymer Science, **268**, 440–446 (1990). DOI: 10.1007/BF01411002

[6] Flores A., Baltá Calleja F. J., Bassett D. C.: Microhardness studies of chain-extended PE: I. Correlations to microstructure. Journal of Polymer Science Part B: Polymer Physics, **37**, 3151–3158 (1999). DOI: 10.1002/(SICI)1099-0488(19991101)37:21<3151::AID-POLB24>3.0.CO;2-E

[7] Flores A., Aurrekoetxea J., Gensler R., Kausch H. H., Baltá Calleja F. J.: Microhardness-structure correlation of iPP/EPR blends: Influence of molecular weight and EPR particle content. Colloid and Polymer Science, **276**, 786–793 (1998). DOI: 10.1007/s003960050311

[8] Glavchev I., Radenkov Ph., Kabivanov V., Kircheva R., Yalamova T.: Method for preparation of PE-UHMW. Bulgarian patent. Reg. № 30049, Bulgaria (1975).

[9] Staneva M., Nedkov E.: Kinetic investigation of γ-irradiated PE-UHMW over non-isothermal processes according to renewed Nedkov-Atanasov approach. Radiation effects, in 'Reactor powder morphology' (eds.: Myasnikova L., Lemstra P. J.) Nova Science Publishers Inc., New York, in press (2009).

[10] Wunderlich B.: Macromolecular Physics, vol. 2. Mir, Moskva (1979).

[11] Nedkov E., Tsvetkova S.: Effect of gamma irradiation on the melting characteristics of ultra high molecular weight poly (ethylene oxide). Radiation Physics and Chemistry, **44**, 251–256 (1994). DOI: 10.1016/0969-806X(94)90002-7

[12] Nedkov E., Tsvetkova S.: Effect of gamma irradiation on the crystalline structure of ultra high molecular weight poly (ethylene oxide). Radiation Physics and Chemistry, **43**, 397–401 (1994). DOI: 10.1016/0969-806X(94)90034-5

eXPRESS Polymer Letters Vol.3, No.3 (2009) 145–151
Available online at www.expresspolymlett.com
DOI: 10.3144/expresspolymlett.2009.19

Interlaminar crack propagation in MWCNT/fiber reinforced hybrid composites

G. Romhány[*], *G. Szebényi*

Department of Polymer Engineering, Budapest University of Technology and Economics, Műegyetem rkp. 3., H-1111 Budapest, Hungary

Received 21 December 2008; accepted in revised form 30 January 2009

Abstract. In this work carbon fiber/epoxy composites and MWCNT (multiwalled carbon nanotube)/carbon fiber/epoxy hybrid composites with 0.1, 0.3, 0.5 and 1 weight% nanotube filling of the matrix have been prepared and compared in terms of interlaminar properties. For the dispersion of the carbon nanotubes in the epoxy resin three roll milling has been utilized. The mechanical characterization has been carried out using standard DCB (double cantilever beam) tests assisted by acoustic emission. The test results have been evaluated by the conventional method provided by the standard and a novel method implementing acoustic emission signal localization for crack propagation tracing. According to the tests carbon nanotube filling of the matrix of the composites has a beneficial effect on their interlaminar properties: the interlaminar fracture toughness values of the composites have increased by a maximum of 13 and 33% at a 0.3 weight% carbon nanotube content of the matrix according to the conventional and AE based evaluation method respectively.

Keywords: *polymer composites, nanocomposites, material testing, acoustic emission*

1. Introduction

In their first decades fiber reinforced composites mainly played the role of high performance materials for the high-tech industries as aerospace, military and racing industries. Nowadays the need for more fuel efficient vehicles in both aviation and vehicular traffic has induced the coming of a second golden age for composite materials. In most of their applications the composite parts are subjected to vibration which could lead to delamination and thereby the failure of the part, so it is crucial to improve the delamination resistance of polymer matrix composite materials.

Multiple reports showed the positive effect of carbon nanotube filling on the crack propagation resistance of polymer resins [1, 2]. Gojny *et al*. [3] have tested a standard epoxy resin mainly used for resin infusion filled with functionalized and unfunctionalized nanotubes. According to their tests a 43% increase in the fracture toughness of the resin could be observed at a 0,5% loading of amine functionalized DWCNTs (double walled carbon nanotubes). Ganguli *et al*. [4] examined the effect of MWCNT filling on the fracture toughness of a tetrafunctional epoxy resin through single edge notch three-point bending tests. They have measured a three-fold increase in the stress intensity factor at 1 weight% MWCNT loading. Delamination occurs in the resin filled interlayer between the reinforcement material layers in composite structures, so any toughening of the matrix material can improve delamination resistance. Although some promising theoretical results [5] and improvements in other interlaminar properties like interlaminar shear strength [6, 7] have been reported, few publications provide direct data on the interlaminar crack

[*]Corresponding author, e-mail: romhany@pt.bme.hu

propagation in CNT (carbon nanaotube) and fiber reinforced hybrid composites. Wichmann *et al*. [8] have reported a decrease in the Mode I interlaminar fracture toughness of DWCNT and glass fiber reinforced epoxy matrix composites, and pointed some difficulties during the tests caused by the obstructed tracking of the crack tip in the opaque resin using the conventional visual crack tracking during DCB testing. In our previous studies we have reported some indirect delamination resistance improvement in a nanotube/fiber reinforced system [9]. The aim of this research is to directly characterize the effect of carbon nanotube filling on the interlaminar mechanical properties of fiber reinforced composites through standard DCB tests.

2. Experimental

2.1. Materials

FM-20 epoxy laminating resin was used (P+M Polimerkémia Kft., Hungary) with T-16 curing agent (P+M Polimerkémia Kft., Hungary) as matrix. The recommended mixing weight ratio was 100:20, the resin had a curing treatment of 4 h at 60°C.

Baytubes® BT150 HP (Bayer, Germany) multiwalled carbon nanotubes (MWCNTs) were used as filler in one portion of the matrix (Figure 1). The nanotubes have been produced in a CVD based catalytic process resulting in an average outer diameter between 13–16 nm, length above 1 μm and carbon purity above 99% according to the manufacturer. The carbon nanotubes have been mixed to the epoxy component of the resin using a three roll mill, four pass-throughs have been carried out to achieve uniform dispersion and appropriate particle size (<10 μm).

Zoltek PX35FBUD0300 unidirectional carbon fabric (Zoltek Ltd., Hungary) has been used as fiber reinforcement in the composites. The fabric consisted of 50k rovings, and had a surface weight of 300 g/m^2.

2.2. Composite preparation

To characterize the effect of the nanotube filling of the matrix on the properties of carbon fiber reinforced composites one carbon fiber/epoxy laminate and four carbon nanotube/carbon fiber/epoxy laminates with 0.1, 0.3, 0.5, and 1 weight% nanotube filling have been produced under the same circumstances.

The laminates have been produced by hand lamination of 10 plies of carbon fabric impregnated with the resin, the fiber orientation of all laminae has been 0°. A 50 μm thick PET film has been used as a delamination initiator insert in the center plane (between the 5th and 6th lamina) of the laminates. Both sides of the film have been coated with mould release agent to minimize adhesion between the film and the matrix of the composite. To avoid trapped in air bubbles, the laminate has been rolled after every two plies.

To achieve uniform thickness and fiber content the laminate has been pressed for 12 hours under 30 kN at room temperature. The uniform thickness of all of the laminates has been achieved by using a 4 mm thick steel plate placed as a spreader next to the laminates in the press. The fiber contents were 49.2±1.1, 51.9±2.8, 51.7±3.2, 51.9±2.7, and

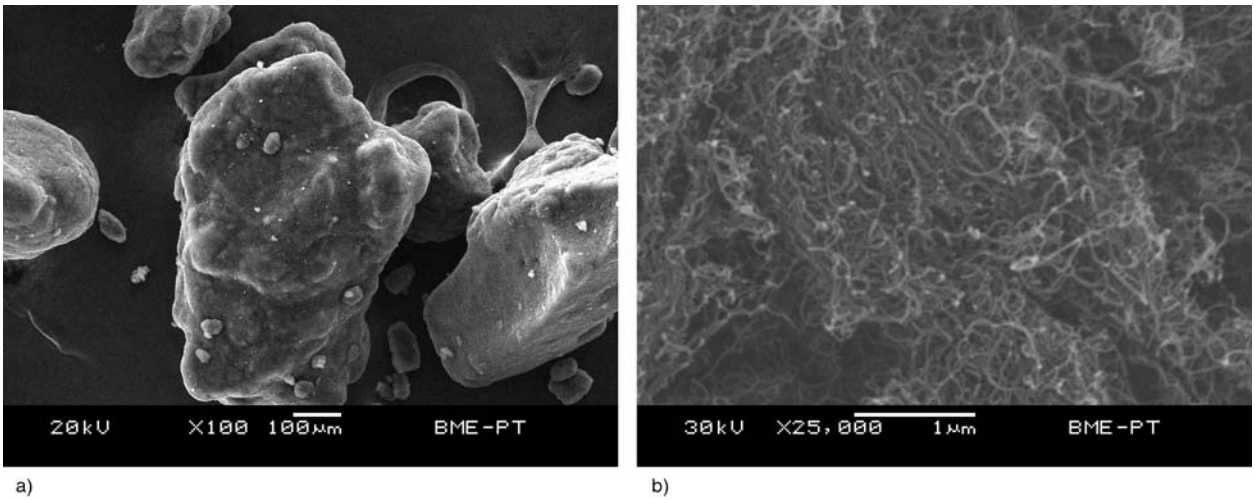

Figure 1. SEM micrographs of the MWCNT aggregates (a) and MWCNTs (b) used (raw materials)

53.4±1.9 volume% in the unfilled and 0.1, 0.3, 0.5 and 1 weight% MWCNT filled composite respectively.

2.3. Specimen preparation

8 specimens have been cut out of each laminate parallel to the fiber orientation according to ASTM D 5528 – 01 with a length of 210 mm, width of 25 mm, thickness of 4 mm, and an insert length of 65 mm. The edges of each specimen have been coated just ahead of the insert with a thin layer of water-based typewriter correction fluid to aid the visual detection of delamination propagation. A 100 mm length of the specimens has been marked with thin vertical lines every 2 mm from the insert to help the recording of the crack front position.
Steel load hinges have been mounted on the top and the bottom of each specimen using Sikadur 330 (Sika, Germany) adhesive, special care has been taken to the correct positioning of the load blocks. The specimen and test setup can be seen in Figure 2.

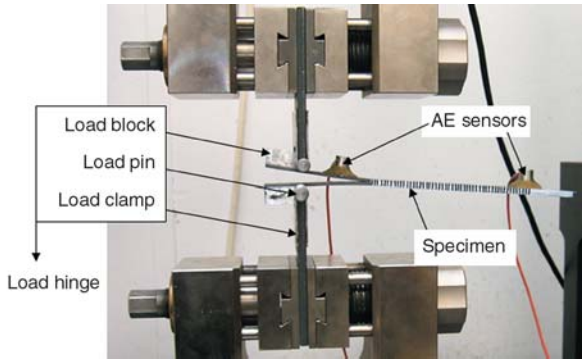

Figure 2. The DCB test setup

2.4. Characterization

Mode I interlaminar fracture toughness tests have been carried out on the test specimens according to ASTM D 5528 – 01 at a test speed of 5 mm/min using a Zwick 005 universal, computer controlled testing machine.
To pinpoint the position of the crack propagation more accurately than in case of visual detection the acoustic emission (AE) technique [10, 11] has been used (during visual detection, the crack propagation can only be observed after the curved crack front has reached the edge of the specimen, while AE signals can be detected immediately after the crack front starts to form). Sensophone AED-40 device with Physical Acoustics Corporation Micro30S sensors in the frequency range from 100 to 600 kHz have been used. Logarithmic amplifying has been applied. The threshold has been set to 30 dB to filter out ambient noises, and the reference voltage of the test device has been 3 mV. Two AE sensors have been fixed on the surface of the specimens at given positions, 120 mm-s from each other. After the measurement of the speed of AE signal propagation in the specimens (9000 m/s), the exact location of the AE event source, and so the crack front could be calculated from the detection time difference of the two sensors (Figure 3).

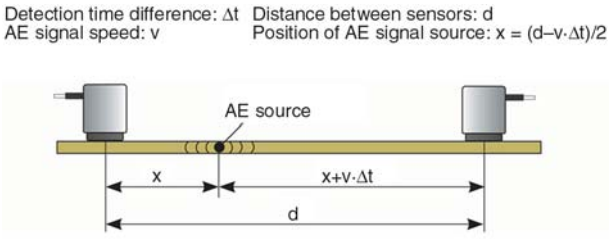

Figure 3. The principles of the localization of an AE source

3. Results and discussion

The main results of the DCB tests are the force – load point displacement and the crack front position – time curves. From these curves and the specimen geometry data the crack front position – interlaminar fracture toughness curves can be calculated and composed. The calculation of the strain energy release rate has been carried out using the modified beam theory. For the evaluation of the critical interlaminar fracture toughness, the 5% offset/maximum load method of the standard has been chosen. This method is the most effective to exclude the subjectivity of visual crack front tracing, but it has no direct connection with the failure processes in the specimens.
The critical interlaminar toughness values provided by this method can be observed in Figure 4. From the results it can be said that the G_{Ic} values increase with nanotube content to 0.3 weight% filling, after that a decrease can be observed. At 0.3 weight% nanotube content a 13% increase could be measured in the average toughness values compared to the unfilled matrix specimens.

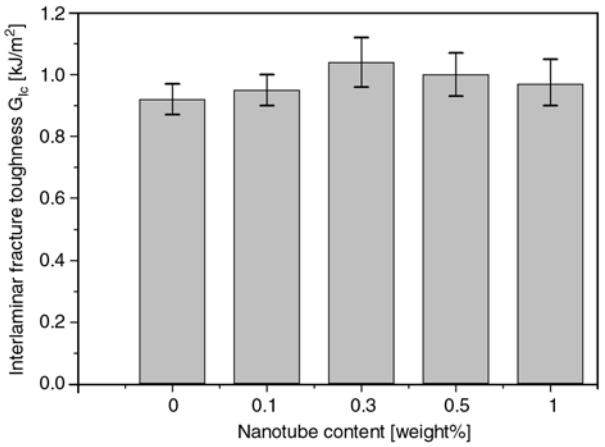

Figure 4. Interlaminar fracture toughness values of the composites and hybrid composites obtained by the 5% deviation method

The aim of using the AE technique was to introduce a crack propagation start criteria fully free of subjectivity, and in direct connection with the actual start of crack propagation.

The crack position values of AE events localized during the testing of a 0.1 weight% nanotube filled specimen can be seen in Figure 5.

From the graph it can be clearly seen that a dense region is present, containing a most of the detected AE signals, but the full spectrum is covered with traces. It can be explained firstly by the vast amount of AE events, leading to some localization problems (the device could not match all detection time differences with the right signal), secondly by the reflection of the AE signals in the specimens, which can make localization more difficult. In case of a high amplitude AE signal there is a high probability that it is a primary signal (signal detected for the first time, directly after emitted by the source), not a reflection. Therefore to filter improperly localized signals an amplitude threshold has been set.

After plotting the amplitudes of all localized events, this threshold has been set at 60 dB. Above this level higher amplitude signals could be still continually detected.

The events remaining after the filtering are plotted in Figure 6. It can be observed, that the region of the events representing the propagation of the crack front could be successfully narrowed down, also a clear trend can be observed according to the propagation of the crack front.

The results could be refined further by calculating the average of the crack positions in 15 s long intervals (1.25 mm of load point displacement). In Figure 7 the so calculated crack tip positions and the visually recorded positions can be compared. The crack tip positions are close to each other, so the AE localization could be verified by the visually recorded data.

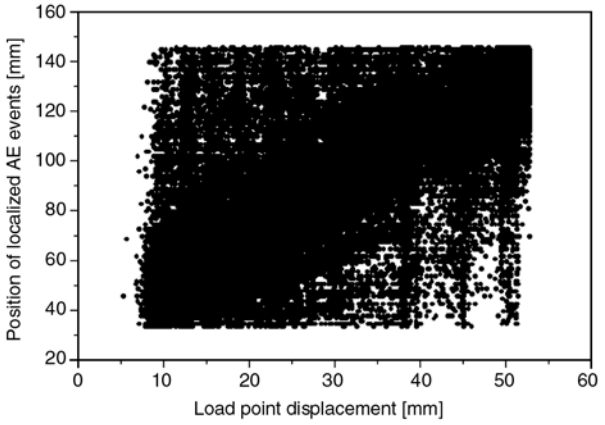

Figure 5. The localized AE events of a hybrid composite specimen with 0.1 weight% MWCNT content

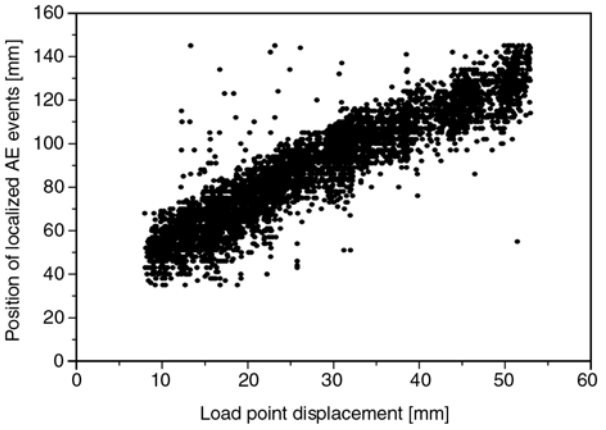

Figure 6. The localized AE events of a hybrid composite specimen with 0.1 weight% MWCNT content after filtering

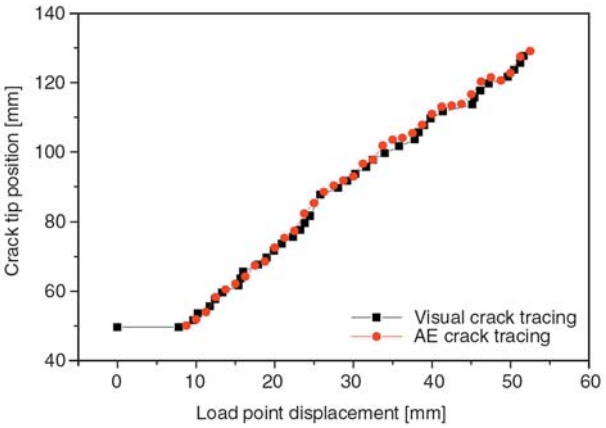

Figure 7. Comparison of crack tracing methods by a hybrid composite specimen with 0.1 weight% MWCNT

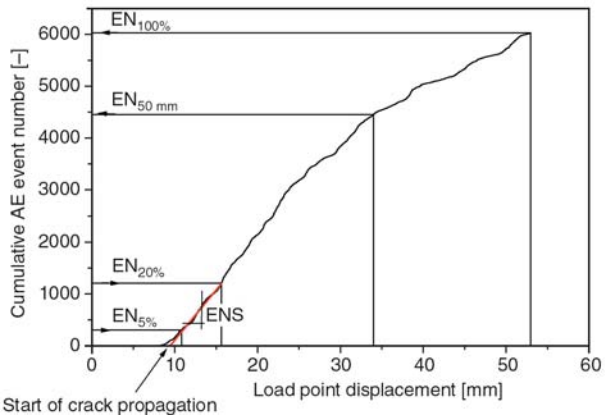

Figure 8. The definition of crack propagation start for the AE technique

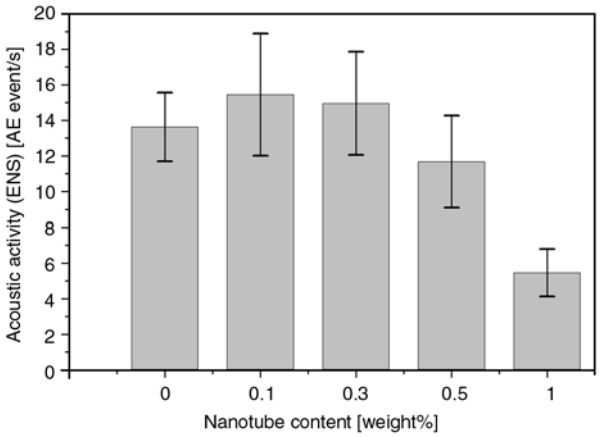

Figure 10. Acoustic activity as a function of nanotube content

In Figure 8 the cumulative AE event number versus load point displacement plot can be seen. It can be observed, that initially no signal is detected, then after a short transient section the acoustic activity and the slope of the curve increase significantly. It is evident that the crack propagation starts in the transient section. The crack propagation start has been defined as follows. The points corresponding to the 5 and 20% of total event number have been determined, and after that a line has been fitted between these two points using linear regression. The intersection of the regression line and the *x* axis has been defined as the opening displacement where the crack propagation started. The G_{Ic} values calculated using these data are plotted in Figure 9.

Compared to the method described in the standard the tendency of the G_{Ic} values in function of carbon nanotube content is the same, but in the values there is a significant difference. The difference can be explained by the more accurate crack tracing method, the crack propagation start could be pinpointed more precisely using the AE technique.

The slope of the line, fitted between the $EN_{5\%}$ and $EN_{20\%}$ points of the cumulative AE event number curve (ENS in Figure 8.), which corresponds to the acoustic activity during the stage of crack propagation (Figure 10), and also the event number localized till 50 mm crack propagation have been calculated (Figure 11).

The tendencies of both the acoustic activity and the event number versus carbon nanotube content are similar to the tendency of G_{Ic}. The event number values and the initial increase in acoustic activity suggest that the crack propagation can be composed of multiple smaller cracks. In case of brittle materials, like the epoxy used, unstable crack propagation can be observed, because the energy released during crack propagation is higher, than the energy needed for the creation of free surfaces. The crack front advances through unstably jumping

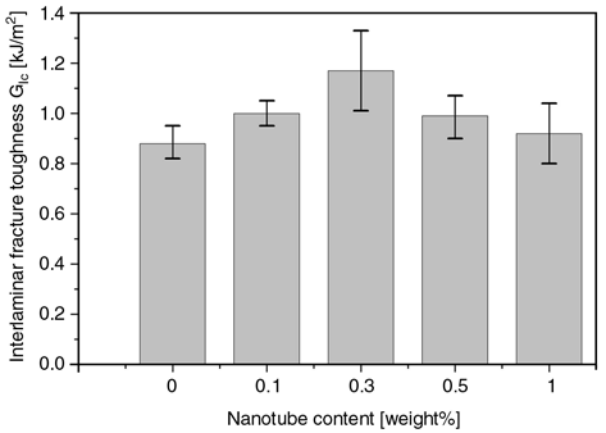

Figure 9. Interlaminar fracture toughness values of the composites and hybrid composites obtained by the AE method

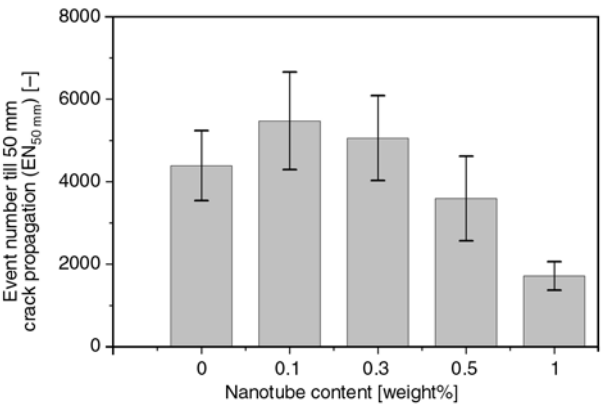

Figure 11. AE events localized till 50 mm crack propagation

and stopping microcracks, as with the advancement of the crack, the stress in the crack front is decreasing, and the crack propagation is caused by further opening displacement. The adhesion between the matrix and the nanotubes is fairly weak, so the nanotubes function as nanosized continuity flaws in the matrix in this case. When the microcracks jump forward, they propagate unstably, and when they reach a continuity flaw provided by a nanotube, they are pinned, so compared to the unfilled matrix composite, in hybrid composites, the formation of a higher amount, but smaller sized microcracks can be suggested. This causes the increase in acoustic event number and activity. According to the event numbers, above 0.5% nanotube filling another failure mechanism dominates. In that case nanotubes are present in such high amounts, that they tend to contact and form larger impurities, which have still the chance of pinning the microcracks, but they reduce the effective length of matrix material, which the crack has to propagate through which leads to less AE events, and lower resistance against crack propagation.

It is worthwhile to compare not only the G_{Ic} values, representing only one point of crack propagation, but also the full strain energy rate – crack length increase curves to get a deeper understanding of the full failure process, especially after G_{Ic}. The *R*-curves obtained from the averaging of the curves of each specimen of same nanotube contents can be observed in Figures 12 and 13. It can be clearly seen that the hybrid systems containing 0.1 and 0.3 weight% carbon nanotubes significantly outperform the unfilled matrix composite, while the 0.5 and 1 weight% nanotube filled ones remain around the level of the unfilled specimens.

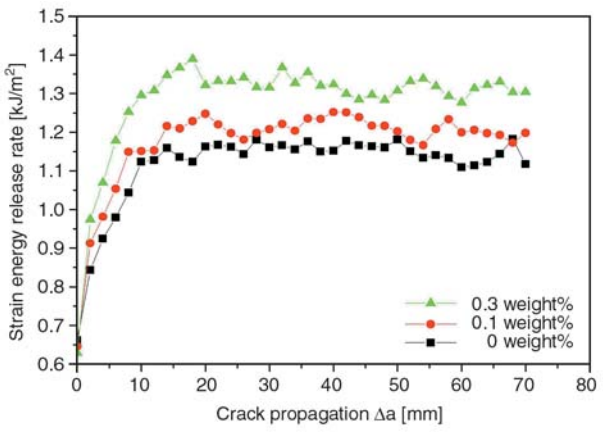

Figure 12. Average *R*-curves for composites containing 0, 0.1 and 0.3 weight% MWCNTs

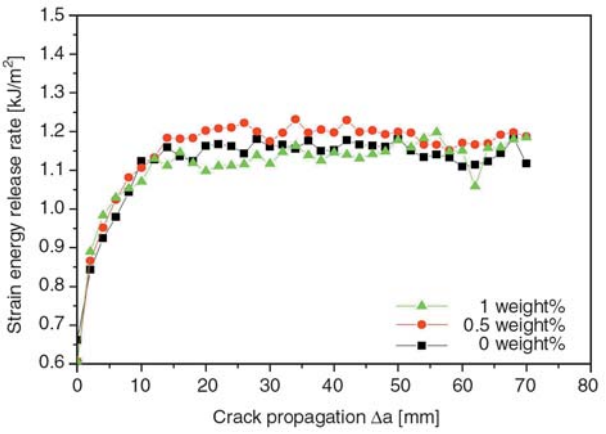

Figure 13. Average *R*-curves for composites containing 0, 0.5 and 1 weight% MWCNTs

4. Conclusions

In this work the effect of MWCNT reinforcement on the interlaminar mechanical properties of conventional carbon fiber/epoxy composites has been studied. The dispersion of the carbon nanotubes in the epoxy resin has been carried out using easily upscalable technique, three roll milling. Hybrid composite laminates containing 0, 0.1, 0.3, 0.5 and 1 weight% MWCNT filled matrices have been prepared by hand lamination followed by pressing using the nanotube filled resin and unidirectional carbon fabric. The mechanical characterization has been carried out using standard DCB tests assisted by acoustic emission. During the testing the negative effect of the completely opaque nanotube filled resin on the visual crack propagation tracing has been disabled using a novel evaluation technique utilizing AE crack tracing. According to the tests carbon nanotube filling of the matrix of the composites has a beneficial effect on their interlaminar properties: the interlaminar fracture toughness values of the composites have increased by a maximum of 13 and 33% at a 0.3 weight% carbon nanotube content of the matrix according to the conventional and AE based evaluation method respectively. According to our results it can be declared, that carbon nanotube filling of the matrix of conventional fiber reinforced composites can increase their performance, reliability when subjected to the danger of delamination.

Acknowledgements

The authors would like to sincerely thank Bayer Hungaria Ltd. and Bayer MaterialScience AG. for the donation of the Baytubes®. This work was supported by the Hungarian Scientific Research Fund (OTKA F67897 and NI62729) and János Bolyai Research Scholarship of the Hungarian Academy of Sciences.

References

[1] Du J-H., Bai J., Cheng H-M.: The present status and key problems of carbon nanotube based polymer composites. Express Polymer Letters, **1**, 253–273 (2007). DOI: 10.3144/expresspolymlett.2007.39

[2] Zhou Y. X., Wu P. X., Cheng Z-Y., Ingram J., Jeelani S.: Improvement in electrical, thermal and mechanical properties of epoxy by filling carbon nanotube. Express Polymer Letters, **2**, 40–48 (2008). DOI: 10.3144/expresspolymlett.2008.6

[3] Gojny F. H., Wichmann M. H. G., Fiedler B., Schulte K.: Influence of different carbon nanotubes on the mechanical properties of epoxy matrix composites – A comparative study. Composites Science and Technology, **65**, 2300–2313 (2005). DOI: 10.1016/j.compscitech.2005.04.021

[4] Ganguli S., Bhuyan M., Allie L., Aglan H.: Effect of multi-walled carbon nanotube reinforcement on the fracture behavior of a tetrafunctional epoxy. Journal of Materials Science, **40**, 3593–3595 (2005). DOI: 10.1007/s10853-005-2891-x

[5] Tong L., Sun X., Tan P.: Effect of long multi-walled carbon nanotubes on delamination toughness of laminated composites. Journal of Composite Materials, **42**, 5–23 (2008). DOI: 10.1177/0021998307086186

[6] Kim M-G., Hong J-S., Kang S-G., Kim C-G.: Enhancement of the crack growth resistance of a carbon/epoxy composite by adding multi-walled carbon nanotubes at a cryogenic temperature. Composites Part A: Applied Science and Manufacturing, **39**, 647–654 (2008). DOI: 10.1016/j.compositesa.2007.07.017

[7] Gojny F. H., Wichmann M. H. G., Fiedler B., Bauhofer W., Schulte K.: Influence of nano-modification on the mechanical and electrical properties of conventional fibre-reinforced composites. Composites Part A: Applied Science and Manufacturing, **36**, 1525–1535 (2005). DOI: 10.1016/j.compositesa.2005.02.007

[8] Wichmann M. H. G., Sumfleth J., Gojny F. H., Quaresimin M., Fiedler B., Schulte K.: Glass-fibre-reinforced composites with enhanced mechanical and electrical properties- Benefits and limitations of a nanoparticle modified matrix. Engineering Fracture Mechanics, **73**, 2346–2359 (2006). DOI: 10.1016/j.engfracmech.2006.05.015

[9] Romhány G., Szebényi G.: Preparation of MWCNT/carbon fabric reinforced hybrid nanocomposite and examination of its mechanical properties. Materials Science Forum, **589**, 269–274 (2008).

[10] Czigány T., Marosfalvi J., Karger-Kocsis J.: An acoustic emission study of the temperature-dependent fracture behavior of polypropylene composites reinforced by continuous and discontinuous fiber mats. Composites Science and Technology, **60**, 1203–1212 (2000). DOI: 10.1016/S0266-3538(00)00059-2

[11] Czigány T., Karger-Kocsis J.: Determination of the damage zone size in textile fabric reinforced polypropylene composites by locating the acoustic emission. Polymers and Polymer Composites, **1**, 329–339 (1993).

eXPRESS Polymer Letters Vol.3, No.3 (2009) 152–158
Available online at www.expresspolymlett.com
DOI: 10.3144/expresspolymlett.2009.20

Structure aggregation of carbon black in ethylene-propylene diene polymer

S. N. Lawandy, S. F. Halim, N. A. Darwish*

Laboratory of Metrology and Technology of Polymer, National Institute of Standards (NIS),Tersa St., 12211 Giza, Egypt

Received 30 November 2008; accepted in revised form 27 January 2009

Abstract. The modulus of filled and unfilled Ethylene-propylene diene rubber (EPDM) vulcanizates was used to predict the shape-factor of carbon black aggregation in the polymer. Four types of carbon black that vary in particle size and structure were used in this study. Quadratic curves relating the carbon black volume concentration and the modulus ratio of filled and unfilled rubber vulcanizates were used to adopt the shape factor of certain carbon black type. The shape factor of MT, HAF, SRF and Lampblack were 3, 3.75, 4 and 4.25 respectively. X-ray diffraction technique (XRD) was also used to evaluate the relative size of crystallite on the filler surface to that of the rubber and correlating it to the shape factor of carbon black aggregation in the polymer. Effect of the pH values and structure of carbon blacks used on the shape factor of filler aggregates were also studied. It was found that the shape factor is independent on the particle size while it is dependent on the pH value and structure of carbon black. Also the crystallites size of the filler is proportional to the shape factor.

Keywords: *rubber, EPDM, carbon black, shape factor, vulcanizates*

1. Introduction

The polymer-carbon black filler reinforcement depends widely on the polymer type, carbon black type and structure. Another factor affecting this reinforcement is the filler-filler interaction which leads to the formation of three dimensional aggregation structures within the bulk of the rubber matrix. These aggregations take various shapes which may be spherical or ellipsoidal with different major and minor axes [1]. Several aggregates connect through Van der Waals forces to give weak, giant assembled called agglomerates [2–4]. Several authors investigated and discussed the structure of these aggregates by using several techniques such as relating the modulus of unfilled rubber to that of filled rubber [5, 6], scanning electron microscope [7, 8] and Transmission electron microscopy TEM [9].

In this paper we will discuss the shape factor of the filler aggregates in the rubber matrix starting by the enhancement of elastomer modulus based on the rubber-filler interaction. These modulus studies started by Rehner [10] who adopted the well-known Einstein equation (Equation (1)):

$$\eta=\eta_0(1+2.5C) \tag{1}$$

where η and η_0 are the viscosities of liquid having suspended particles and that of the liquid respectively and C is the volume fraction of the particles suspended in the liquid. Smallwood, who suggested a rubber-filler interaction [11], replaced the viscosity terms in Equation (1) by Youngs modulus terms to be Equation (2):

$$E_f=E_0(1+2.5C) \tag{2}$$

*Corresponding author, e-mail: sawsanhanna@hotmail.com

where E_f and E_0 in Equation (2) are the moduli of filled and unfilled vulcaniztes respectively and C is the volume fraction of the filler in the mix. Equation (2) can be hold only for low concentration of filler. Guth [12] gives a modified equation (Equation (3)):

$$E_f = E_0(1+2.5C+14.1C^2) \tag{3}$$

where the last term of Equation (3) is due to the interaction between carbon particulates and the polymer. However, these last two equations have been shown to hold for large particle size of carbon black where the rubber-filler interaction is comparatively small. For non spherical particles Guth [13] introduce shape factor f_s, which is the ratio of asymmetric particles length to their diameter, and proposed the Equation (4):

$$E_f = E_0(1+0.67f_sC+1.62f_s^2C^2) \tag{4}$$

For higher volume fraction of filler, several equations have been given [14, 15]. Recently Oberdisse *et al*. [16, 17] studied the reinforcement effect of soft polymer which is nanolatex polymer polymethyl methacrylate and polybutylacrylate by nanosilica. They study the structure of the silica in the composite matrix by small angle neutron scatterings (SANS) and stress-strain measurements. In order to analyses their stress-strain data they use other expression for modulus. This expression was given by Oberdisse as shown in Equation (5):

$$\frac{E}{E_{latex}} = \frac{\exp 2.5C_{agg}}{1-\dfrac{C_{agg}}{{}^{\max}C_{agg}}} \tag{5}$$

where (Equation (6)):

$$C_{agg} = \frac{C_{si}}{\upsilon} \tag{6}$$

where C_{si} is in Equation (6) the volume fraction of silica, ${}^{\max}C_{agg}$ is the volume fraction aggregation at higher volume concentration 60% and υ is the aggregate compactly factor. The experimental determination of υ is not an easy task and that there are a lot of arguments about ${}^{\max}C_{agg}$ because of collisions between aggregates and the dispersion of aggregation. Similar trials for the filler aggregation and structure were indicated by Medalia [18-19].

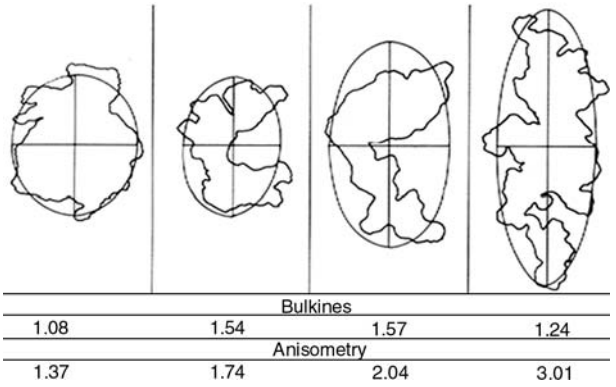

Figure 1. Aggregation structure of carbon black [18, 19]

His technique depends on the analysis of electron micrographs. The filler aggregate shape was subjected to computer integrations. The maximum and minimum moments of inertia were determined. These were the two axes of an ellipse. The ratio between these axes is the anisometry Q. The ratio between silhouette area over the ellipse area is the bulkiness, B, from which the structure factor $T = QB–1$. Figure 1 shows an illustration for the different anisometry (Q) of filler aggregates.

The trouble with calculating the structure factor is that many aggregates or particles have to be reviewed before average value for anisometry and bulkiness can be reached and hence the measurement is very consuming. Later, transmission electron microscopy combined with computerized tomography was used by Kohjiya *et al*. [9] and others to display the skeleton characteristics of nanofiller carbon black network in natural rubber. Their study was based on the fact that filler-filler interaction is higher than filler to rubber and that further association of filler aggregates, i.e. agglomeration leads to another form of filler network [20]. Figure 2 shows the aggregation and agglomeration of carbon black in the rubber.

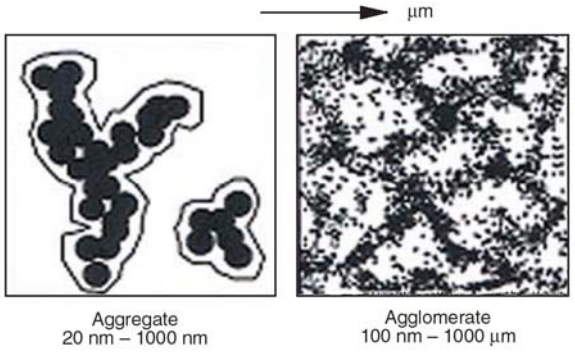

Figure 2. The aggregation and agglomeration of carbon black in rubber [9]

The techniques mentioned before to display the filler aggregation, agglomeration and the method used to quantify the filler network showed controversial results.

We used the simple stress-strain data to reach certain reliable data explaining the shape-factor of carbon black in a certain polymer matrix. We verify our results by X-ray diffraction technique (XRD).

2. Experimental

2.1. Materials

The polymer used in this study is Ethylene-propylene diene rubber (EPDM), Buna EPT 9650, Bayer. The Ethylene content is 53±4, ENB content 6.5±1.1 and the viscosity ML (1+8) at 150°C is 60±6. Dicumyl peroxide (DCP), UN Korean of density 1.56 was used as cross-linking agent. High abrasion carbon black HAF-LS (N-326), Thermal black MT (N-990), Semi-reinforcing SRF (N-774) and Lampblack were used as fillers with different concentrations in the rubber mixes. The main structural parameters of carbon blacks are listed in Table 1. The mix formulations are given in Table 2.

2.2. Mixing and sample preparation

Mixing was carried out on two-roll laboratory open mixing mill (152.4×330.2 mm) at a friction ratio 1:1.4. The mixing was carried out according to ASTM D3182.89. The optimum cure time of each compounded rubber mix was detected using a Monsanto Rheometer (Alpha Technologies MDR 2000) working at 162°C. An average cure time for all mixes was selected and used for all samples to ensure fair results. Samples for testing were compression molded in a laboratory hydraulic press (Mackey Bowley, C1136199) at 162°C. The rheometric properties of each mix are given in Table 3.

2.3. Stress-strain measurements

Dumbbell shape samples prepared according to ASTM D 412-98a were used for relaxed stress-strain measurements. Zwick tensile testing machine Z010/TH2A was run at speed 10 mm/min and the stress-strain curves of various mixes was recorded up to 16% strain.

Table 1. Formulation of the EPDM mixes containing various types of carbon blacks

Formulation of the EPDM mixes containing HAF and SRF carbon blacks											
Mixes no. Ingredients [phr]	**B**	**H_1**	**H_2**	**H_3**	**H_4**	**H_5**	**S_1**	**S_2**	**S_3**	**S_4**	**S_5**
EPDM	0	100	100	100	100	100	100	100	100	100	100
Stearic Acid	2	2	2	2	2	2	2	2	2	2	2
Zinc oxide	5	5	5	5	5	5	5	5	5	5	5
Dicumyl peroxide	3	3	3	3	3	3	3	3	3	3	3
HAF	–	20	30	40	50	60	–	–	–	–	–
SRF	–	–	–	–	–	–	20	30	40	50	60
Formulation of the EPDM mixes containing MT and Lampblack carbon blacks											
Mixes no. Ingredients [phr]	**B**	**M_1**	**M_2**	**M_3**	**M_4**	**M_5**	**L_1**	**L_2**	**L_3**	**L_4**	**L_5**
EPDM	0	100	100	100	100	100	100	100	100	100	100
Stearic Acid	2	2	2	2	2	2	2	2	2	2	2
Zinc oxide	5	5	5	5	5	5	5	5	5	5	5
Dicumyl peroxide	3	3	3	3	3	3	3	3	3	3	3
MT	–	20	30	40	50	60	–	–	–	–	–
Lampblack	–	–	–	–	–	–	20	30	40	50	60

Table 2. The main specifications of the carbon blacks used [1]

Carbon black	**Average (elementary) particle size[1] [nm]**	**pH value**	**Structure[2] [cm³ DBP/100 g filler]**
HAF (N-326)	26–30	9.2	67
SRF (N-774)	61–100	9.9	70
MT (N-990)	201–500	7.4	33

[1]According to the ASTM D1765-86

[2]According to the ASTM D2414

Table 3. Rheological and mechanical properties of filled and unfilled EPDM rubber vulcanizates

Rheological and mechanical properties of EPDM rubber vulcanizates containing HAF and SRF carbon blacks											
Mixes **Curing characteristics**	**B**	**H_1**	**H_2**	**H_3**	**H_4**	**H_5**	**S_1**	**S_2**	**S_3**	**S_4**	**S_5**
Minimum Torque [N·mm]	0.01	0.02	0.02	0.2	0.03	0.03	0.02	0.02	0.02	0.02	0.03
Maximum Torque [N·mm]	0.15	0.19	0.21	0.25	0.29	0.32	0.20	0.22	0.25	0.30	0.31
Cure time, t_{C90} [min]	13.0	13.3	13.5	13.50	13.4	11.9	11.3	11.20	11.10	11.30	11.3
Scorch time t_{S2} [min]	0.90	0.94	0.89	0.82	0.77	0.70	0.84	0.81	0.76	0.68	0.68
Tensile Strength [MPa]	1.41	3.97	6.36	7.55	9.42	14.4	5.22	9.06	14.1	16.8	19.9
Elongation at break [%]	140	241	427	346	326	364	358	429	451	403	392
Rheological and mechanical properties of EPDM rubber vulcanizates containing MT and Lampblack carbon blacks											
Mixes **Curing characteristics**	**B**	**M_1**	**M_2**	**M_3**	**M_4**	**M_5**	**L_1**	**L_2**	**L_3**	**L_4**	**L_5**
Minimum Torque [N·mm]	0.01	0.02	0.02	0.02	0.02	0.02	0.02	0.02	0.02	0.03	0.03
Maximum Torque [N·mm]	0.15	0.20	0.30	0.24	0.26	0.28	0.22	0.26	0.27	0.33	0.35
Cure time, t_{C90} [min]	13.0	11.4	11.3	11.2	11.2	11.3	11.4	11.3	11.3	11.1	11.2
Scorch time t_{S2} [min]	0.90	0.81	0.76	0.70	0.68	0.66	0.73	0.67	0.67	0.58	0.55
Tensile Strength [MPa]	1.41	3.52	3.45	5.9	7.32	9.1	4.5	8.0	10.7	15.9	15.5
Elongation at break [%]	140	313	261	353	338	378	314	347	352	389	336

2.4. X-ray diffraction (XRD)

Philips Analytical X-ray diffraction, type PW1840 of Cu radiation was used. It operates at 40 kV and 30 mA with a wavelength (λ) 1.54056 Å. The diffractograms were recorded continuously in the range 2θ = 4–70°.

3. Results and discussion:

3.1. Determination of shape factor from stress-strain measurements

The modulus at 16% strain values of the unfilled EPDM rubber vulcanizates (E_0) and those of filled (E_f), at the various carbon black concentrations 20, 30, 40, 50 and 60 phr was measured and the ratio Ef/E_0 were calculated. Also the carbon black volume fraction (C) was calculated for each concentration (carbon black volume/rubber filled volume). Quadratic curves of carbon black shape-factor were plotted using Equation (4) by implementing several values of f_s (2.5, 3, 3.5, 4 and 4.5). By plotting curves using the values of the ratio E_f/E_0 versus C for each carbon black type, the shape-factor of each carbon black can be adduced by selecting the quadratic shape-factor curve to which the points are fitted. Figure 3 shows these quadratic curves and that of EPDM filled rubber with MT, HAF, SRF and LB. It was found that the shape factor of Lampblack, SRF, HAF and MT are 4.25, 4, and 3.75, 3 respectively. These recorded results show that the shape factor is independent of the particle size of the carbon black that is given in Table 1.

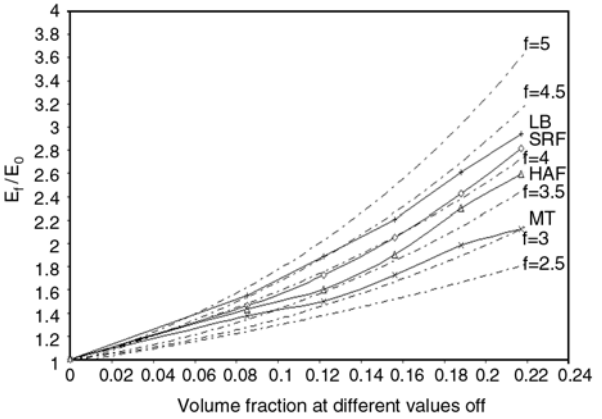

Figure 3. Shape factor of different carbon blacks aggregates

3.2. Shape factor and pH value and structure of carbon black

Table 2 includes two important parameters which are the structure and pH value of these blacks. It is to be noted here that, the Lampblack pH value is not mentioned in this table because of the wide range and classifications of these blacks. However, plotting the relation between the shape factor and pH values of the used carbon black, the pH value of the used LB black was estimated to be nearly 10.3. This can be shown in Figure 4. It is clear from Figure 4 that the shape factor increases as the pH val-

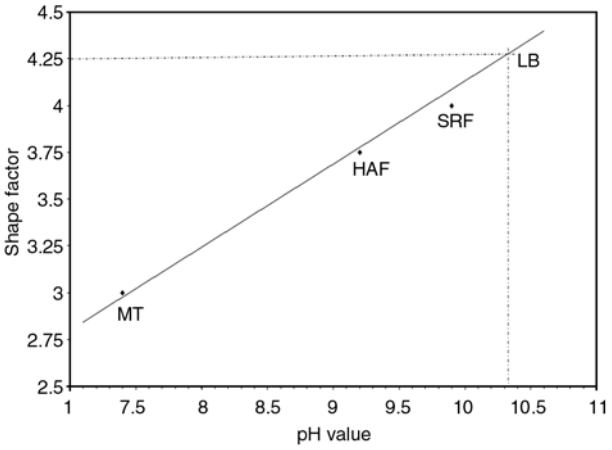

Figure 4. The relation between pH values of carbon blacks and the shape factor of carbon black aggregates

ues of carbon black increases. This is referred to the presence of chemisorbed oxygen complexes on carbon black surfaces. The major functional oxygenated groups are carboxylic, quinoic phenolic or lactonic groups. Oxygenated functional groups are acidic and control the pH value of carbon black [21, 22]. The pH values of carbon black affect their dispersion in the polymer matrix [23].

Plotting a relation between carbon black structure and the aggregates shape factor of carbon blacks reveals an interesting relation as shown in Figure 5. This relation was expected as the carbon black structure is a sort of volume concentration of carbon in one cm^3 of filler. Carbon black structure is determined by Dibutyl Phthalate (DBP) absorption (ASTM D2414) which measures the amount of oil that can be absorbed by the filler particles. A high value of DBP absorption indicates a high-structure black [22, 24, 25]. A high structure black has a strong attractive force between its aggregate and tends to produce larger aggregates in contact separated by small distances [26–28]. It was reported [26] that the aggregate anisometry is associated with the DBP absorption capacity. Figure 5 shows that the higher structure of carbon black are the higher the shape factor of carbon black aggregates.

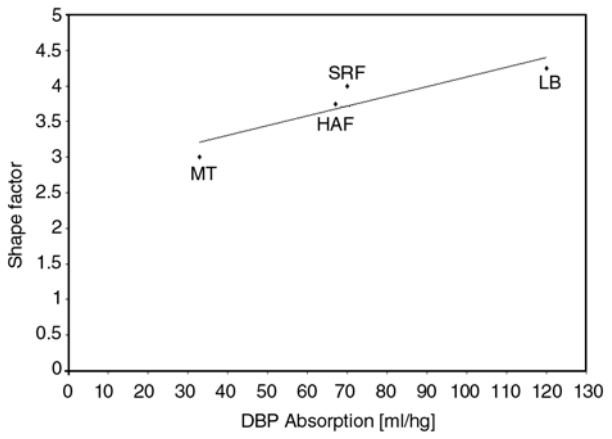

Figure 5. The relation between DBP values(Structure) of carbon blacks and the shape factor of carbon black aggregates

3.3. XRD

In order to investigate the degree of aggregation of carbon black in the EPDM rubber vulcanizates; attempts were made to quantify the crystalline regions present in EPDM filled with various types of carbon black using X-ray diffraction technique. As shown from Figure 6 all samples showed the same broad pattern at $2\theta = 14–20°$ which represent the amorphous EPDM polymer; this is followed by a distinct crystalline region representing the carbon black aggregation at $2\theta = 20–28°$. This is expected since carbon black aggregates tend to concentrate in amorphous regions [29]. The width of this carbon black crystalline pattern depends widely on the type of carbon black in the mix. The half-band width of the crystalline pattern that accompanied the amorphous pattern of the rubber was measured accurately (relative to fixed width of the amorphous rubber pattern). These values were plotted versus carbon black shape factor, found before in section 3.1. These can be shown in Figure 7. It is clear that the aggregates shape factor increases with the increase of the half-band width of X-ray patterns which means that the crystallite size decreases (inverse relation) [30, 31]. In other words as the crystallites size decrease the shape factor increases. These results can be correlated with that obtained by Biscoe and Warren [32] who identified the aggregate structure as intermediate between crystalline and amorphous materials. Energy of interaction between polymer and carbon black depends on nature and amount of crystallites. The most energetic sites, which very effectively adsorb polymers, are usually identified as crystallite edges. Small crystallites are not energetically favorable structure [33]. So as the crystallite size decreases the rubber filler interaction decreases this happens in favor to the filler-filler interaction rather than rubber-filler interaction. This is supposed to lead to the formation of aggregates with higher shape factor.

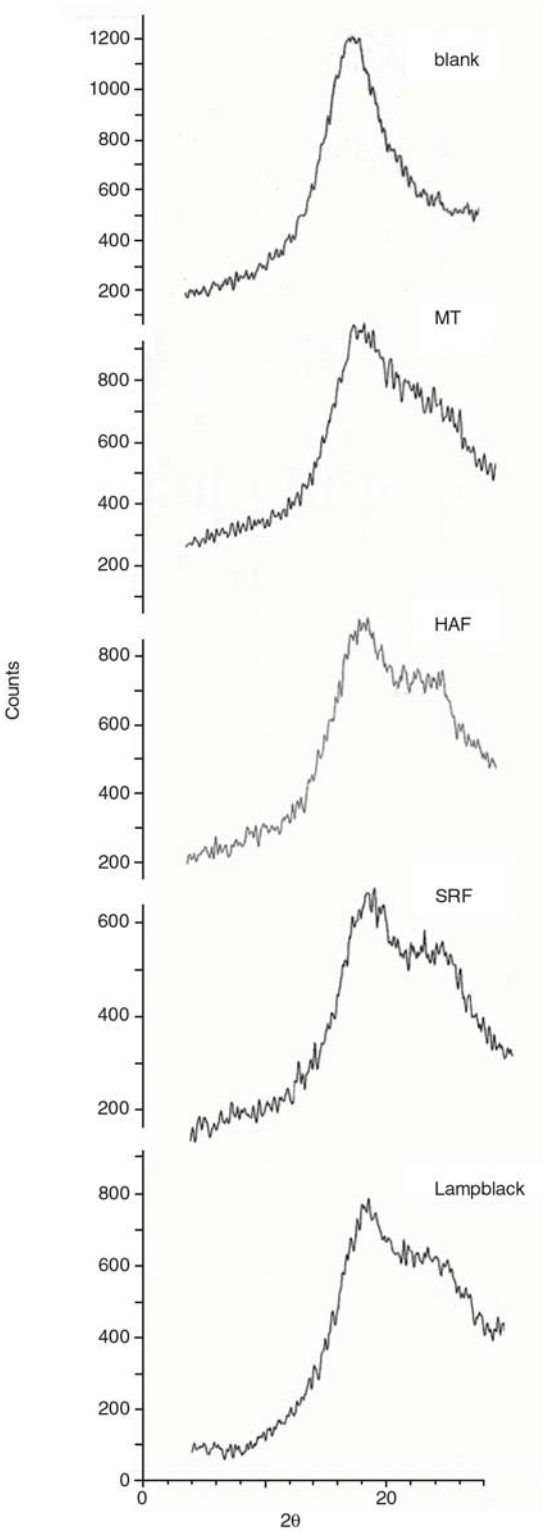

Figure 6. X-ray diffraction patterns for unfilled (blank) and filled EPDM vulcanizates with different fillers

4. Conclusions

The modulus at low strain of filled and unfilled rubber is a reliable method to detect the shape factor of different carbon black aggregates in rubber. Also the X-ray diffraction is good tool to estimate the relative distribution of carbon black which can express the degree of aggregation in the rubber mixes. The shape factor of carbon black aggregates in EPDM is independent on the carbon black particle size while it is directly proportional to the pH value and structure of carbon black.

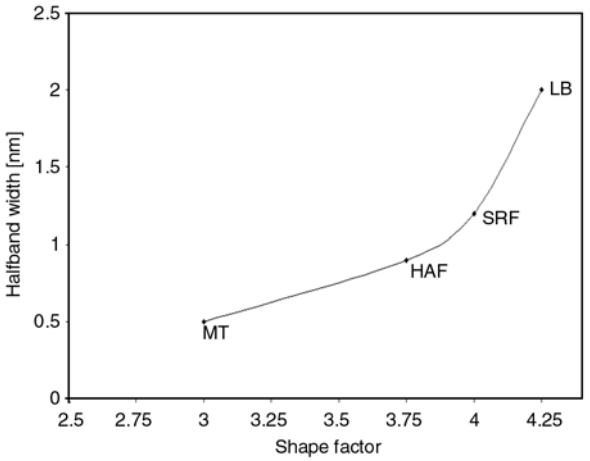

Figure 7. Relative Crystalline region expressed as half-band width of X-ray pattern

References

[1] Leblanc J. L.: Rubber-filler interactions and rheological properties in filled compounds. Progress in Polymer Science, **27**, 627–687 (2002). DOI: 10.1016/S0079-6700(01)00040-5

[2] Osman M. A., Attallah A.: Interparticle and particle-matrix interactions in polyethylene reinforcement and viscoelasticity. Polymer, **46**, 9476–9488 (2005). DOI: 10.1016/j.polymer.2005.07.030

[3] Oono R.: Distribution of carbon black in SBR. Journal of Applied Polymer Science, **21**, 1743–1749 (2003). DOI: 10.1002/app.1977.070210702

[4] Gruber T., C., Herd C. R.: Anisometry measurements in carbon black aggregate populations. Rubber Chemistry and Technology, **70**, 727–746 (2000).

[5] Donnet J-B., Bansal R. C., Wang M-J.: Carbon Black Science and Technology. Marcel Dekker, New York (1993).

[6] Vilgis T. A.: Time scales in the reinforcement of elastomers. Polymer, **46**, 4223–4229 (2005). DOI: 10.1016/j.polymer.2005.02.060

[7] Eirich F. R.: Science and technology of rubber. Academic Press, New York (1978).

[8] Zhang A., Wang L., Lin Y., Mi X.: Carbon black filled powdered natural rubber: Preperation, particle size distribution, mechanical properties and structures. Journal of Applied Polymer Science, **101**, 1763–1774 (2006). DOI: 10.1002/app.23516

[9] Kohjiya S., Katoh A., Suda T., Shimanuki J., Ikeda Y.: Visualization of carbon black networks in rubbery matrix by skeletonisation of 3D TEM image. Polymer, **47**, 3298-3301 (2006).
DOI: 10.1016/j.polymer.2006.03.008

[10] Rehner J.: Theory of filler reinforcement in natural and synthetic. The stress in and about particles. Journal of Applied Physics, **14**, 638–645 (1943).
DOI: 10.1063/1.1714942

[11] Smallwood H. M.: Limiting law of the reinforcement of rubber. Journal of Applied Physics, **15**, 758–766 (1944).
DOI: 10.1063/1.1707385

[12] Guth E.: Theory of filler reinforcement. Journal of Applied Physics, **16**, 20–25 (1945).
DOI: 10.1063/1.1707495

[13] Mullins L., Tobin N. R.: Stress softening in rubber vulcanizates. Part I. Use of a strain amplification factor to describe the elastic behavior of filler-reinforced vulcanized rubber. Journal of Applied Polymer Science, **9**, 2993–3009 (1965).
DOI: 10.1002/app.1965.070090906

[14] Ahmed S., Jones F. R.: A review of particulate reinforcement theories for polymer. Journal of Materials Science, **25**, 4933–4942 (1990).
DOI: 10.1007/BF00580110

[15] Mooney M.: The viscosity of a concentrated suspension of spherical particles. Journal of Colloid Science, **6**, 162–170 (1951).
DOI: 10.1016/0095-8522(51)90036-0

[16] Oberdisse J.: Structure and rheological properties of latex-silica nanocomposites films: Stress-strain isotherms. Macromolecules, **35**, 9441–9450 (2002).
DOI: 10.1021/ma020635d

[17] Oberdisse J., El Harrak A., Carrot G., Jestin J., Boué F.: Structure and rheological properties of soft-hard nanocomposites: Influence of aggregation and interfacial modification. Polymer, **46**, 6695–6705 (2005).
DOI: 10.1016/j.polymer.2005.05.023

[18] Medalia A. I.: Morphology of aggregates. I. Calculations of shape and bulkiness factore; Application to computer-simulated random flocs. Journal of Colloid and Interface Science, **24**, 393–404 (1967).
DOI: 10.1016/0021-9797(67)90267-6

[19] Medalia A. I.: Morphology of aggregates. IV. Effective volume of aggregates of carbon black from electron microscopy; Application to vehicle adsorption and to die swell of filled rubber. Journal of Colloid and Interface Science, **32**, 115–131 (1970).
DOI: 10.1016/0021-9797(70)90108-6

[20] Wolff S., Wang M. J.: Carbon black reinforcement of elastomers. in 'Carbon black' (eds: Donnet J-B., Bansal R. C., Wang M-J.) Marcel Dekker, New York (1993).

[21] Dannenberg E. M.: Carbon-black treadwear ratings from laboratory tests. Rubber Chemistry and Technology, **59**, 497–511 (1986).

[22] Huang J-C.: Carbon black filled conducting polymers and polymer blends. Advances in Polymer Technology, **21**, 299–313 (2002).
DOI: 10.1002/adv.10025

[23] Dannenberg E. M.: Bound rubber and carbon-black reinforcement. Rubber Chemistry and Technology, **59**, 512–524 (1986).

[24] Donnet J., Vidal A.: Carbon black: Surface properties and interactions within elastomers. in 'Advances in polymer science' (eds: Abe A., Albertsson A-C., Duncan R., Dusek K., de Jeu W. H., Kausch H-H., Kobayashi S., Lee K-S., Leibler L., Long T. E., Manners I., Möller M., Nuyken O., Terentjev E. M., Voit B., Wegner G., Wiesner U.) Springer, Berlin, 103–127 (1986).
DOI: 10.1007/3-540-15830-8

[25] Edwards D. C.: Polymer-filler interaction in rubber reinforcement. Journal of Materials Science, **25**, 4175–4185 (1990).
DOI: 10.1007/BF00581070

[26] Li Z. H., Zhang J., Chen S. J.: Effects of carbon blacks with various structures on vulcanization and reinforcement of filled ethylene-propylene-diene rubber. Express Polymer Letters, **2**, 695–704 (2008).
DOI: 10.3144/expresspolymlett.2008.83

[27] Donnet J-B.: Fifty years of research and progress on carbon black. Carbon, **32**, 1305–1310 (1994).
DOI: 10.1016/0008-6223(94)90116-3

[28] Bourrat X.: Electrically conductive grades of carbon black structure and properties. Carbon, **31**, 287–302 (1993).
DOI: 10.1016/0008-6223(93)90034-8

[29] Zhang W., Dehghani-Sanij A. A., Blackburn R.: Carbon based conductive polymer composites. Journal of Materials Science, **42**, 3408–3418 (2007).
DOI: 10.1007/s10853-007-1688-5

[30] Kagjiya T., Nishimoto S., Watanabe Y., Kato M.: Importance of the amorphous fraction of polypropylene in the resistance of radiation-induced oxidative degradation. Polymer Degradation and Stability, **12**, 261–275 (1985).
DOI: 10.1016/0141-3910(85)90094-1

[31] El-Zaher N. A., Micheal M. N.: Time optimization of UV-ozone pretreatment for improving wool fabrics properties. Journal of Applied Polymer Science, **85**, 1469–1476 (2002).
DOI: 10.1002/app.10750

[32] Biscoe J., Warren B. E.: An X-ray study of carbon black. Journal of Applied Physics, **13**, 364–371 (1942).
DOI: 10.1063/1.1714879

[33] Ungár T., Gubicza J., Tichy G., Pantea C., Zerda T. W.: Size and shape of crystallites and internal stresses in carbon black. Composites Part A: Applied Science and Manufacturing, **36**, 431–436 (2005).
DOI: 10.1016/j.compositesa.2004.10.017

eXPRESS Polymer Letters Vol.3, No.3 (2009) 159–167
Available online at www.expresspolymlett.com
DOI: 10.3144/expresspolymlett.2009.21

Synthesis, characterization and photopolymerization of vinyl functionalized poly (ε-caprolactone)

S. S. Liow[*1], *L. K. Widjaja*[1], *V. T. Lipik*[1], *M. J. M. Abadie*[1,2]

[1]School of Materials Science & Engineering, MSE/NTU, Block N4.1, 50 Nanyang Avenue, Nanyang Technological University, Singapore 639798, Singapore
[2]Laboratory of Polymer Science and Advanced Organic Materials, LEMP/MAO, Université Montpellier 2, S.T.L., Place Bataillon, 34095 Montpellier Cedex 05, France

Received 26 December 2008; accepted in revised form 9 February 2009

Abstract. Vinyl functionalized poly (ε-caprolactone) with molar mass ranging from 500–5000 Da were synthesized by ring opening polymerization and further photopolymerized. One-step synthesis and functionalization is achieved based on ring opening polymerization (ROP). Hydroxyl butyl vinyl ether (HBVE) was employed to play the role as the initiator of ROP, and photo-curable functional group. The presence of CH_2=CH peak in Fourier Transform Infrared (FTIR) spectra confirmed that vinyl end groups were successfully attached to poly (ε-caprolactone) (PCL) macromolecule. Kinetic parameters of cationic photopolymerization of vinyl functionalized PCL were investigated. The activation energy was estimated at 11.33 kJ/mol, by assuming the cationic system followed second-order autocatalytic model.

Keywords: *tailor-made polymers, poly (ε-caprolactone), cationic photopolymerization, functionalization; curing kinetics*

1. Introduction

Aliphatic polyesters, such as Polyglycolide (PGA), Polylactide (PLA), Poly (ε-caprolactone) (PCL) and their copolymers have received great interest in biomedical applications due to their good biocompatibility [1] and bioabsorbability. They degrade mainly by hydrolysis of ester linkages, yield hydroxyl carboxylic acids, which in most cases are ultimately metabolized [2]. The functionalization of oligomers such as ε-caprolactone, with unsaturated groups and subsequent Ultraviolet (UV) curing [3, 4] or polymerization [5, 6] has been studied. Especially, UV curing is interesting since it usually provides fast, well-controlled and low energy consumption process, capable of forming thin films or predefined patterns, and can be carried out at low temperatures [7]. Our research focuses on the development of novel controlled drug release system based on mono-functionalized polyesters/ copolyesters and successive cationic UV grafting to yield fully or partially bioabsorbable therapeutic multilayered surface coatings, with variable rate of degradation. If this polyester/ copolyester is multi-functionalized, consequent UV crosslinking can yield fully bioabsorbable polymeric network, which is suitable for biomedical applications such as tissue engineering scaffolds, cell encapsulations and short term drug delivery vehicles.

To prepare polymers with variable rates of degradation, most studies have focused on copolymerization [8–11]. Copolymerization allows blending of two or more polymers, in order to achieve variable degradation patterns. In-depth research of degradation behaviors of the copolymers in different compositions and prolonged synthesis procedure are expected. It could be more convenient, if the vari-

*Corresponding author, e-mail: Liow0019@ntu.edu.sg

able rate of degradation is obtained by formation of multilayered polymeric coatings, by rapid and well-controlled UV curing.

Photo-curable functional groups, such as methacrylates have been used most often as unsaturated group attached on precursor oligomers [4–6]. Functionalization with coumarin and phenylazide has been reported as well [12, 13]. In these cases, free radical photopolymerization was employed. When cured radically, these photoreactive functions are subjected to oxygen and impurities inhibition, which could lead to incomplete conversion. Immune inflammation reaction was reported to be related to the leach out of monomers or unreacted oligomers from polymeric implants. Another anticipated risk of acrylates is a higher level of skin sensitization as compared to most vinyl ethers [14]. In addition, the synthesis of acrylates, coumarin and phenylazide functionalized precursor oligomers usually involved two-steps reaction: precursor oligomers synthesis and subsequent functionalization. Longer preparation time and tedious purification are expected.

To overcome these problems, we are investigating an alternative UV curing method – cationic photopolymerization, where mono-functionalized oligocaprolactone was used as precursor oligomers. The main advantage of cationic photopolymerization is that it is not inhibited by oxygen and capable of 'dark curing'. Synthesis and functionalization can be achieved in one step, by using ROP. HBVE was employed to play the role as the initiator of ROP, and photo-curable functional group. Most vinyl ethers are expected to have a lower level of skin sensitization as compared to acrylates.

In this study, we report the feasibility to photopolymerize precursor oligomers. The kinetics of cationic photopolymerization of HBVE functionalized PCL (vinyl-PCL) will be discussed.

2. Materials and methods

2.1. Materials

Epsilon-caprolactone monomer (99%) was purchased from Fluka, Singapore and used without further purification. The initiator 4-hydroxybutyl vinyl ether (stabilized with 0.01% KOH) (HBVE) was obtained from BASF, Canada. Tin (II) 2-ethylhexanoate ($SnOct_2$) was purchased from Sigma, Singapore. Toluene was purified by distillation. Chloroform, methanol and dimethyl sulfoxide (DMSO) were of analytical grade and used as received. The photoinitiator: bis [4(diphenylsulfonio)-phenyl] sulfide-bis-hexafluoroantimonate 50% solution in propylene carbonate supplied as Cyracure® UVI 6976 by Union Carbide (USA) was used without further purification.

2.2. ROP and functionalization of vinyl-PCL

To functionalize PCL of 2000 g/mol, 5 mmol of HBVE as initiator, 0.5 mmol of $SnOct_2$ as catalyst and 25 ml of freshly distilled toluene were charged into a 50 ml three neck flask. The flask was evacuated by vacuum, and purged with nitrogen before being placed into an oil bath, at 80°C. After 30 minutes, 10 g of ε-caprolactone monomer was charged into the reaction flask. The reaction was kept at 110°C for 24 h. The crude products were dissolved in chloroform and precipitated in a four-fold excess of methanol. The polymer was dried at 40°C under vacuum for 24 h.

2.3. Measurements

The molar weights (number average molar weight M_n and weight average molar weight M_w) and polydispersity index (PDI) were determined by Size Exclusion Chromatograph (SEC) (Agilent GPC 1100 series), using monodisperse polystyrene standard for calibration. Measurements were made at room temperature with chloroform as solvent (1 ml: 1 mg). Matrix Assisted Laser Desorption/Ionization-Time Of Flight (MALDI-TOF) mass spectrometry was performed on Shimadzu Biotech (Axima-ToF^2) in linear mode. MALDI-TOF mass-spectra were acquired by averaging at least 100 laser shots. 2,5-dihydroxyl benzoic acid was used as matrix and tetrahydrofuran as solvent. Sodium chloride was dissolved in methanol and used as the ionizing agent. Samples were prepared by mixing 20 µl of polymer solution in tetrahydrofuran (2 mg/ml) with 20 µl of matrix solution (10 mg/ml) and 1 µl of a solution of ionizing agent (1 mg/ml). Then 1 ml of these mixtures was deposited on a target plate and allowed to dry in air at room temperature. Calibration was made with polyethylene glycol 10 kDalton. Nuclear magnetic resonances based on proton (^{1}H NMR) spectra were recorded in $CDCl_3$ on a Bruker 400 MHz Spectrometer.

Glass and melt transition temperatures were determined by Differential Scanning Calorimetry (TA Instruments Q10-0095). The measurements were carried out from –90 to 120°C at heating rate of 10°C/min. Functional end groups were determined by Fourier Transform Infrared Spectroscopy (FTIR) (Perkin Elmer FTIR Spectrum GX spectrometer), using powdered potassium bromide (KBr) as matrix.

2.4. Photopolymerization of vinyl-PCL

Differential Scanning PhotoCalorimetry (DPC) (TA Instruments MDSC-2920 equipped with a photocalorimetric accessory) was used to investigate the kinetics of cationic photopolymerization of vinyl group present in monofunctional PCL 0.5, 2 and 5 kDa. Pulverized vinyl-PCL was dissolved in two solvents; non-photoreactive DMSO and photoreactive HBVE respectively. The composition is tabulated in Table 1.

The initiation light source was a 200 W high-pressure mercury lamp, which gave a UV light intensity over wavelength range of 200–440 nm. 3.0 mg of samples were placed in aluminum standard pans covered with a disc of polyethyleneterephthalate (PET) foil to maintain equal distribution of solution layer under investigation. The samples were exposed to UV light of intensity in the range of 25 mW/cm^2, for 5 minutes. Also, samples were subjected to 1 minute isothermal treatment prior to and after the UV exposure, to ensure constant temperature. A nitrogen flux of 50 cm^3/min assured homogeneity of temperature in the measuring cell.

2.4.1. Calculations

The degree of conversion (α) can be obtained from the DPC exotherm as shown in Equation (1):

$$\alpha = \frac{\Delta H_{\exp}}{\Delta H_0} \tag{1}$$

and the theoretical enthalpy at full conversion of vinyl double bonds (ΔH_0) is determined by Equation (2):

$$\Delta H_0 = f\left(\frac{\Delta H_{Tf}}{m}\right) \tag{2}$$

where f is the functionality; ΔH_{Tf} is the theoretical enthalpy of vinyl ether function, 14.3 kcal/mol [15] and m is the molar weight of each macromolecule. List of theoretical enthalpy used in this study is calculated using Equation (2) and tabulated in Table 2. As an example for the HBVE functionalized PCL (M_n 2000 Da) in DMSO solution (80/20), the theoretical enthalpy is given by Equation (3):

$$\Delta H_0 = 1 \cdot 0.8\left(\frac{14300 \cdot 4.1839}{2000+116}\right) = 22.62\left[\frac{\mathrm{J}}{\mathrm{g}}\right] \tag{3}$$

The autocatalytic model as shown in Equation (4) was used to calculate the kinetic parameters. Autocatalytic model assumes that in a curing process, the measured heat flow is proportional to the conversion rate ($d\alpha/dt$). This assumption is valid if the testing material exhibiting single reaction without any other enthalpic events, such as evaporation of solvent or significant changes in heat capacity with conversion [16] (Equation (4)):

$$\frac{d\alpha_{(t,T)}}{dt} = k_{(T)}\alpha^m(1-\alpha)^n \tag{4}$$

where $d\alpha/dt$, the reaction rate [min^{-1}]; α, the fractional conversion after time t; $k_{(T)}$, temperature dependent rate coefficient [min^{-1}]; n, m, reaction orders of propagation and initiation respectively. Second-order autocatalytic model was assumed by fixing $(m + n = 2)$.Temperature dependent rate coefficient $k_{(T)}$ is assumed to follow the Arrhenius equation (Equation (5)):

Table 2. Theoretical enthalpies (ΔH_0) at full conversion calculated from Equation (2)

Compound	Theoretical enthalpy ΔH_0 [J/g]
PCL 2k DMSO 80/20	22.62
PCL 2k HBVE 50/50	272.03
PCL Neat Resin HBVE 50/50	257.89

Table 1. Compositions of vinyl-PCL with non-photoreactive and photoreactive solvent

Compound	PCL [wt%]	Solvent [wt%]	Photo reactive solvent	Initiator UVI 6976 [wt%]
PCL 2k/DMSO	80	20	No	4
PCL 2k/HBVE	50	50	Yes	4

$$k_{(T)} = Ae^{-\frac{E_a}{RT}} \quad (5)$$

where E_a is the activation energy, A is the frequency factor, R is the ideal gas constant and T is the absolute temperature [K].

3. Results and discussion

In the preliminary experiments, we functionalized PCL by using HBVE in the presence of $SnOct_2$. The resulting vinyl-PCL was characterized by its molar weights, functional end groups and transition temperatures, using several techniques including SEC, MALDI-TOF, FTIR and Differential Scanning Calorimetry (DSC). Linearly grafted polymer was obtained by photopolymerization of vinyl-PCL under UV exposure.

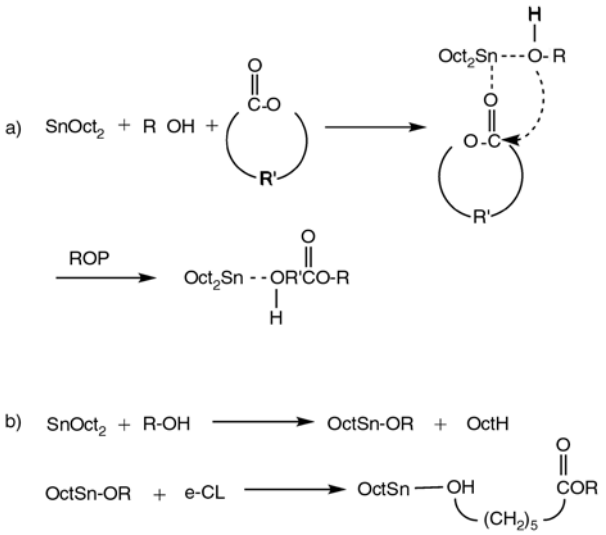

Figure 2. The main ROP mechanism proposals with $SnOct_2$ as catalyst, a) complexation of a monomer and alcohol prior to ROP [18] and b) formation of a tin-alkoxide before ROP of ε-CL [19]

3.1. ROP and functionalization of vinyl-PCL

ROP of cyclic ester makes it possible to prepare polyesters with defined molar weights, low polydispersity index, and functionalized end groups, due to the absence or very limited side reactions and by products [2]. To enable photo curing of PCL, monofunctional vinyl ether, in this case is HBVE, was incorporated into each PCL chain. Targeted molar weight was calculated using Equation (6):

$$DP = \frac{MW_{targeted}}{m_{monomer}} = \frac{[M]}{x[I]} \quad (6)$$

where DP is the degree of polymerization, $m_{monomer}$, molar weight of caprolactone monomer; $[M]$, monomer concentration; x, functionality of initiator (in this case $x = 1$ since monofuctional HBVE was used as initiator); $[I]$, initiator concentration. Figure 1 shows the reaction scheme.

In ROP of PCL, we used HBVE as initiator, and $SnOct_2$ as catalyst. $SnOct_2$ is now widely used as catalyst of degradable polymer synthesis because stannous salts have been approved for pharmaceutical applications [17]. The main mechanisms of $SnOct_2$ catalyzed ROP proposed in literatures [18, 19] are shown in Figure 2.

PCL with wide range of molar weights ranging from 0.5–40 kDa were successfully synthesized but only low molar weights PCL (0.5, 2 and 5 kDa) were used for further photo grafting. In this study, we defined low molar weight PCL as oligomer hav-

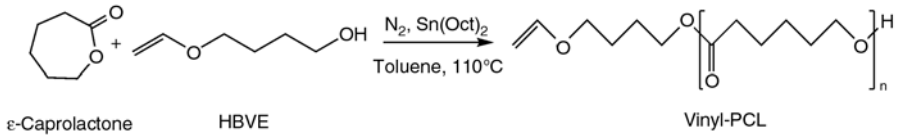

Figure 1. Reaction scheme for ROP of vinyl-PCL using HBVE as initiator, and $SnOct_2$ as catalyst

Table 3. Molecular mass and melting transition temperatures of vinyl-PCL prepolymer

		SEC			^{1}H NMR	MALDI-TOF	
Target M_n [kDa]	**[HBVE]/ [$SnOct_2$]**	**M_n [g/mol]**	**M_w [g/mol]**	**Poly Dispersity Index (PDI)**	**M_n [g/mol]**	**M_n [g/mol]**	**T_m [°C]**
0.5	2	1898	3502	1.84	3609	612	40.29
2	2	7091	11189	1.57	3995	1011	57.69
5	10	4574	10051	2.20	4643	ND[a]	58.28

[a]ND – not detected

ing molar weight from 500–5000 Da. An overview of the properties of vinyl-PCL is presented in Table 3.

For PCL 5 kDa both molar weights obtained from SEC and NMR showed consistency with one another. Note that the experimental M_n follows closely to targeted value when molar ratio of HBVE/$SnOct_2$ is 10. It is observed in the PCL 0.5 kDa and PCL 2 kDa that M_n (detected by SEC and NMR) is higher than targeted value when molar ratio of HBVE/$SnOct_2$ was decreased to 2, where amount of $SnOct_2$ increased. In the presence of ROH (in our case is HBVE), if the proportion [ROH]/ [$SnOct_2$] does not exceed approximately 2, ROH acts mostly as a co-initiator, reacting with $SnOct_2$ [19]. The increased amount of $SnOct_2$ has probably initiated some macromolecules. This explained why M_n tends to be higher when [ROH]/[$SnOct_2$] ratio is 2. Above this ratio, ROH retains its function as an initiating compound [19].

PDI (M_w/M_n ratio) observed in all synthesized PCL were high. In the case of PCL 5 kDa, this could result from bimolecular transesterification in presence of $SnOct_2$, not shifting M_n but M_w [19]. $SnOct_2$ is well known for causing transesterification reactions at elevated temperatures [2]. For PCL 5 kDa, only MALDI spectra for low molar mass fraction were detected because of high PDI. Sometimes, the MALDI results are completely out of range for polymer with high PDI [20].

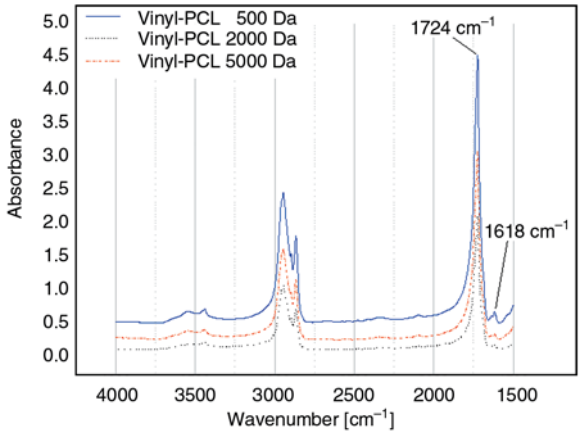

Figure 3. FTIR spectra of 0.5, 2 and 5 kDa vinyl-PCL

3.2. End group analysis by FTIR

It is known that vinyl ether is a function involved in cationic photopolymerization. From Figure 3, the low intensity peak at 1618 cm^{-1} corresponds to the vibration of the vinyl CH_2=CH double bonds, and the strong peak at 1725 cm^{-1} indicates vibration of abundant C=O ester bonds in PCL. This result shows that the vinyl group is successfully linked to PCL after ring opening polymerization.

3.3. Photopolymerization of vinyl-PCL

Before photopolymerization, two sets of samples were prepared by dissolving vinyl-PCL in DMSO and HBVE respectively. Upon UV exposure, polymerization of double bonds leads to formation of linearly grafted vinyl-PCL as shown in Figure 4 and Figure 5.

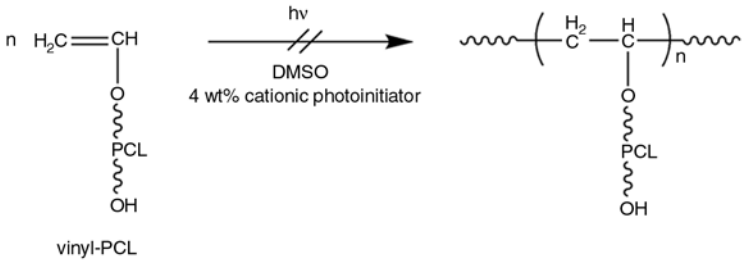

Figure 4. Typical photopolymerization reaction of vinyl-PCL in non-photo reactive solvent (DMSO)

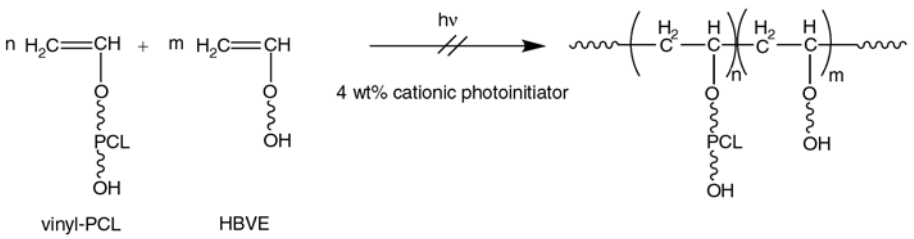

Figure 5. Typical photopolymerization reaction of vinyl-PCL in photo reactive solvent (HBVE)

3.3.1. Photopolymerization in non-photo reactive solvent (DMSO)

Photocuring of the vinyl-PCL in DMSO in presence of cationic photoinitiator (Cyracure® UVI 6976) has been performed. Figure 6 shows typical DPC exotherm plot of PCL 2 kDa photopolymerized in non-reactive solvent (DMSO), initiated by UVI 6976. The total area under the curve corresponds to the polymerization enthalpy (ΔH_{exp}) of the sample. Broad peak is obtained indicating low reactivity of the photopolymerization system. Low reactivity of the system is further presented by long induction time and low rate coefficients (k), as compared to HBVE system. It is in fact reasonable since the photo reactive species (vinyl double bonds) is only a small portion in a long macromer.

From the plot of heat flow over time, one can obtain information such as induction time (time of 1% monomer conversion), polymerization enthalpy, percentage of conversion and reaction rate coefficient (k), as shown in Table 4. Conversion was calculated from Equation (1). Average conversions range from 73–97% within 5 minutes of UV exposure.

On the other hand, note that cationic photopolymerization continues curing long after exposure once initiated [21, 22]. This is termed as 'dark curing'. Therefore, conversion of vinyl double bonds is expected to continue further until complete conversion after exposure. In addition, cationic photopolymerization is not inhibited by traces of oxygen in the air or radical impurities but inhibiting and retarding effects or chain transfer reactions were observed with bases, water, alcohols [23].

In cationic polymerization, the reaction rate coefficient (k) is affected by the nature of counter ion [24]. Lazauskaité and coworkers have examined the kinetic parameters of cationic photopolymerization of epoxies monomer initiated by photoinitiator having the same counter ions in this study [25]. At 60°C, both k values are consistent with each other.

The reaction rate coefficient (k) is assumed to follow Arrhenius equation (Equation (4)). An estimation of activation energy (E_a) was obtained as 11.33 kJ/mol by fitting a linear relationship of ln$k$ and reciprocal of temperature, as shown in Figure 7. Estimation of activation energy is considered low as compared to vinyl ether function alone (14.3 kcal/mol = 59.83 kJ/mol) [15]. Lower activa-

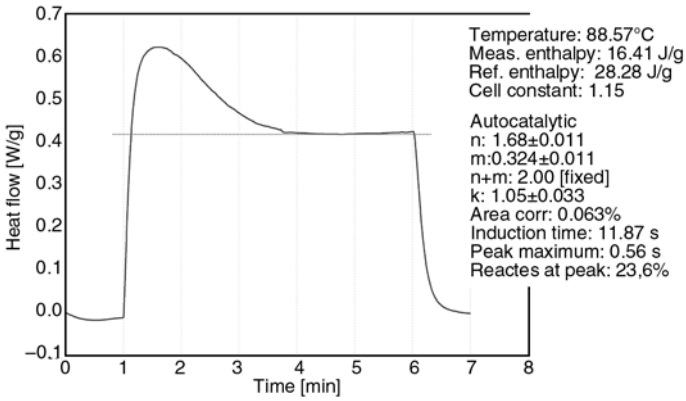

Figure 6. Typical DSC exotherm of vinyl-PCL 2 kDa in DMSO solution at 90°C. Exothermic peak is pointing upwards.

Table 4. Kinetic parameters of the second-order autocatalytic model for the photopolymerization of vinyl-PCL in DMSO solution with 4 wt% UVI 6976 obtained by TA specialty library analysis

Temperature of experiment [°C]	Enthalpy, ΔH_{exp} [J/g]	Peak maximum [s]	Induction time [s]	Reacted at peak [%]	Rate coefficient, k [min^{-1}]	m	Conversion[b]
58.9	21.9	0.47	11.2	14.0	2.20	0.637	0.967
68.8	21.4	0.49	11.7	16.2	2.48	0.623	0.947
78.6	18.4	0.50	10.7	18.4	2.65	0.625	0.815
88.6	16.5	0.55	10.6	25.0	3.44	0.683	0.728
98.4	17.1	0.67	10.9	30.5	3.23	0.706	0.755

E_a= 11.33 ± 2.44 kJ/mol, R^2: 0.88

Frequency factor, A: 133.75

[b] Conversion within 5 minutes of UV exposure was calculated using Equation (1)

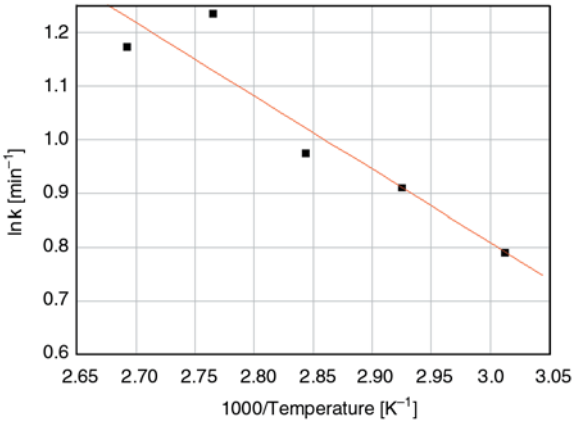

Figure 7. ln*k* vs. 1/*T* Arrhenius plot

tion energy indicates a higher reactivity system. But, vinyl-PCL oligomeric system could not be more easily polymerized than the vinyl ether monomer.

Unlike monomeric system studied by Lazauskaité, oligomeric system has lower diffusivity of active centers than monomeric system, it is necessary to take into account the diffusion controlled reaction. According to Rabinowitch [26] the overall reaction rate coefficient, ke, can be expressed as Equation (7):

$$\frac{1}{k_e}=\frac{1}{k_{chem}}+\frac{1}{k_{diff}} \tag{7}$$

where k_{chem} is the chemically controlled and k_{diff} is the diffusion controlled rate coefficient, and k_{chem} follows an Arrhenius temperature dependence. System with low diffusivity can decrease the overall rate coefficient significantly, and thus affect temperature dependence, resulting in low activation energy estimation.

3.3.2. Photopolymerization in photoreactive solvent (HBVE)

Photocuring of the vinyl-PCL in HBVE in presence of cationic photoinitiator (Cyracure® UVI 6976) has been performed. Photopolymerization in HBVE follows the reaction scheme presented in Figure 5. Since HBVE is photoreactive, it is expected to receive enthalpy contributed by polymerization of HBVE double bonds in addition to vinyl-PCL double bonds. Figure 8 shows a typical exothermic plot of this system. Sharper peak is obtained as compared to DMSO system, indicating higher reactivity of the photopolymerization system. High reactivity of the system is further presented by the lower induction time and higher rate coefficients (*k*), as compared to DMSO system in Table 4. It is expected since both double bonds from HBVE monomers and vinyl-PCL were participating in photopolymerization.

The kinetic results of vinyl-PCL in HBVE solution is compared with neat resin system in HBVE solution initiated by the same initiator, as shown in Table 5. Average enthalpy of vinyl-PCL is higher than the neat resin system. It is expected that the difference in enthalpy is contributed when vinyl-PCL photopolymerized. However, the difference is too small to be conclusive. Therefore it cannot be concluded here from results in Table 5 that the double bonds in vinyl-PCL were photopolymerized successfully.

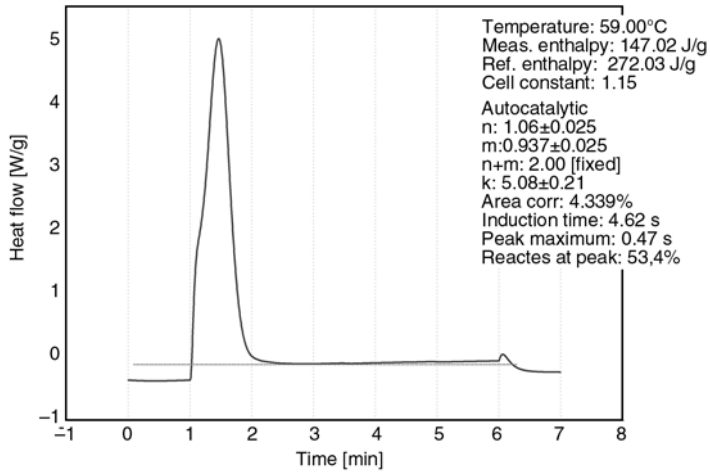

Figure 8. Typical DSC exotherm of vinyl-PCL 2 kDa in HBVE solution at 60°C. Exothermic peak is pointing upwards.

Table 5. Comparision of kinetic parameters of vinyl-PCL with PCL neat resin, both in HBVE reactive solvent at 60°C obtained by TA specialty library analysis

Compound	Enthalpy ΔH_{exp} [J/g]	Peak maximum [s]	Induction time [s]	Reacted at peak [%]	Rate coefficient k [min^{-1}]	m	Conversion[b]
PCL 2kDa HBVE 50/50	155.5 ± 11.9	0.48	4.80	0.519	6.30	0.985	0.58
PCL NR HBVE 50/50	151.2 ± 12.1	0.22	3.63	0.452	10.92	0.689	0.58

[b] Conversion within 5 minutes of UV exposure was calculated using Equation (1)

4. Conclusions

Our preliminary results have proved that cationic photopolymerization is capable of curing vinyl ether functionalized precursor oligomers with high conversion in DMSO solution. One-step synthesis and functionalization is established by using hydroxyl butyl vinyl ether as initiator and photocurable functional group. The presence of CH_2=CH peak in FTIR spectra confirmed that vinyl end groups were successfully attached to PCL macromolecule.

Photopolymerization kinetics of vinyl-PCL was studied in both DMSO and HBVE solution. Photocuring of the vinyl-PCL in DMSO in presence of cationic photoinitiator (Cyracure® UVI 6976) yield polymerization enthalpy of 17–22 J/g. The activation energy was calculated to be 11.33 kJ/mol, by assuming the cationic system followed autocatalytic model. In HBVE solution, it cannot be concluded that vinyl-PCL contributed to the resulted polymerization enthalpy, in the comparison to neat resin system. This is mainly due to the fact that the enthalpy contribution of vinyl-PCL is too small compare to HBVE.

References

[1] Serrano M. C., Pagani R., Vallet-Regí M., Peña J., Rámila A., Izquierdo I., Portolés M. T.: In vitro biocompatibility assessment of poly([epsilon]-caprolactone) films using L929 mouse fibroblasts. Biomaterials, **25**, 5603–5611 (2004). DOI: 10.1016/j.biomaterials.2004.01.037

[2] Albertsson A. C.: Degradable aliphatic polyesters. Springer, Berlin/Heidelberg (2002).

[3] Grijpma D. W., Hou Q., Feijen J.: Preparation of biodegradable networks by photo-crosslinking lactide, ε-caprolactone and trimethylene carbonate-based oligomers functionalized with fumaric acid monoethyl ester. Biomaterials, **26**, 2795–2802 (2005). DOI: 10.1016/j.biomaterials.2004.08.002

[4] Sawhney A. S., Pathak C. P., Hubbell J. A.: Bioerodible hydrogels based on photopolymerized poly(ethylene glycol)-co-poly(α-hydroxy acid) diacrylate macromers. Macromolecules, **26**, 581–587 (1993). DOI: 10.1021/ma00056a005

[5] Storey R. F., Warren S. C., Allison C. J., Wiggins J. S., Puckett A. D.: Synthesis of bioabsorbable networks from methacrylate-endcapped polyesters. Polymer, **34**, 4365–4372 (1993). DOI: 10.1016/0032-3861(93)90203-M

[6] Helminen A. O., Korhonen H., Seppala J. V.: Cross-linked poly (ε-caprolactone/D,L-lactide) copolymers with elastic properties. Macromolecular Chemistry and Physics, **203**, 2630–2639 (2002). DOI: 10.1002/macp.200290039

[7] Schwalm R.: UV Coatings: Basics, recent developments and new applications. Elsevier, Amsterdam (2007).

[8] Hakkarainen M., Albertsson A-C., Karlsson S.: Weight losses and molecular weight changes correlated with the evolution of hydroxyacids in simulated *in vivo* degradation of homo- and copolymers of PLA and PGA. Polymer Degradation and Stability, **52**, 283–291 (1996). DOI: 10.1016/0141-3910(96)00009-2

[9] Dirk W., Grijpma A. J. P.: (Co)polymers of L-lactide 1. Synthesis, thermal properties and hydrolytic degradation. Macromolecular Chemistry and Physics, **195**, 1633–1647 (1994). DOI: 10.1002/macp.1994.021950515

[10] Pitt G. G., Gratzl M. M., Kimmel G. L., Surles J., Sohindler A.: Aliphatic polyesters II. The degradation of poly (DL-lactide), poly (ε-caprolactone), and their copolymers *in vivo*. Biomaterials, **2**, 215–220 (1981). DOI: 10.1016/0142-9612(81)90060-0

[11] Iojoiu C., Cade D., Fessi H., Hamaide T.: Synthesis of oligocaprolactone vinyl ether macromonomers and their use for indomethacin encapsulation in polymer nanoparticles based on polycaprolactone macromonomer-maleic anhydride-*N*-vinyl pyrrolidone terpolymers. Polymer International, **55**, 222–228 (2006). DOI: 10.1002/pi.1964

[12] Matsuda T., Mizutani M., Arnold S. C.: Molecular design of photocurable liquid biodegradable copolymers. 1. Synthesis and photocuring characteristics. Macromolecules, **33**, 795–800 (2000). DOI: 10.1021/ma991404i

[13] Mizutani M., Arnold S. C., Matsuda T.: Liquid, phenylazide-end-capped copolymers of ε-caprolactone and trimethylene carbonate: Preparation, photocuring characteristics, and surface layering. Biomacromolecules, **3**, 668–675 (2002). DOI: 10.1021/bm0101670

[14] Blyler Jr. L. L., Paczkowski M. A., Simoff D. A., Varlemann U., Wang N. P.: Vinyl ether terminated oligomers and polymers. U.S. Patent 5989627, USA (1999).

[15] Hoyle C. E.: Calorimetric analysis of photopolymerization. in 'Radiation curing: Science and technology' (ed.: Pappas S. P.) Plenum Press, New York, 57–133 (1992).

[16] Cho J-D., Hong J-W.: Curing kinetics of UV-initiated cationic photopolymerization of divinyl ether photosensitized by thioxanthone. Journal of Applied Polymer Science, **97**, 1345–1351 (2005). DOI: 10.1002/app.21838

[17] Wu X. S.: Synthesis and properties of biodegradable lactic/glycolic acid polymers. in 'Encyclopedic handbook of biomaterials and bioengineering' (ed.: Wise D. L.) 1015–1054 (1995).

[18] Kricheldorf H. R., Kreiser-Saunders I., Stricker A.: Polylactones 48. $SnOct_2$-initiated polymerizations of lactide: A mechanistic study. Macromolecules, **33**, 702–709 (2000). DOI: 10.1021/ma991181w

[19] Kowalski A., Duda A., Penczek S.: Kinetics and mechanism of cyclic esters polymerization initiated with tin (II) octoate, 1: Polymerization of ε-caprolactone. Macromolecular Rapid Communications, **19**, 567–572 (1998). DOI: 10.1002/(SICI)1521-3927(19981101)19:11<567::AID-MARC567>3.0.CO;2-T

[20] Pasch H., Schrepp W.: MALDI-TOF mass spectrometry of synthetic polymers. Springer, Berlin (2003). DOI: 10.1007/s00216-004-3038-7

[21] Abadie M. J. M., Voytekunas V. Y.: New trends in UV curing. Eurasian Chemico-Technological Journal, **6**, 67–77 (2004).

[22] Decker C.: Photoinitiated crosslinking polymerisation. Progress in Polymer Science, **21**, 593–650 (1996). DOI: 10.1016/0079-6700(95)00027-5

[23] Fouassier J-P.: Photoinitiation, photopolymerization, and photocuring: Fundamentals and applications. Hanser, Cincinnati (1995).

[24] Kim Y-M., Kris Kostanski L., MacGregor J. F.: Kinetic studies of cationic photopolymerizations of cycloaliphatic epoxide, triethyleneglycol methyl vinyl ether, and cyclohexene oxide. Polymer Engineering and Science, **45**, 1546–1555 (2005). DOI: 10.1002/pen.20383

[25] Lazauskaité R., Budreckiené R., Grazulevicius J. V., Abadie M. J. M.: Cationic photopolymerization of 1,2-epoxy-6-(9-carbazolyl)-4-oxahexane initiated by sulfonium salt and iron arene complex. Advanced Synthesis and Catalysis, **342**, 569–573 (2000). DOI: 10.1002/1521-3897(200006)342:6<569::AID-PRAC569>3.0.CO;2-J

[26] Rabinowitch E.: Collision, co-ordination, diffusion and reaction velocity in condensed systems. Transactions of the Faraday Society, **33**, 1225–1233 (1937). DOI: 10.1039/TF9373301225

eXPRESS Polymer Letters Vol.3, No.3 (2009) 168–176
Available online at www.expresspolymlett.com
DOI: 10.3144/expresspolymlett.2009.22

Swelling properties of acrylamide-N,N′-methylene bis(acrylamide) hydrogels synthesized by using meso-2,3-dimercaptosuccinic acid-cerium(IV) redox couple

*C. Özeroglu**, *A. Birdal*

Istanbul University, Faculty of Engineering, Department of Chemistry 34320 Avcilar Istanbul, Turkey

Received 6 January 2009; accepted in revised form 13 February 2009

Abstract. In this paper, meso-2,3-dimercaptosuccinic acid-Ce(IV) redox couple is used for crosslinking polymerization of acrylamide (AAm) with N,N′-methylene bis(acrylamide) (MBAA) in acid aqueous medium. We have investigated the effects of crosslinker ratio, acid concentration and the molar ratio of AAm/Ce(IV) on the swelling behaviors of the synthesized P(AAm-MBAA) hydrogels. The experimental results show that the increase in the n_{AAm}/n_{MBAA} and $n_{AAm}/n_{Ce(IV)}$ result in an increase in the swelling ratio and rate of resulting hydrogels. However, the swelling equilibrium ratio and rate have been decreased with increasing of acid concentration. The k and n values in the equation of swelling rate have been determined. The n exponent decreases with increasing crosslinker, initiator and acid concentrations whereas k values increase. Kinetics and equilibrium swelling values have been discussed in terms of reaction parameters.

Keywords: *polymer gels, meso-2,3-dimercaptosuccinic acid, redox initiator, acrylamide, swelling*

1. Introduction

Hydrogels that exhibit swelling changes in response to environmental changes such as temperature, pH, electrical field, radiation of UV or visible light, solvent composition, salt concentration and type of surfactants are promising as intelligent materials. As a result they attract increasing interest in various application areas such as drug delivery systems, separation operations in biotechnology, processing of agricultural products, conductive or superabsorbent composites, sensors and actuators [1–12]. The swelling equilibrium of gels is determined by both the free energy of elasticity and free energy of mixing. In acrylamide-N,N′-methylene bis(acrylamide) hydrogel/water system, water diffuses into the network by the forces determined by the difference of chemical potential of water inside and outside of the network. The swelling gel reaches the equilibrium state at higher concentration of water in gel phase. The contribution of elastic forces to the chemical potential of water prevents the polymer from becoming completely dissolved [2, 9, 13, 14]. Numerous scientists have made great effort to investigate the synthesis and swelling properties of gel particles. In the synthesis of gel particles, potassium persulfate (PPS) or ammonium persulfate (APS) with or without N,N,N′,N′-tetramethylenediamine (TEMED) initiator systems have been generally used [15–17]. Ceric salt-organic reducing agent containing thiol, hydroxyl, carboxyl and amine functional groups can be used for polymerization and copolymerization of vinyl monomers. However, ceric salt-organic reducing agent containing thiol functional group or groups are also new sources to initiate copolymerization of vinyl monomers at low tem-

*Corresponding author, e-mail: ozeroglu@istanbul.edu.tr

peratures. When reducing agent with thiol functional group is used in redox system of ceric salt-organic reducing agent, the formation of –S. radical is energetically most favorable due to low S–H bonding energy to initiate copolymerization of gel particles in acid-aqueous medium at lower temperatures [18–23].

The swelling of polymeric networks is influenced by the composition of the polymer i.e. by the synthetic conditions, such as the n_{AAm}/n_{MBAA} in polymeric networks and by the nature of swelling media. These types of hydrogels containing functional groups have a potential to be used as colon specific drug delivery devices and can be used for water absorption from oil-water emulsions [24–26].

In this communication, meso-2,3-dimercaptosuccinic acid-Ce(IV) redox couple was used to synthesize the crosslinked copolymer of acrylamide and N,N′-methylene bis(acrylamide) in acidic aqueous medium. The effect of parameters such as molar ratios of acrylamide to N,N′-methylene bis(acrylamide), acrylamide to cerium(IV) sulfate and the concentration of sulfuric acid were investigated. The swelling ratios and kinetics of hydrogels synthesized at different reaction parameters such as the n_{AAm}/n_{MBAA} at different initiator and acid concentrations, the concentration of sulfuric acid for $n_{AAm}/n_{MBAA} = 40$ at constant initiator concentration and the $n_{AAm}/n_{Ce(IV)}$ at constant acid and crosslinker concentration were studied.

2. Experimental

2.1. Materials

Acrylamide (Merck), N,N′-methylene bis(acrylamide) (Fluka), cerium(IV) sulfate (Merck) and meso-2,3-dimercaptosuccinic acid (Merck) were used as received and represented as AAm, MBAA, Ce(IV) and DMSA respectively in the text.

Sulfuric acid (Merck) with a purity of 98% was used in the redox reaction of meso-2,3-dimercaptosuccunic acid and cerium(IV) sulfate.

2.2. Preparation of P(AAm-MBAA) hydrogels

In order to prepare P(AAm-MBAA) hydrogels, the solution containing the calculated amount of Ce(IV) dissolved in acidic medium was added to the aqueous solution of acrylamide, N,N′-methylene bis(acrylamide) and meso-2,3-dimercaptosuccinic acid in a round bottomed flask equipped with a stirrer. For this purpose, the oxidant (cerium(IV) sulfate) was dissolved in a solution containing the calculated amount of sulfuric acid. The solution volume containing the oxidant was kept constant at 20 ml. The total volume of crosslinking polymerization solution was 100 ml. The synthesized P(AAm-MBAA) hydrogels were purified from contaminants by immersion and soaking for 4 hours (three times) in 300 ml of distilled water and dried at 60°C. After drying, the hydrogels were placed in the sintered glass funnels which were immersed in distilled water. The swelling of the hydrogels were monitored by mass measurements against time. In this study, swelling values at 167 hours have been taken as equilibrium swelling values of all hydrogels – although equilibrium of swelling of some hydrogels may need more time than 167 hours. Once the equilibrium was reached, the hydrogels were weighed, dried at 60°C in vacuum for 24 hours and re-weighted. The effects of physicochemical parameters on the swelling behaviors and kinetics have been investigated. These parameters are: the molar ratios of acrylamide/cerium(IV) sulfate ($n_{AAm}/n_{Ce(IV)} = 100$ and 200) at constant crosslinker and acid concentrations, the concentration of sulfuric acid ($C_{H_2SO_4} = 0.0125$ and 0.025 mol/l) at the $n_{AAm}/n_{MBAA} = 40$ and the molar ratios of acrylamide to N,N′-methylene bis(acrylamide) for different acid and initiator concentrations.

The radical generation in the redox reaction of meso-2,3-dimercaptosuccinic acid and cerium(IV) sulfate in acid-aqueous medium is supposed to occur by one electron transfer from meso-2,3-dimercaptosuccinic acid to Ce(IV) according to the reactions given in Figure 1 as reported in the literature [18–22].

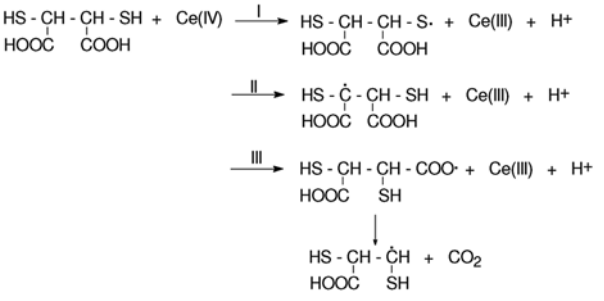

Figure 1. Radical formation reactions between meso-2,3-dimercaptosuccinic acid and Ce(IV) ions

Because of low S–H bonding energy, the formation of free radicals in reaction I in Figure 1 is more likely than other reactions to initiate crosslinking polymerization of acrylamide and N,N′methylene bis(acrylamide) and oxidative termination of polymer radicals is also possible by ceric ions [18, 20, 21]. In previous investigations, it is described that the formation of radicals on carboxyl groups may be possible [18–22]. However, the radical formation on carboxyl groups may appear less than that of the other radical formation reactions given in Figure 1, as the formation of free radicals on carcoxyl groups requires more energy.

After radical generation by redox reaction of meso-2,3-dimercaptosuccinic acid-Ce(IV) in acid-aqueous medium, the crosslinking polymerization of acrylamide-N,N′-methylene bis (acrylamide) was performed and the crosslinked copolymer having chemical formula given in Figure 2 was synthesized.

In order to characterize the crosslinking polymers, infrared measurements were carried out with ATI Unicam (Mattson 1000) FT-IR spectrometer and the spectra of crossliked polymers were determined by KBr disk method. For this purpose, pellets of about 300 mg KBr powder containing finely grained powder of crosslinked polymer sample (7–8 mg) were made. Figure 3 shows that the FT-IR spectra of crossliked polymers containing different crosslinker ratios (n_{AAm}/n_{MBAA} = 20 and 150), synthesized using DMSA-Ce(IV) redox system have been recorded by ATI Unicam (Mattson 1000) FT-IR spectrometer. As can be seen from Figure 3, the bands which can be assigned to the N–H stretching vibration in –NH-group of N,N′-methylene bis(acrylamide) or $–CONH_2$ groups of acrylamide in hydrogels appear at 3470 and 1670 cm^{-1}. The C–H stretching band is characterized by the peak at 2960 cm^{-1} due to symmetric or asymmetric stretching vibration of the CH_2 groups of acrylamide or N,N′-methylene bis(acrylamide).

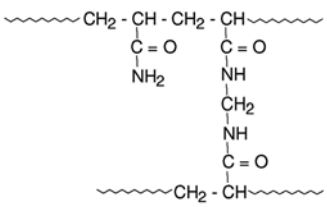

Figure 2. The chemical structure of the synthesized P(AAm-MBAA) hydrogel

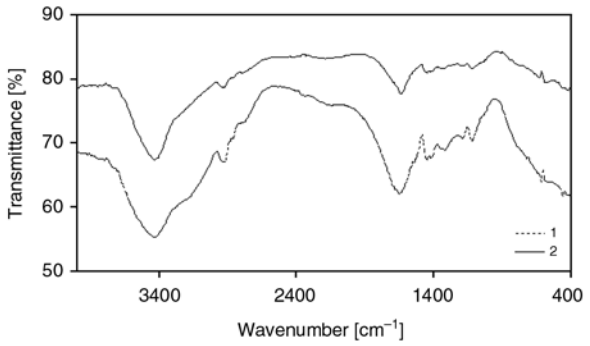

Figure 3. The FT-IR spectra of P(AAm-MBAA) hydrogels containing different n_{AAm}/n_{MBAA}, synthesized using meso-2,3-dimercaptosuccinic acid-Ce(IV) redox system. n_{AAm}/n_{MBAA} 20 (1) and 150 (2). C_{AAm} = 0.7 mol/l; $C_{H_2SO_4}$ = 0.0125 mol/l; $2n_{Ce(IV)} = n_{DMSA}$; T = 30°C.

3. Results and discussion

Swelling ratios (SR) and the values of equilibrium swelling ratios (ESR) of resulting hydrogels were calculated by using the Equations (1) and (2):

$$SR = \frac{m_t - m_0}{m_0} \quad (1)$$

$$ESR = \frac{m_{eq} - m_0}{m_0} \quad (2)$$

where SR represents the average swelling ratio of hydrogel in distilled water, obtained from triplicate experimental results. m_t and m_0 are the weights of hydrogel at time t and dried gel at initial time, respectively. ESR denotes the equilibrium swelling ratios in terms of g H_2O/g polymer and the m_{eq} is the weight of hydrogel at equilibrium.

The effects of the molar ratios of AAm/MBAA for different $n_{AAm}/n_{Ce(IV)}$ ($n_{AAm}/n_{Ce(IV)}$ = 100 and 200; $n_{DMSA} = 2n_{Ce(IV)}$) and acid concentrations ($C_{H_2SO_4}$ = 0.0125 and 0.0250 mol/l) on the swelling ratios of hydrogels in distilled water has been shown in Figures 4 and 5. The concentration of acrylamide monomer in these experiments was kept constant at 0.7 mol/l. As can be seen from Figures 4 and 5, it is observed that the increase in the molar ratio of AAm/MBAA for different acid concentrations of 0.0125 mol/l and 0.025 mol/l, and the $n_{AAm}/n_{Ce(IV)}$ values of 200 and 100 has increased the swelling ratios of hydrogels. The equilibrium swelling ratios determined from the curves of the swelling ratios of hydrogels depending on the n_{AAm}/n_{MBAA} for vari-

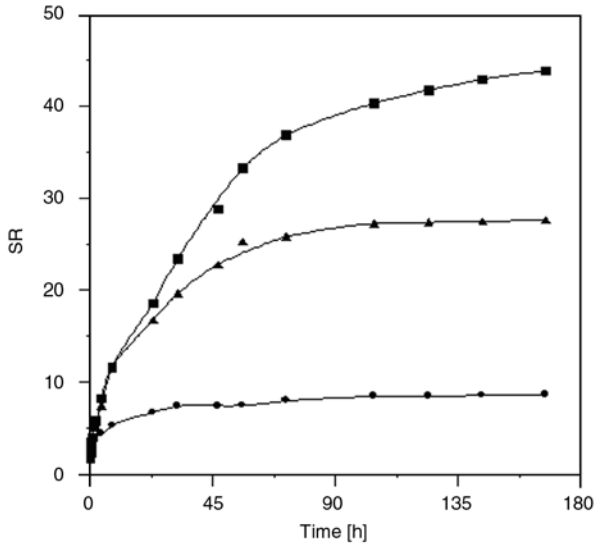

Figure 4. The dependence of swelling ratios of P(AAm-MBAA) hydrogels synthesized at the acid concentration of 0.025 mol/l and the $n_{AAm}/n_{Ce(IV)}$ of 100 on the molar ratios of AAm/MBAA. n_{AAm}/n_{MBAA} = 40 (●), 80 (▲) and 100 (■); C_{AAm} = 0.7 mol/l; $2n_{Ce(IV)} = n_{DMSA}$; T = 30°C

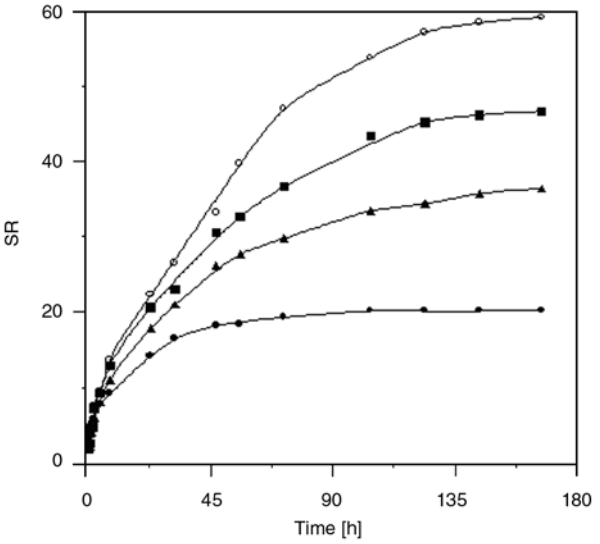

Figure 5. The effect of the molar ratios of AAm/MBAA on swelling ratios of P(AAm-MBAA) hydrogels synthesized at the acid concentration of 0.0125 mol/l and the $n_{AAm}/n_{Ce(IV)}$ of 200. n_{AAm}/n_{MBAA} = 20 (●), 60 (▲), 80 (■) and 150 (o); C_{AAm} = 0.7 mol/l; $2n_{Ce(IV)} = n_{DMSA}$; T = 30°C.

ous acid and initiator concentrations in crosslinking polymerization reaction have been listed in Table 1. As can be seen from the results given in Table 1, an increase in the n_{AAm}/n_{MBAA} values has resulted in an increase in the equilibrium swelling ratios of the synthesized hydrogels in distilled water. The photographic pictures of P(AAm-MBAA) hydrogels containing different crosslinker ratios are shown in Figure 6. The hydrogel represented with letter *A* is more opaque due to having higher crosslinker concentration (n_{AAm}/n_{MBAA} = 20), whereas, the hydrogel represented with letter *D* is more transparent due to having lower crosslinker concentration (n_{AAm}/n_{MBAA} = 150). These results show that hydrogels having less crosslink bonds swell better than hydrogels having more crosslink bonds as expected. In order to describe the phenomenon of swelling of more opaque hydrogels, phase separation is assumed in the systems and in the case of AAm-based hydrogels it is explained by entanglements between chains developing during polymerization in water medium as described in a previous study [27].

The dependence of swelling ratios of hydrogels on the acid concentration in crosslinking polymerization reaction at constant crosslinker molar ratio of n_{AAm}/n_{DMSA} = 40 is given in Figure 7. The augmentation in acid concentration has led to a decrease in the swelling ratios of hydrogels in distilled water. With increasing acid concentration in crosslinking polymerization, $-CONH_2$ groups of acrylamide may slowly undergo hydrolysis and the functional groups of –COOH may appear [28]. The functional groups $-CONH_2$ and –COOH in hydrogels react with each other to form the imide functional groups (–CONHOC–) in P(AAm-MBAA) hydrogels. For this reason, the hydrogel synthesized at higher acid

Table 1. The effect of the n_{AAm}/n_{MBAA} on the equilibrium swelling ratios of hydrogels synthesized at different acid and initiator concentrations. C_{AAm} = 0.7 mol/l; T = 30°C.

$n_{AAm}/n_{Ce(IV)}$	$C_{H_2SO_4}$ [mol/l]	n_{AAm}/n_{MBAA}	ESR (g H_2O/g polymer)
100	0.0250	40	8.59
100	0.0250	80	27.62
100	0.0250	100	43.91
200	0.0125	20	20.17
200	0.0125	60	36.41
200	0.0125	80	46.48
200	0.0125	150	57.18

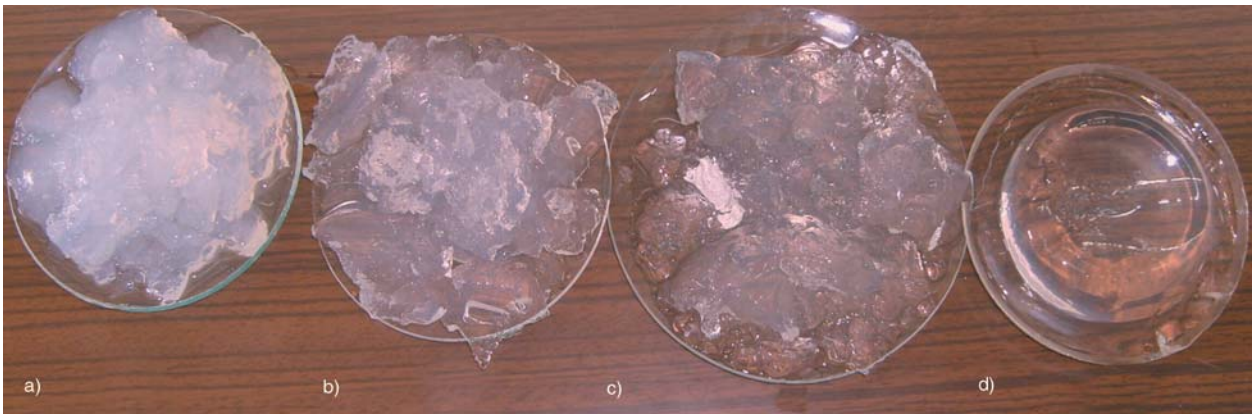

Figure 6. The photographic pictures of swelled hydrogels containing different molar ratios of AAm/MBAA. n_{AAm}/n_{MBAA} = 20 (a), 40 (b), 60 (c) and 150 (d). C_{AAm} = 0.7 mol/l; $C_{H_2SO_4}$ = 0.0125 mol/l; $n_{AAm}/n_{Ce(IV)}$ = 200; $2n_{Ce(IV)} = n_{DMSA}$; T = 30°C.

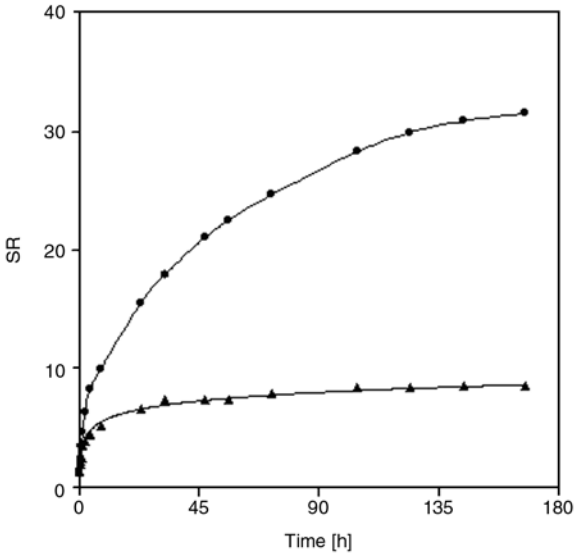

Figure 7. The swelling ratios of hydrogels synthesized at different acid concentrations. $C_{H_2SO_4}$ = 0.0125 (●) and 0.025 (▲) mol/l; C_{AAm} = 0.7 mol/l; n_{AAm}/n_{MBAA} = 40; $2n_{Ce(IV)} = n_{DMSA}$; T = 30°C.

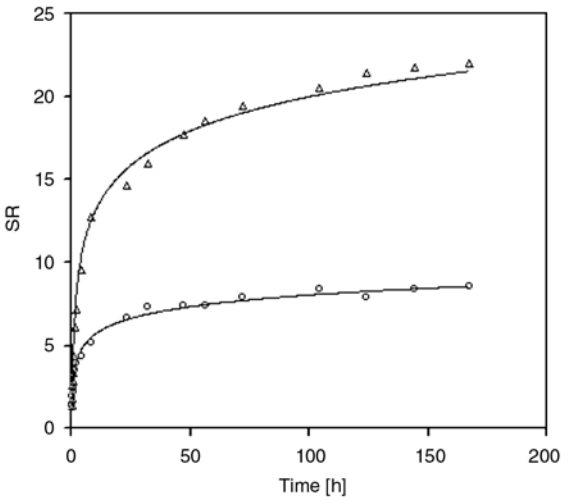

Figure 8. The relation between the molar ratios of AAm/Ce(IV) in crosslinking polymerization reaction and the swelling ratios of P(AAm-MBAA) hydrogels in distilled water, $n_{AAm}/n_{Ce(IV)}$ = 100 (o) and 200 (Δ). C_{AAm} = 0.7 mol/l; $C_{H_2SO_4}$ = 0.025 mol/l; n_{AAm}/n_{MBAA} = 40; $2n_{Ce(IV)} = n_{DMSA}$; T = 30°C.

concentration swells less than that synthesized at lower acid concentration. The values of equilibrium swelling ratios of hydrogels synthesized at different acid concentrations of 0.025 and 0.0125 mol/l have been determined as 8.59 and 31.53 g H_2O/g polymer for n_{AAm}/n_{MBA} = 40, respectively.

The effect of the molar ratios of AAm/Ce(IV) in crosslinking polymerization reaction at constant acid and crosslinker concentrations on the swelling ratios of P(AAm-MBAA) hydrogels in distilled water has been illustrated in Figure 8. The increase in the nAAm/nCe(IV) has resulted in an increase in the swelling ratios of hydrogels in distilled water. The equilibrium swelling ratios of hydrogels have been determined as 8.59 and 22.03 g H_2O/g polymer for the molar ratios of AAm/Ce(IV) of 100 and 200, respectively, in crosslinking polymerization reaction at constant acid concentration (0.025 mol/l) and crosslinker ratio (n_{AAm}/n_{MBA} = 40). It is evident that the increase in initiator concentration in synthesis of P(AAm-MBAA) hydrogel using cerium(IV) sulfate meso-2,3-dimercaptosuccinic acid redox system has decreased the swelling ratios of synthesized P(AAm-MBAA) hydrogels in distilled water.

The kinetic swelling results of hydrogels synthesized at various reaction parameters were examined by Peppas kinetic formula [29–31] (Equation (3)):

$$\frac{m_t}{m_{eq}} = kt^n \quad (3)$$

Linearized form of Equation (3) can be written as shown in Equation (4):

$$\ln\frac{m_t}{m_{eq}} = \ln k + n\ln t \quad (4)$$

where m_t and m_{eq} are the weights of hydrogels at time, t and at equilibrium respectively. k and n are constants. The values of exponent n are dependent on the amount of ionic groups in hydrogel. This equation is valid in the swelling ratio less than 60% [13, 31]. Using this criteria, the exponent, n and k values are obtained from the slope and intercept determined from a plot of $\ln(m_t/m_{eq})$ versus $\ln t$, respectively.

Figures 9 and 10 show a logarithmic plot ($\ln(m_t/m_{eq})$ versus to $\ln t$) of the swelling rate of P(AAm-MBAA) hydrogels with various crosslinker contents. The kinetic parameters (k and n values obtained from the slop and intercept of straight lines) in the swelling kinetic equation of P(AAm-MBAA) hydrogels synthesized at different acid, initiator and crosslinker concentrations have been summarized in Table 2. The experimental results show that an increasing crosslinker ratio (n_{AAm}/n_{MBAA}) results in significant rises in the n exponent, whereas the k value decreases. The effect of acid concentration of initiation system on the swelling behaviors has been examined (Figure 11). As can be seen from Figure 11 and Table 2 that at higher acid concentrations, the swelling of gels is slow, the corresponding k values increase by increasing acid concentrations, while the n values somewhat decrease.

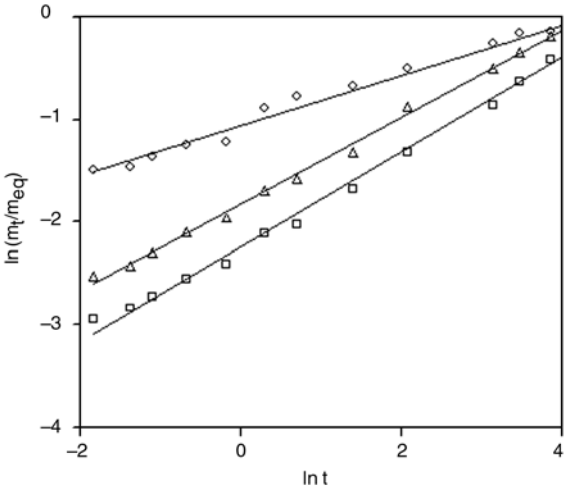

Figure 9. The effect of molar ratios of acrylamide to crosslinker on the swelling rates of P(AAm-MBAA) hydrogels in distilled water, synthesized at the acid concentration of 0.025 mol/l and the $n_{AAm}/n_{Ce(IV)}$ of 100. n_{AAm}/n_{MBAA} = 40 (o), 80 (Δ) and 100 (□).

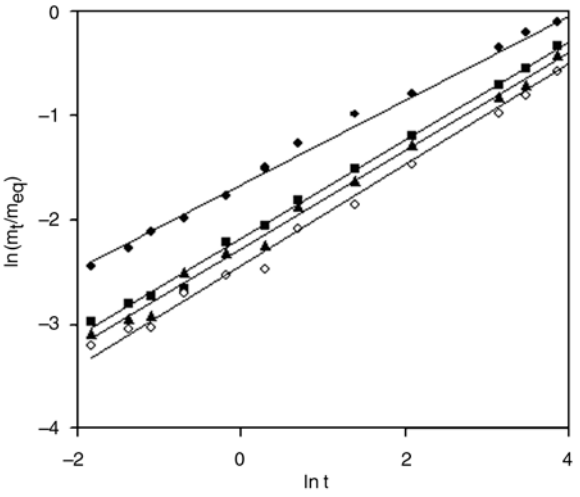

Figure 10. The dependence of the swelling rate of hydrogels synthesized at the acid concentration of 0.0125 mol/l and the $n_{AAm}/n_{Ce(IV)}$ of 200 on the n_{AAm}/n_{MBAA}. n_{AAm}/n_{MBAA} = 20 (●), 60 (■), 80 (▲) and 150 (o).

Table 2. The dependence of kinetic parameters in swelling kinetic equation fitting data obtained from swelling results of P(AAm-MBAA) hydrogels in distilled water on the acid concentration in crosslinking polymerization reaction. C_{AAm} = 0.7 mol/l; T=30°C.

$C_{H_2SO_4}$ [mol/l]	$n_{AAm}/n_{Ce(IV)}$	n_{AAm}/n_{MBAA}	n	k	Correlation coefficient, (R)
0.0125	200	20	0.405	0.191	0.995
0.0125	200	60	0.471	0.113	0.997
0.0125	200	80	0.472	0.103	0.996
0.0125	200	150	0.485	0.090	0.993
0.0125	100	40	0.457	0.119	0.990
0.0250	100	40	0.244	0.348	0.983
0.0250	100	80	0.421	0.161	0.997
0.0250	100	100	0.462	0.107	0.994
0.0250	200	40	0.371	0.210	0.967

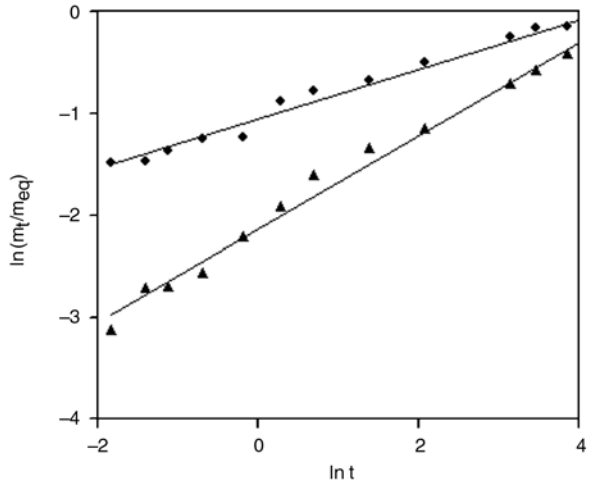

Figure 11. The relation between acid concentrations in crosslinking polymerization reactions at constant crosslinker concentration (n_{AAm}/n_{MBAA} = 40) and the swelling rate of synthesized P(AAm-MBAA) hydrogels in distilled water. $C_{H_2SO_4}$ = 0.0125 (▲) and 0.0250 (●) mol/l.

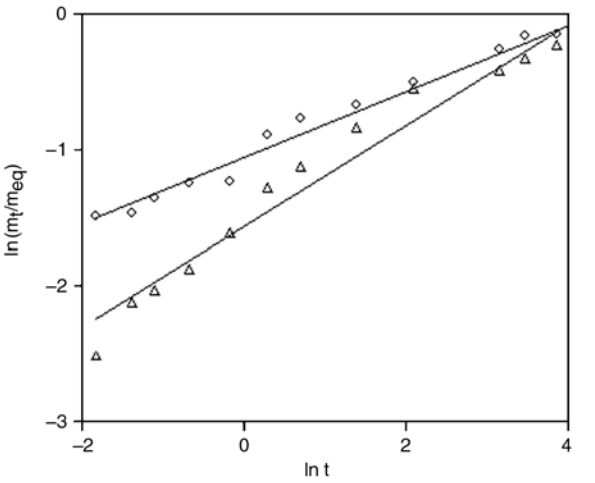

Figure 12. The dependence of swelling kinetic rate of synthesized P(AAm-MBAA) hydrogels in distilled water on molar ratios of AAm/Ce(IV) in crosslinking polymerization reaction. $n_{AAm}/n_{Ce(IV)}$ = 100 (o) and 200 (Δ).

The swelling rate of P(AAm-MBAA) hydrogels synthesized at different initiator concentrations ($n_{AAm}/n_{Ce(IV)}$ = 100 and 200) has been shown in Figure 12. The augmentation in the molar ratio of AAm/Ce(IV) in crosslinking polymerization reaction shows an increase in the n exponent from 0.244 to 0.371. However, the k value decreases from 0.348 to 0.210 (Table 2). This result indicates that the increase in initiator concentration in crosslinking polymerization reaction of P(AAm-MBAA) hydrogels synthesized using DMSA-Ce(IV) redox system in acid aqueous medium has led to a decrease in the swelling rate.

4. Conclusions

Ceric salt-organic reducing agent containing thiol functional groups are promising a new alternative initiator system for crosslinking polymerization of AAm with MBAA in acid-aqueous medium at ambient temperatures. The dependence of swelling ratio and swelling rate of hydrogels on the parameters such as the n_{AAm}/n_{MBAA}, acid concentration and the $n_{AAm}/n_{Ce(IV)}$ in the crosslinking polymerization reaction of acrylamide and N,N′-methylene bis(acrylamide) initiated with meso-2,3-dimercaptosuccinic acid-cerium(IV) sulfate redox system has been investigated. It has been observed that the augmentation in the acid, initiator and crosslinker concentrations has led to a decrease in the swelling ratio and rate of P(AAm-MBAA) hydrogels in distilled water. The k and n exponent values in the kinetic equation have been calculated. The swelling ratios and k values decrease with increasing Ce(IV) concentration ($2n_{Ce(IV)} = n_{DMSA}$) due to increase in the concentration of meso-2,3-dimercaptosuccinic acid. This phenomenon is attributed that thiol group in meso-2,3-dimercaptosuccinic acid acts as a crosslinking agent. Therefore the swelling equilibrium ratio and swelling rate decrease with increase in its concentration.

Acknowledgements

The present work was supported by the Research Fund of University of Istanbul. Project numbers: UDP-2329/10042008.

References

[1] Naghash H. J., Massah A., Erfan A.: Free-radical crosslinking polymerization of acrylamide and N,N′-methylenebis acrylamide by used Ce(IV)/polyethylene glycol and Ce(IV)/diethylmalonate redox initiator systems. European Polymer Journal, **38**, 147–150 (2002).
DOI: 10.1016/S0014-3057(01)00171-9

[2] Miyata T., Asami N., Okawa K., Uragami T.: Rapid response of a poly(acrylamide) hydrogel having a semi-interpenetrating polymer network structure. Polymer Advanced Technology, **17**, 794–797 (2006).
DOI: 10.1002/pat.818

[3] Tanaka T.: Collapse of gels and the critical endpoint. Physical Review Letters, **40**, 820–823 (1978). DOI: 10.1103/PhysRevLett.40.820

[4] Hoffman A. S.: Applications of thermally reversible polymers and hydrogels in therapeutics and diagnostics. Journal of Controlled Release, **6**, 297–305 (1987). DOI: 10.1016/0168-3659(87)90083-6

[5] Okano T.: Molecular design of temperature-responsive polymers as intelligent materials. Advances in Polymer Science, **110**, 179–197 (1993). DOI: 10.1007/BFb0021133

[6] Tanaka T., Nishio I., Sun S-T., Ueno-Nishio S.: Collapse of gels in an electric field. Science, **218**, 467–469 (1982). DOI: 10.1126/science.218.4571.467

[7] Kataoka K., Miyazaki H., Bunya M., Okano T., Sakurai Y.: Totally synthetic polymer gels responding to external glucose concentration: Their preparation and application to on-off regulation of insulin release. Journal of the American Chemical Society, **120**, 12694–12695 (1998). DOI: 10.1021/ja982975d

[8] Miyata T., Asami N., Uragami T.: Preparation of an antigen-sensitive hydrogel using antigen-antibody bindings. Macromolecules, **32**, 2082–2084 (1999). DOI: 10.1021/ma981659g

[9] Tanaka T., Filmore D. J.: Kinetics of swelling of gels. Journal of Chemical Physics, **70**, 1214–1218 (1979). DOI: 10.1063/1.437602

[10] Tang Q., Wu J., Lin J., Li Q., Fan S.: Two-step synthesis of polyacrylamide/polyacrylate interpenetrating network hydrogels and its swelling/deswelling properties. Journal of Materials Science, **43**, 5884–5890 (2008). DOI: 10.1007/s10853-008-2857-x

[11] Tang Q., Lin J., Wu J.: The preparation and electrical conductivity of polyacrylamide/graphite conducting hydrogel. Journal of Applied Polymer Science, **108**, 1490–1495 (2008). DOI: 10.1002/app.27716

[12] Wu J., Lin J., Zhou M., Wei M.: Synthesis and properties of starch-graft-acrylamide/clay superabsorbent composite. Macromolecular Rapid Communications, **21**, 1032–1034 (2000). DOI: 10.1002/1521-3927(20001001)21:15<1032::AID-MARC1032>3.0.CO;2-N

[13] Oh K. S., Bae Y. C.: Swelling behaviour of submicron gel particles. Journal of Applied Polymer Science, **69**, 109–114 (1998). DOI: 10.1002/(SICI)1097-4628(19980705)69:1<109::AID-APP12>3.0.CO;2-V

[14] Tanaka T., Sato E., Hirokawa Y., Hirotsu S., Peetermans J.: Critical kinetics of volume phase transition of gels. Physical Review Letters, **55**, 2455–2458 (1985). DOI: 10.1103/PhysRevLett.55.2455

[15] Yildiz B., Işik B., Kiş M.: Synthesis and characterization of thermoresponsive isopropylacrylamide-acrylamide hydrogels. European Polymer Journal, **38**, 1343–1347 (2002). DOI: 10.1016/S0014-3057(01)00308-1

[16] Emik S., Gürdag G.: Synthesis and swelling behavior of thermosensitive poly(N-isopropyl acrylamide-co-sodium-2-acrylamido-2-methyl propane sulfonate) and poly(N-isopropyl acrylamide-co-sodium-2-acrylamido-2-methyl propane sulfonate-co-glycidyl methacrylate) hydrogels. Journal of Applied Polymer Science, **100**, 428–438 (2006). DOI: 10.1002/app.23126

[17] Sayil Ç., Okay O.: Swelling-shringing hysteresis of poly(N-isopropyl acrylamide) gels in sodium dodecylbenzenesulfonate solution. Journal of Applied Polymer Science, **83**, 1228–1232 (2002). DOI: 10.1002/app.2289

[18] Özeroglu C., Erdogan S.: Oxidative polymerization of acrylamide in the presence of thioglycolic acid. Central European Journal of Chemistry, **3**, 705–720 (2005). DOI: 10.2478/BF02475198

[19] Misra G. S., Bajpai U. D. N.: Redox polymerization. Progress in Polymer Science, **8**, 61–131 (1982). DOI: 10.1016/0079-6700(82)90008-9

[20] Özeroglu C., Özduganci C.: Low temperature initiation by 3-mercaptopropionic acid-Ce(IV) or -$KMnO_4$ redox system for polymerization of acrylamide monomer. Polymer-plastics Technology and Engineering, **45**, 549–554 (2006). DOI: 10.1080/03602550600554109

[21] Özeroglu C., Sezgin S.: Polymerization of acrylamide initiated with Ce(IV)- and $KMnO_4$-mercaptosuccinic acid redox systems in acid-aqueous medium. Express Polymer Letters, **1**, 132–141 (2007). DOI: 10.3144/expresspolymlett.2007.22

[22] Saraç A. S.: Redox polymerization. Progress in Polymer Science, **24**, 1149–1204 (1999). DOI: 10.1016/S0079-6700(99)00026-X

[23] Pandey P. K., Srivastava A., Tripathy J., Behari K.: Graft copolymerization of acrylic acid onto guar gum initiated by vanadium (V)-mercaptosuccinic acid redox pair. Carbonhydrate Polymer, **65**, 414–420 (2006). DOI: 10.1016/j.carbpol.2006.01.022

[24] Singh B., Chauhan G. S., Kumar S., Chauhan N.: Synthesis, characterization and swelling responses of pH sensitive psyllium and polyacrylamide based hydrogels for the use in drug delivery (I). Carbonhydrate Polymer, **67**, 190–200 (2007). DOI: 10.1016/j.carbpol.2006.05.006

[25] Soppimath K. S., Kulkarni A. R., Aminabhavi T. M.: Chemically modified polyacrylamide-*g*-guar gum-based crosslinked anionic microgels as pH-sensitive drug delivery systems: Preparation and characterization. Journal of Control Release, **75**, 331–345 (2001). DOI: 10.1016/S0168-3659(01)00404-7

[26] Kaith B. S., Kumar K.: Selective absorption of water from different oil-water emulsions with Psy-cl-poly(AAm) synthesized using irradiation copolymerization method. Bulletin of Materials Science, **30**, 387–391 (2007).
DOI: 10.1007/s12034-007-0062-1

[27] Kuru E. A., Orakdogen N., Okay O.: Preparation of homogeneous polyacrylamide hydrogels by free radical crosslinking polymerization. European Polymer Journal, **43**, 2913–2921 (2007).
DOI: 10.1016/j.eurpolymj.2007.04.019

[28] Schildknecht C. E.: Vinyl and related polymers. John Wiley and Sons, New York (1952).

[29] Franson N. M., Peppas N. A.: Influence of polymer composition on non-fickian water transport through glassy copolymer. Journal of Applied Polymer Science, **28**, 1299–1310 (1983).
DOI: 10.1002/app.1983.070280404

[30] Ritger P. L., Peppas N. A.: A simple equation for description of solute release II. Fickian and anomalous release from swellable devices. Journal Control Release, **5**, 37–42 (1987).
DOI: 10.1016/0168-3659(87)90035-6

[31] Biçak N., Şenkal B. F., Şişmanoglu T., Özeroglu C.: New, strong cationic hydrogels: Preparation of *N,N,N′,N′*-tetraallyl piperazinium dibromide and its copolymers with N,N-diallyl morpholinium bromide. Journal of Polymer Science Part A: Polymer Chemistry, **38**, 1006–1013 (2000).
DOI: 10.1002/(SICI)1099-0518(20000315)38:6<1006::AID-POLA10>3.0.CO;2-F

eXPRESS Polymer Letters Vol.3, No.3 (2009) 177–189
Available online at www.expresspolymlett.com
DOI: 10.3144/expresspolymlett.2009.23

Mechanical properties of ceramic-polymer nanocomposites

R. Abraham[1,6], S. P. Thomas[2], S. Kuryan[3], J. Isac[4], K. T. Varughese[5], S. Thomas[6]*

[1]St Dominics College, Kanjirapally, Kottayam, Kerala-686512, India
[2]Corporate R&D Division, HLL Lifecare Limited, Trivandrum, Kerala-695012, India
[3]St Stephen's College, Kollam, Kerala, India
[4]CMS College, Kottayam , Kerala, India
[5]Central Power Research Institute, Bangalore, India
[6]School of Chemical Sciences, Mahatma Gandhi University, Kottayam, Kerala-686560, India

Received 25 November 2008; accepted in revised form 16 February 2009

Abstract. Nano crystalline powders of Barium Sodium Niobate (BNN) with the composition Ba_{3-2x} Na_{4+x} R Nb_{10} O_{30} with (R stands for rare earth = 0, $x = 0$) have been prepared by conventional ceramic technique. Barium Sodium Niobate can form a wide range of solid solutions, incorporating rare earth and alkali, alkaline earth elements with different compositions. The powder belonged to tungsten bronze type structure with tetragonal symmetry and lattice constants $a = b = 1.2421$ nm and $c = 0.3903$ nm. XRD (X-ray Diffraction) SEM (Scanning Electron Microscope) and AFM (Atomic Force Microscope) studies revealed that the particle size is in the nanometer range. Composites are prepared by mixing powders of BNN with polystyrene at different volume fractions of the BNN. Melt mixing technique is carried out in a Brabender Plasticoder at a rotor speed of 60 rpm (rotations per minute) for composite preparation. Mechanical properties such as stress-strain behavior, Young's modulus, tensile strength, strain at break etc. are evaluated. Addition of filler enhances the mechanical properties of the polymer such as Young's modulus and tensile strength. The composites showed the trend of perfect adhesion between the filler and the polymer. The filler particles are distributed relatively uniform fashion in all composites and the particles are almost spherical in shape with irregular boundaries. To explore more carefully the degree of interfacial adhesion between the two phases, the results are analyzed by using models featuring adhesion parameter. The experimental results are compared with theoretical predictions.

Keywords: *nanocomposites, modeling, mechanical properties, adhesion, polystyrene*

1. Introduction

Materials consisting of more than one kind of substance, that is, composite materials have been designed for complying with various demands. Plastics and rubbers incorporating powdery fillers have frequently been used from the viewpoint of mechanical properties [1]. For these particulate composite materials, it is important to clarify the reinforcement effect of fillers. A variety of theoretical and experimental studies have been reported on the reinforcement effect in terms of macroscopic mechanical properties. However there are a lot of difficulties because of the uncertainty in adhesion between matrix and fillers, dispersion behavior of filler in matrix etc. [2].

In recent years, new approaches are successfully developed for the preparation of polymer composites for electronic applications. Development of electronic devices working at high operating frequencies, such as fast computers, cellular phones, etc. require a new high-dielectric constant materials that combine good dielectric properties with both mechanical strength and ease of processing. The unique combination of dielectric and mechanical

*Corresponding author, e-mail: sabut552001@yahoo.com

properties is hard to achieve in a one-component material. Pure polymers are easy to process into mechanically robust components but generally suffer from low dielectric constant [3, 4]. On the other hand, typical high-dielectric constant materials, such as ferroelectric ceramics, are brittle and require high-temperature processing [5] which are often not compatible with current circuit integration technologies. The ideal solution would be high-K materials that are mechanically robust and process able at ambient temperatures have to be incorporated with suitable polymers such as ferroelectric ceramic-polymer composites that may combine desired properties of the components [6, 7].

An important attribute of polymers is the ability to modify their inherent physical properties by the addition of fillers while retaining their characteristics. Polymers can be made stronger, stiffer, and electronically conductive by the incorporation of various additives. Most of these modifications are made by the addition of inorganic fillers to the polymer. These fillers, present in varying degrees, also affect the basic mechanical properties of the polymer [8–12].

In the present work we have synthesized a new class of ferroelectric ceramic material barium sodium niobate [13–15] and prepared composites out of it by mixing it with polystyrene. In this paper, we report a study on the mechanical properties of polystyrene/barium sodium niobate composites. Tensile modulus, tensile strength and elongation at break data have been analyzed as a function of BNN filler loading on the basis of theoretical predictions for two phase systems. X-ray Diffraction (XRD), Scanning Electron Microscopy (SEM) and Atomic Force Microscope (AFM) studies have been made to characterize the structure and properties of the filler and the composites.

2. Experimental

2.1. Materials

The filler, ferroelectric ceramic material (Barium Sodium Niobate, BNN) was prepared by usual ceramic technique using reagent grade sodium carbonate, barium carbonate, and niobium pentoxide. Solid-state reaction technique was adopted for the preparation of the material. The starting materials were $BaCO_3$ (Merck Ltd., Mumbai, India), Na_2CO_3 and Nb_2O_5 (CDH, New Delhi, India). The specific properties of the Polystyrene (Merck Ltd., Mumbai, India) are reported in Table 1.

Table 1. Properties of polystyrene

Properties	Value
Dielectric constant	2.5–2.65
Poisson's ratio	0.333
Water absorption	0.05%
Glass transition temp	108°C
Average molecular wt.	208 000

The constituent carbonates and oxides were weighed according to the chemical formulae satisfying the stoichiometric relations Equation (1):

$$3BaCO_3 + 2Na_2CO_3 + 5Nb_2O_5 \rightarrow \rightarrow Ba_3Na_4Nb_{10}O_30 + 5CO_2 \quad (1)$$

The powders were mixed, milled and calcined at a temperature of 1000°C for three hours. For the preparation of one gram of $Ba_3Na_4Nb_{10}O_{30}$, 0.30948 g of $BaCO_3$, 0.11081 g of Na_2CO_3, and 0.69424 g of Nb_2O_5 were used. To break the agglomerates, which get formed during the calcinations stage, the powder calcined was once again crushed and ground finely. Appropriate quantity of polyvinyl alcohol (binder) was used for proper mixing. Disc shaped pellets (of diameter 10 mm and thickness 2.5 to 3 mm) were prepared at an optimum load of 80 kN and for sintering; the pressed pellets were placed over alumina plate dispersed with zirconium powder. Sintering was carried out at a temperature of 1200°C for 5 hrs. A heating rate of 10°C/min was allotted before the dwell temperature of 600°C and of 50°C/min after the same. The density of the sintered samples was calculated by both sample geometry and Archimedes methods [16]. Then these sintered samples were named as (Barium Sodium Niobate ($Ba_3Na_4Nb_{10}O_{30}$) or (BNN)). The weight % of the constituent carbonates and oxides were calculated using Equation (1) and presented in Table 2.

Table 2. Composition of BNN

Material	Content [wt%]
$BaCO_3$	27.75
Na_2CO_3	9.93
Nb_2O_5	62.31

2.1.1. Methods of composite preparation

The melt mixing technique was chosen for preparing the composites because it allowed solvent free mixing for the ceramic filler. By melting at high temperature, molten polystyrene can easily penetrate between filler particles, which facilitates suitable mixing and allow avoiding air trapping into the composites. Consequently void free composites were obtained [17].

Polystyrene-Ceramic composites were prepared in a Brabender Plasticoder. The cavity for mixing in the instrument has an internal volume of $40 \cdot 10^{-6}$ m^3 and is fitted with two screw type rotors of variable speed. Filling the internal cavity completely with mixing charges ensures a constant ram pressure and good mixing. The rotor and the cavity were heated with a circulated flow of electric current and the temperature could be set at any desired level. When the temperature of the internal mixer was raised to 180°C, polystyrene was added and complete melting of polymer was ensured by a constant minimum torque and attainment of the desired cavity temperature of 180°C. BNN powder then added to molten PS and was mixed for about 6 minutes at a rotor speed of 60 rpm. The compositions of the composites were 10, 20, 30 and 40% by the volume of the filler. The mixed samples were compression molded into sheets of desired thickness by hydraulic press at a temperature of 180°C and were used for different studies. The composites were named as BNN10, BNN20, BNN30 and BNN40.

2.1.2. Measurements

Energy dispersive X-ray spectrograph was taken by ISIS Link Oxford Instrument, UK. Powder X-ray diffraction data were taken with Bruker X-ray diffractometer using Cu-K_α line (0.154 nm) (D8 Advance). The morphology and microstructure of the composites were analyzed by means of high resolution scanning electron microscopy using a JEOL JSM 840-microscope.

Tapping mode Atomic force microscope measurements were carried out in air at ambient conditions (28°C) with a Veeco Nanoscope 3D, made by Digital Instruments Inc., USA. The characteristics of the measurements are scan rate, scan size and data points. The selected scan rate was 1.001 Hz, scan size 1 μm and the image contained 512 data points. Images were analyzed using a Nanoscope image processing software. Particle size is calculated by the particle analysis software 'Nanoscope V531r1. Rectangular samples of 10×1.2×0.2 cm^3 were cut for tensile testing. Tensile testing was done using a Universal Testing Machine (Shimadzu, model AG-50kN) at a cross head speed of 10 mm/min. Tensile properties were determined according to ASTM D638.

3. Results and discussion

3.1. Morphological study

3.1.1. EDX spectrum

The EDX spectrum of BNN Figure 1 gives the information on the elemental composition of the material [18]. The % of carbonates and oxides used for the preparation of BNN is reported in Table 2. The three dominant peak positions at 1, 2.3 and 4.6 keV correspond quite well to the energy pattern of the corresponding materials (Na, Nb and Ba) reported in the EDX international chart, giving the evidence that Niobium is dominant in BNN samples. Figure 1 and Table 2 are neatly coincided.

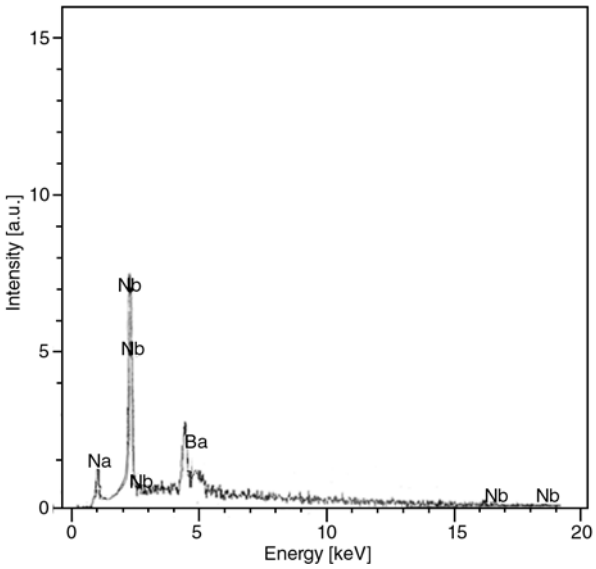

Figure 1. EDX spectrum of BNN

3.1.2. X-ray analysis of BNN

Fine powders of BNN were obtained by crushing the sintered pellets. Powder X-ray diffraction pattern of the crushed pellets were recorded in 2θ range of 10 to 90° as in Figure 2. Each crystalline solid has its own characteristic X-ray powder pattern, which may be used as a 'fingerprint' for its identification. The lattice parameters of the com-

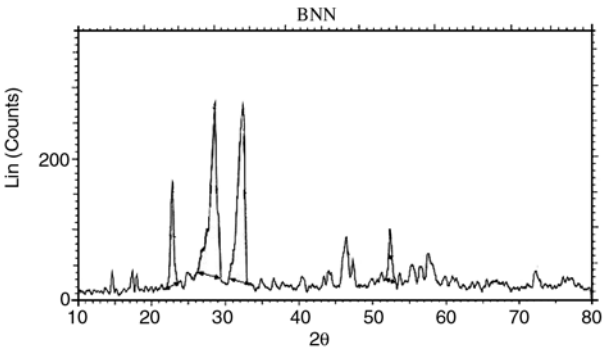

Figure 2. XRD of BNN

pound were obtained using the computer file PDF match to JCPDS data attached to the system analyzer. The patterns were indexed and identified using the JCPDS-ICDD database (Joint Committee on Powder diffraction Standards-International centre for Diffraction Standards-1994). The crystalline phases obtained were structures with tetragonal symmetry. The basic relation for indexing structures with tetragonal symmetry is given by Equation (2):

$$\frac{1}{d_{hkl}^2}=\frac{h^2}{a^2}+\frac{k^2}{b^2}+\frac{l^2}{c^2} \tag{2}$$

The *d*-spacing of a set of planes is defined as the perpendicular distance between any pair of adjacent planes in the set and it is this *d* value that appears in Bragg's law. The *d*-spacing of the lines in a powder pattern are governed by the values of unit cell parameters (*a*, *b*, *c*), provided the various lines have been assigned by Miller indices [*h k l*]. The results are again calculated by the computer program PDP1.1 (Powder diffraction Profile 1.1) [19].

All the characteristic peaks of BNN are reported in Table 3. The second and third columns of Table 3 give the intensity count [%] and intensity [%] of the diffraction lines. The observed *d* value from XRD data and calculated *d* value using the computer program P.D.P 1.1 are reported in the fourth and the fifth column of the Table 3. The difference between the observed and calculated *d* value for each reflection is given in the sixth column of the table. From the examination of Δd values, it is evident that the observed and calculated values are nearly equal for all major peaks and hence the observed lattice parameters fit the experimental data. So the *d* value corresponds to the 2θ value of 22.767°, the [*h k l]* indices are [0 0 1], directly gives the value of *c*-parameter, which is 0.3903 nm for BNN crystals. The [0 0 2] reflection corresponding to *d* value of 0.1955 nm and the Δd value 0.0003. The presence of the above two reflections of the material in the XRD pattern confirm that BNN belong to tungsten bronze phase with tetragonal symmetry ($a = b \neq c$). For BNN the lattice parameters of the unit cell axis are $a = 1.2421$ nm and $c = 0.3903$ nm. The axial ratio $(\sqrt{10}(c/a))$ is nearly equal to unity, and volume of the unit cell $602.16 \cdot 10^{-30}$ m^3 which is the characteristics of tungsten bronze type structure with tetragonal symmetry. The space group of the above compound is found to be P4mm. The 32-point groups of crystals can be further classified into (*a*) crystals having a center of symmetry (*b*) crystals, which do not posses a centre of symmetry. Crystals with centre of symmetry include 11-point groups and that do not show any polarity. The crystals belong to the remaining 21-point groups do not have a centre of symmetry and posses one or more crystallographically unique directional axes. All crystals in the class of non-centro symmetric point groups show piezoelectric effect. In this group, which shows piezoelectric effect, ten point groups (including 1, 2, m, mm2, 4, 4mm, 3, 3m, 6 and

Table 3. XRD data of BNN

Angle (2θ)	Intensity count [%]	Intensity [%]	d value (obs) [nm]	d (cal) [nm]	Δd	[h k l]	FWHM (β°)	Particle size [nm]
22.767	16.00	57.8	0.3903	0.3903	0.00	[0 0 1]	0.467	41.41
29.298	27.5	99.1	0.3046	0.3048	–0.0002	[4 1 0]	0.469	39.71
32.372	27.7	100.0	0.2763	0.2768	0.0005	[3 1 1]	0.503	37.72
46.413	8.94	32.2	0.1955	0.1952	–0.0003	[0 0 2]		
47.330	5.28	19.0	0.1919	0.1927	0.0008	[1 0 2]		
52.378	9.18	33.1	0.1745	0.1737	–0.0008	[5 4 1]	0.506	49.53
55.358	4.81	17.3	0.1658	0.1638	–0.002	[4 1 2]		
56.456	4.7	16.9	0.1628	0.1624	–0.0004	[3 3 2]		
57.565	6.57	23.7	0.1600	0.1601	0.0001	[7 1 1]		
72.318	4.29	15.5	0.1306	0.1306	0.0000	[7 1 2]		

6mm) have only one unique direction axis. Such crystals are polar crystals and they show spontaneous polarization and ferroelectric effect [20].

The particle size is calculated from X-ray diffraction profiles of strong reflections with intensity % greater than 30 using Scherrer's equation by measuring the full width at half maximum (FWHM). The (FWHM) of the material is reported in the eighth column of Table 3 and the calculated particle size is in the last column of Table 3. The Debye Scherrer equation (3) for calculating the particle size is given by Equation (3) [21]:

$$L = \left(\frac{0.9\lambda}{\beta \cos\theta} \right) \tag{3}$$

where λ is the wavelength of light used for the diffraction, (Cu-K_α line) (0.154 nm) and β is the 'full width at half maximum' of the sharp peaks, and θ is the angle measured from the data chart. The calculated values of lattice parameters for BNN, which are in close agreement with values reported in the literature [22]. X-ray powder diffraction may be used to measure the average crystal size in a powdered sample, provided the average diameter is less than about 200 nm. The lines in the powder diffraction are of finite breadth but if the particles are very small the lines are broader than usual. The broadening increases with decreasing particle size. The limit is reached with particle diameters in the range roughly 2 to 10 nm; then the lines are so broad that they effectively 'disappear' into the background radiation.

The results reveal that the particle size of BNN is less than 100 nm. Since XRD is a first hand measuring technique for particle size calculations, one can prefer measurement using SEM or AFM for particle characterization.

3.1.3. X-ray analysis of the composites

The particle size of the ceramic powder and various composites are calculated from X-ray line broadening studies using Scherrer's equation. Figure 3 is the XRD pattern of PS. The particle sizes in all compositions are observed as almost same and reveal the powder is well dispersed in PS medium. Diffraction data is collectively given in Figure 4. All the peaks of the composites are identified and the [*h k l*] values are indexed. Humps seen in the

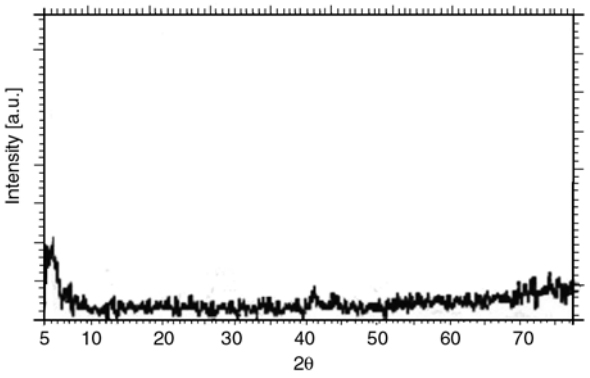

Figure 3. X-ray Diffraction pattern of Polystyrene

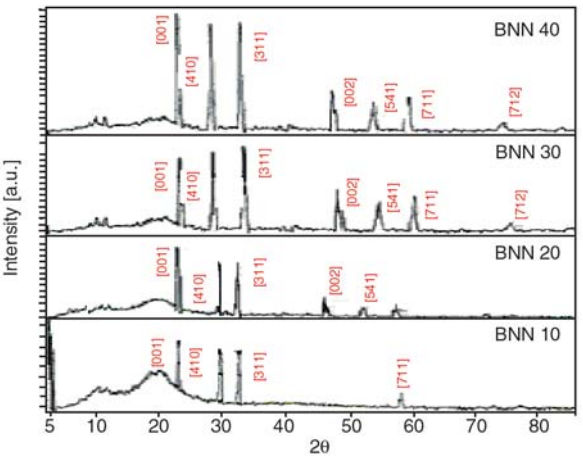

Figure 4. X-ray Diffraction pattern of Composites

left side in the diffractogram Figure 4 up to a 2θ of 20° characterize the amorphous nature of PS and they gradually diminish with the increment of filler content. The emergence of characteristic diffraction lines and their gradual sharpening increases with filler content and for BNN40 all most all the characteristic peaks of BNN are present. Strong and sharp three peaks of intensity 57% at 22.767° whose [*h k l*] values [0 0 1] of intensity 99.1% at 29.298° whose [*h k l*] values at [4 1 0] and of intensity 100% at 32.372° whose [*h k l*] values at [3 1 1] of BNN are seen clearly in all BNN-PS composites. Composites also showed an XRD pattern in which the basic peaks of BNN are intact in the composite, (the peak position didn't change and the particle size remains the same as the parent material) indicating that the parent material does not undergo any transformation during the preparation of the composite. Thus the comparison of XRD patterns of PS and the composites confirmed that BNN does not react with PS. The lattice parameters of the constituent phases are almost the same in all composites. This indicates that the structure remains the

same even if the composition of composites is varied. No other additional peak is observed apart from the parent material. All the above evidences confirmed the successful preparation of the two phase composite material This sequence is generally consistent with the study of Panajkar *et al*. [23] and the recent work of Lee *et al.* [24] who detected the unchangability of XRD peaks of the fillers by composite formation. Intensities of X-ray reflections are important for two main reasons. First, quantitative measurement of intensity is necessary in order to determine unknown crystal structures. Second, qualitative intensity data are needed to characterize materials and identify unknowns. The relative measure of the crystalline phases of the BNN composites can be obtained from the intensity of the scattered beam. From the Figure 4 it is concluded that with respect to the increment of filler content the magnitude of intensity increases and that reveal the increment of crystalline particles in the composites.

3.1.4. AFM images of the composites

AFM topographic images of the surfaces and cross sections of the composites are used for this study. In Figure 5a, 5b) the cross sectional images of selected composites are given. Images show some coloured areas in the images. These are areas where

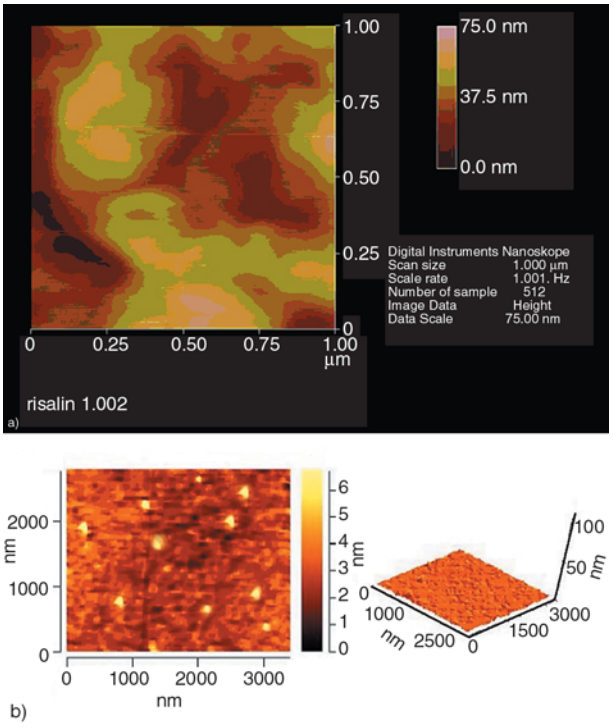

Figure 5. AFM image of BNN10 (a) and BNN40 (b)

Table 4. Particle size measurement through software

Dimension	Mean	Minimum
Height	2.58 nm	–0.91 nm
Area	10 059 nm^2	15.259 nm^2
Diameter	58.14 nm	4.40 nm
Length	119.38 nm	5.52 nm
Width	38.29 nm	5.52 nm

the particles are located in the PS matrix. While increasing the filler amount the number of such spots increases indicating the dispersion of the fillers in the matrix. By the AFM image Figure 5a we get a particle size of the order of 75 nm (rose coloured) for BNN from the image of the filled samples. The average particle size calculated by the software (Nanoscope particle analyzer V531r1) is reported in Table 4 and its value is 58 nm.

3.1.5. SEM Analysis

Morphology has been analyzed from Scanning Electron Microscope. The average particle diameter is found to be less than 100 nm in all composites. Three pairs of images of BNN10 and BNN40 with different magnification are given in Figure 6a and 6b, Figure 7a and 7b), and Figure 8a and 8b. The ceramic particles appear to be well dispersed in both low and high concentration composites. Clustering or agglomeration is seen to be absent in all BNN-PS composites. The filler particles are distributed relatively uniform fashion and the particles are almost spherical in shape with irregular boundaries. The filler particles are seen to be clearly embedded in the polymer matrix, which establishes the (0-3) connectivity of the composites. The ceramic-polymer composites are made up of an active ceramic phase embedded in a passive polymer phase. The properties of the composite depend on the connectivity of the phases, volume percent of ceramic, and the spatial distribution of the active phase in passive phase. The concept of connectivity developed by Newnham [25] describes the arrangement of the component phases within a composite. It is critical in determining the electromechanical properties of the composite. There are 10 different types of connectivities possible in a diphasic composite. It is shown in the form (*A*-*B*) where *A* refers to the number of directions in which the active phase is self connected or continuous. *B* shows the continuity directions of the passive phase. In BNN-

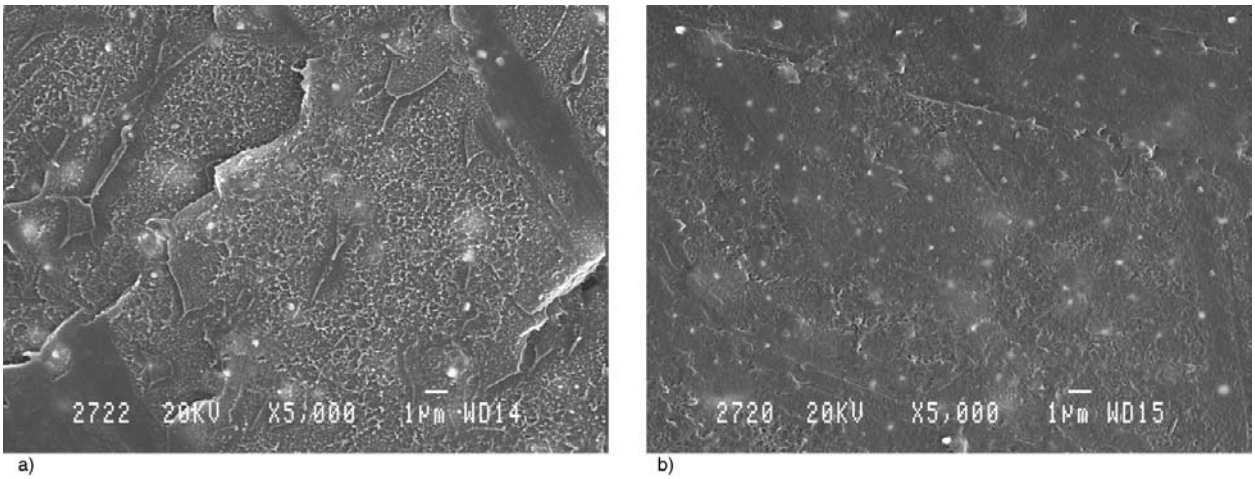

Figure 6. Fracture surface image of BNN10 (a) and BNN40 (b)(magnification (5 000))

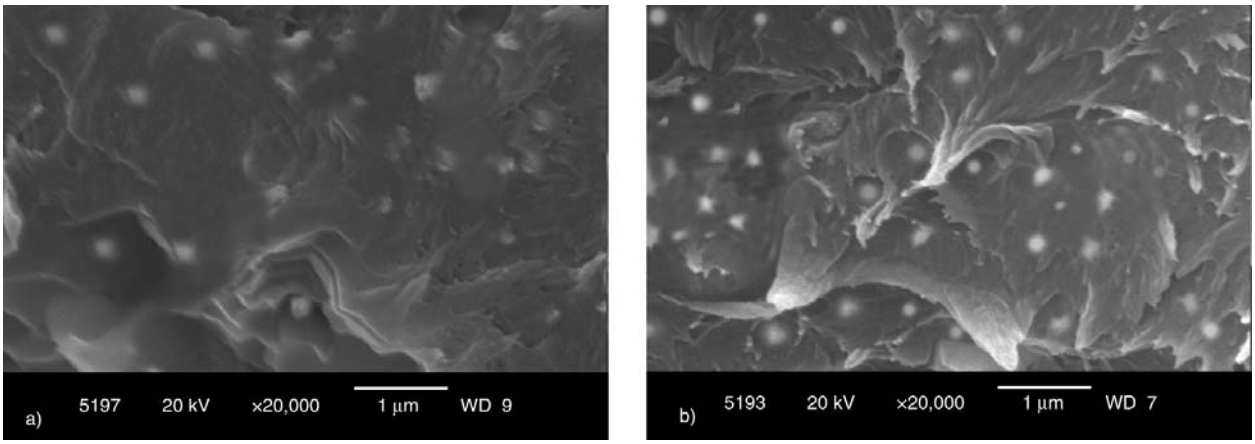

Figure 7. Fracture surface image of BNN10 (a) and BNN40 (b) (magnification (20 000))

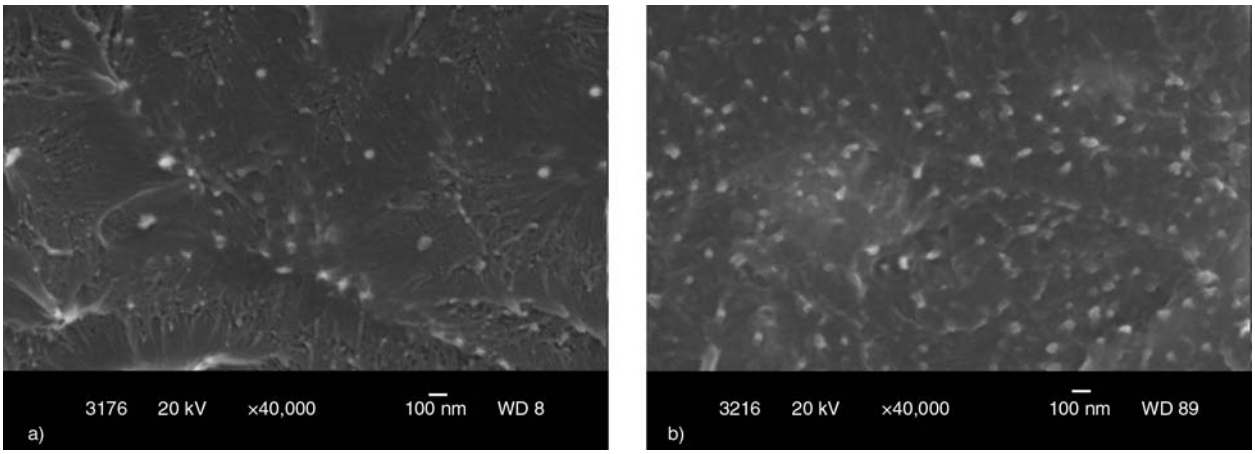

Figure 8. Fracture surface image of BNN10 (a) and BNN40 (b) (magnification (40 000))

PS composites, the active ceramic phase is not self-connected and the passive polymer phase is connected by the three dimensions by maintaining the (0-3) connectivity. The particle dispersion and particle-matrix reinforcement play vital roles for both tensile and elongation properties of the composites. In all pictures it is seen that all the particles are neatly coated with PS. The ceramic particles are dispersed homogeneously with the interspaces filled with PS at all magnification level, and large defects are not observed. Figures 6–8a and 6–8b showed a dense microstructure and is believed to have affected the mechanical properties of the composites. The size of the dispersed particle can be

calculated by counting a large number of particles from various micrographs of different magnification and quantitatively analyzed in terms of their diameter [26].

The number average particle diameter is given by Equation (4):

$$\frac{\sum N_i D_i}{N_i} = \overline{D}_n \tag{4}$$

The weight average particle diameter is given by Equation (5):

$$\frac{\sum N_i D_i^2}{\sum N_i D_i} = D_w \tag{5}$$

The volume average particle diameter is given by Equation (6):

$$\frac{\sum N_i D_i^3}{\sum N_i D_i^2} = D_v \tag{6}$$

where N_i is the number of particles having diameter D_i. The polydispersity index, a measure of particle size distribution and it is calculated as Equation (7):

$$\frac{D_w}{D_n} = PDI \tag{7}$$

The calculated polydispersity index is less than 1.2, reported in Table 5 and the value gives clear evidences for the good dispersion of filler in the matrix [27].

3.1.6. Density calculations

The first second and third column of Table 6 reports the density pattern of the prepared composites.

Table 5. Particle diameter measurement [nm]

Name of sample	Number average	Weight average	Volume average	PDI
BNN10	65.47	78.36	89.79	1.196
BNN40	52.50	61.25	84.96	1.166

The theoretical density values are calculated using the rule of mixtures [28] (Equation (8)):

$$\rho_c = \rho_p (1 - v_1) + \rho_f v_1 \tag{8}$$

where ρ_c is the density of the composite, ρ_p is the density of phase 1(polymer phase), ρ_f is the density of phase 2(ceramic phase) and v_1 is the volume fraction of filler. The values of ρ_p and ρ_f are taken to be 1050 and 5950 kg·m^{-3} respectively. First and second column of Table 6 compares the average of the measured density values (by sample geometry and Archimedes methods) with theoretical values. As density measurements of BNN-PS, it is revealed that the composite pellets followed the rule of mixtures with respect to the constituent powders, so that no noticeable change in density is induced by the thermal processing [29].

3.2. Mechanical properties

3.2.1. Stress Strain Behavior

So many investigators discussed the mechanical property behavior of filled polymer systems. These reports reveal that the tensile modulus is the easiest property to estimate because it is a bulk property that depends primarily on the geometry, particle size distribution and concentration of the filler. The two principal parameters used to describe the mechanical behavior of polymers are stress and strain. In the initial stages of the stress, the strain increases linearly (Hookean region). Modulus is the ratio of the stress to strain in the linear region of the stress strain curve. It is well known that the modulus increases for a polymer when mineral filler is incorporated into it. The exact nature of the tensile response of a polymeric material depends upon the chemical structure of the polymer, conditions of the sample preparation, molecular weight, molecular weight distribution, and the extend of any cross linking or branching [30].

At normal temperature and pressure, polystyrene exhibits an increase in stress with increasing strain

Table 6. Some representative properties of the composites

Name of the sample	Theoretical density [kgm^{-3}]	Observed density [kgm^{-3}]	Ultimate stress [MPa]	Young's modulus [GPa]
Polystyrene	1050	1050	36.61±0.5	2.89±0.02
BNN10	1542	1538	45.68±0.35	3.60±0.04
BNN20	2033	2030	54.75±0.45	4.31±0.02
BNN30	2524	2516	64.12±0.5	5.18±0.03
BNN40	3014	3010	72.15±0.35	5.68±0.03

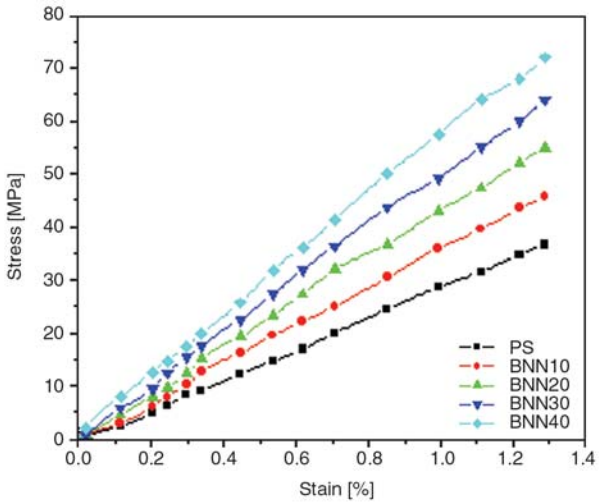

Figure 9. Stress strain behavior of polystyrene nanocomposites

up to the point of sample failure. The stress at failure is called ultimate stress or stress at break. Typical value of modulus and ultimate stress of the PS and composites are reported in the Table 6.

A very good linear fit is obtained for all the curves in Figure 9, with 99.77% correctness by origin plot indicates a relatively homogeneous distribution of filler particles in the matrix; structure related phenomena (change of matrix properties by the introduction of the filler, much aggregation, and segregation of particles during processing) seem to be absent in the composites.

3.2.2. Theoretical modeling

The mechanical properties of two-phase composites made up of a continuous polymer phase and particulate filler phase have been studied in great detail. As a result a variety of models are available to describe the modulus, tensile strength, and elongation at break as a function of filler volume fraction. The modeling and simulation of polymer-based composites has become an important topic in recent times because of the need for the development of these materials for engineering applications.

The mechanical properties of particulate filled composites are affected by a number of parameters such as filler orientation, particle size of the filler and filler-matrix adhesion etc. The load transfer from matrix to filler in a composite is strongly related to optimum mechanical properties of the composites.

Several theories have been proposed to model the tensile modulus of 'the non-interactive' composite materials in terms of different parameters. Among the most prominent, historically and technically are those developed by Einstein [31, 32], with and without adhesion, Kerner [33], and Sato and Furukawa [34]. Modified Kerner equation is an upper bound one while considering adhesion between filler and polymer. Einstein and Sato and Furukawa models are calculated with various adhesion parameters.

Einstein equation (with out adhesion parameter) (Equation (9)):

$$M_c = M_m(1+v_1) \tag{9}$$

where M_c and M_m are the Young's modulus of the composite and the matrix respectively and v_1 the filler volume percentage.

Einstein equation (with adhesion parameter) (Equation (10)):

$$M_c = M_m(1+2.5\cdot v_1) \tag{10}$$

where the constant 2.5 is accounted for adhesion between filler and polymer.

Kerner equation:

Kerner equation can be used to estimate the modulus (Equation (11)):

$$M_c = M_m\left[1+\frac{v_1 15(1-r)}{V_m(8-10r)}\right] \tag{11}$$

where V_m is the matrix volume fraction and r is the Poisson's ratio of the matrix. For expansible polymers incorporating rigid spherical particles featuring adhesion, the Kerner equation can be used to estimate the modulus.

Sato and Furukawa:

Sato and Furukawa have developed an expression (Equations (12) and (13)) for the modulus for the case where the adhesion is taken as a parameter:

$$M_c = M_m\left[\left(1+\frac{v_1^{2/3}}{2-2v_1^{1/3}}\right)(1-\psi j)-\frac{v_1^{2/3}\psi j}{(1-v_1^{1/3})v_1}\right] \quad (12)$$

$$\psi = \left(\frac{v_1}{3}\right)\frac{1+v_1^{1/3}-v_1^{2/3}}{1-v_1^{1/3}+v_1^{2/3}} \quad (13)$$

where v_1 is the volume fraction of filler j is the adhesion parameter, $j = 1$ for poor adhesion, and $j = 0$ for perfect adhesion. It can be seen (from Figure 10) that the experimental results are placed in between Kerner and Sato Furukawa relations with perfect adhesion.

All these predictions assume that the matrix and filler have an appreciable degree of physical interaction only. The polymer matrix is stiffened by the particulate filler. In most conventionally filled polymer systems the modulus increases linearly with the filler volume fraction. The enhancement of the modulus for BNN-PS may not be attributed simply by the introduction of the high modulus inorganic filler to PS matrix.

The increase of modulus is mainly governed by the particle size of the filler [35]. With Sato and Furukawa relations Young's modulus can be calculated with different adhesion parameters such as the value of adhesion parameter $j = 1$ for poor adhesion, $j = 0.5$ for medium adhesion and $j = 0$ for good adhesion. The result obtained with adhesion parameter ($j = 0$) is closely fitted with the experimental curve evidenced that this type of perfect adhesion is the cause of increment in both Young's modulus and tensile strength of the composites as in Figure 10.

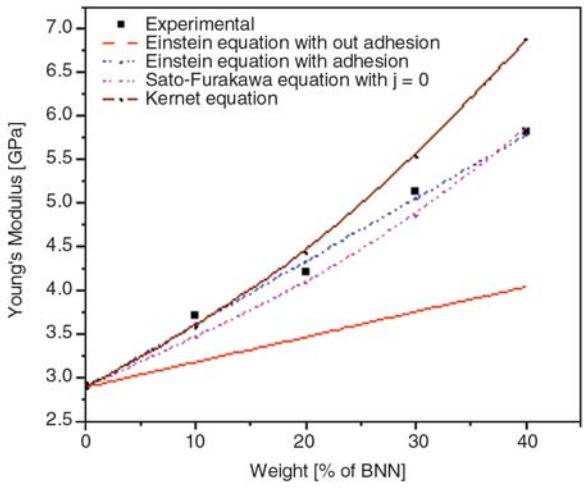

Figure 10. Theoretical modeling of the tensile modulus of BNN-PS composites with different adhesion parameters

3.2.3. Tensile strength

The tensile strength of a filled polymer is more difficult to predict because it depends strongly on local polymer filler interactions. Tensile strength is the force required to pull the composite to the point where it breaks. Specifically the tensile strength of a material is the maximum amount of tensile stress that it can be subjected to before failure. Brittle materials, such as PS, do not have a yield point, which means that ultimate strength and breaking strength are same.

The effect of volume fraction of BNN on tensile strength of the composites is given in Table 6. The virgin PS shows a tensile strength of around 36 MPa, coincides with its reported values [36]. Tensile strength of the composites increases with BNN filler loading. One problem in particulate-filled composites is the poor stress transfer at the filler-polymer interface because of the non-adherence of the filler to the polymer. The nanocomposites showed an increment in its ultimate stress value. In heterogeneous polymer systems the mechanism of micromechanical deformations and consequently, the macroscopic properties of the polymers are determined by local stress distribution around the inclusions. Because the adherence of filler to polymer in BNN-PS composites, the filler particles are able to carry any load, making it a strong body. Stress distribution will be created around the particles, increasing the composite strength further.

3.2.4. Theoretical modeling of tensile stress

A simple model was used by Lubin [37] for the determination of tensile stresses in unfilled and filled polymer with inclusions. It is assumed that at the composite tensile strength (ultimate tensile stress), the polymer has undergone maximum plastic deformation. Moreover, the load carried by the components corresponds to their effective cross-sections occupied in the specimen, *i.e.* $(1–1.21v_1^{2/3})$ for the matrix and $(1.21v_1^{2/3})$ for the inclusions, where v_1 is the volume fraction of inclusions in the composites [38]. If it is assumed that the average

stress acting across the surface of the fillers is £*, the Equation (14) must be valid:

$$£^* = £_m(1-1.21v_1^{2/3}) + £^*(1.21v_1^{2/3}) \quad (14)$$

where £ and $£_m$ are the composite and matrix tensile stresses, respectively. The load carried by the filler (£*) is always very much smaller than the matrix tensile stress when the filler with large particle size is used, *i.e.* debounding takes place. When the specific surface area of the filler is larger (smaller particles), £* can significantly exceed the tensile strength of the matrix. Considering the composition-dependence of tensile stress of composites including adhesion parameter Pukánszky [39] arrived the following relation (Equation (15)):

$$£=£_m\left(\frac{1-v_1}{1+2.5v_1}\right)\exp(Bv_1) \quad (15)$$

where B is an empirical parameter characterizing the degree of particle matrix reinforcement. It increases with specific surface area and the adhesive strength of the filler polymer interphase. The value of the parameter is found out by plotting tensile strength of the composites with filler volume fraction and linear fitting the experimental data as in Figure 11. The value of B is 4.69. An increased modulus is a well known fact in particulate filled micro composites. But an increment in tensile modulus associated with an increment in tensile strength is reported as the peculiarity of the nano composites [40]. These results show that the small BNN particles enable both relatively good dispersion and improved interfacial stress transfer in BNN-PS composites. In contrast with the tensile modulus, theoretical predictions of the tensile strength are less highly developed.

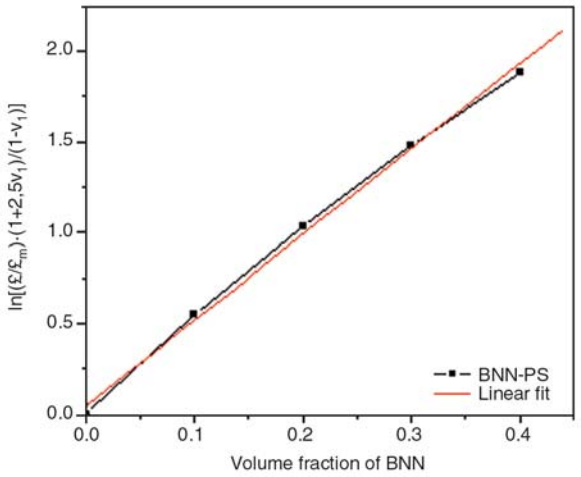

Figure 11. Adhesion parameter from the tensile stress of BNN-PS composites

3.2.5. Elongation at break

Normally addition of rigid particulate fillers to a polymer matrix decreases the elongation at break (strain at break). Only in rare instances, if there is a good reinforcement between polymer and the filler, the fracture goes from particle to particle rather than following a direct path, and these filled polymers have nearly equal elongations at break when compared with neat polymer. BNN-PS composites show the trend of perfect adhesion by the elongation at break value. Elongation at break value of BNN-PS composites is almost same as that of neat PS showing the good reinforcement between the filler and the matrix. A basic model that describes the elongation at break given by Equation (16) [41–43]:

$$€ = €_m(1-v_1^{1/3}) \quad (16)$$

where € and $€_m$ are the elongations at break of the composites and the unfilled polymer, respectively. For the case of perfect adhesion, under the assumption that the polymer breaks at the same elongation in the filled system as in the neat polymer. By Equation (15) it is believed that in the case of poor adhesion, the elongation is expected to decrease more gradually with filler loading.

4. Conclusions

Polycrystalline BNN ceramic powder with particle size less than 100 nm has been synthesized using conventional ceramic technique. The morphology and tensile behavior of BNN-PS composites are studied in detail. The most fascinating property of the composites is the relatively good dispersion of the filler particles in the matrix. The particle dispersion and particle-matrix reinforcement play vital roles for both tensile and elongation properties of the composites. Young's modulus and tensile strength of polystyrene show an increment by the incorporation of BNN filler. Elongation at break value of the composites is same as that of neat PS showing the good reinforcement between the filler and the matrix and stress transfer at the filler-poly-

mer interface is effectively possible by the efficient dispersion and good adherence of the filler to polymer.

References

[1] Byrene M. T., McNamee W. P., Gun'ko Y. K.: Chemical functionalization of carbon nanotubes for the mechanical reinforcement of polystyrene composites. Nanotechnology, **19**, 415707–415714 (2008).
DOI: 10.1088/0957-4484/19/41/415707

[2] Jancar J., Kucera J.: Yield behaviour of polypropylene filled with $CaCO_3$ and $Mg(OH)_2$ 'zero' interfacial adhesion. Polymer Engineering and Science, **30**, 707–711 (1990).
DOI: 10.1002/pen.760301203

[3] Yoon C-B., Lee S-H., Lee S-H., Koh Y-H., Kim H-E., Lee K-W.: Piezoelectric multilayer ceramic/ polymer composite transducer with 2-2 connectivity. Journal of the American Ceramic Society, **89**, 2509–2513 (2006).
DOI: 10.1111/j.1551-2916.2006.01080.x

[4] Psarras G. C.: Nanodielectrics: An emerging sector of polymer nanocomposites. Express Polymer Letters, **2**, 460 (2008).
DOI: 10.3144/expresspolymlett.2008.55

[5] Dekkers M. E., Heikens D.: The effect of interfacial adhesion on the tensile behavior of polystyrene-glass-bead composites. Journal of Applied Polymer Science, **28**, 3809–3815 (1983).
DOI: 10.1002/app.1983.070281220

[6] Smay J. E., Cesarano S., Tuttle B. A., Lewis J. A.: Piezo electric properties of 3-X periodic $Pb(Zr_xTi_{1-x})O_3$-polymer composites. Journal of Applied Physics, **92**, 6119–6127 (2002).
DOI: 10.1063/1.1513202

[7] Pradhan D. K., Choudhary R. N. P., Samantaray B. K.: Studies of structural, thermal and electrical behavior of polymer nanocomposite electrolytes. Express Polymer Letters, **2**, 630–638 (2008).
DOI: 10.3144/expresspolymlett.2008.76

[8] Tjong S. C.: Structural and mechanical properties of polymer nanocomposites. Material Science and Engineering: Reports, **53**, 73–197 (2006).
DOI: 10.1016/j.mser.2006.06.001

[9] Nanda M., Tripathy D. K.: Physico-mechanical and electrical properties of conductive carbon black reinforced chlorosulfonated polyethylene vulcanizates. Express Polymer Letters, **2**, 855–865 (2008).
DOI: 10.3144/expresspolymlett.2008.100

[10] Hameed N., Thomas S. P., Abraham R., Thomas S.: Morphology and contact angle studies of poly(styrene-*co*-acrylonitrile) modified epoxy resin blends and their glass fibre reinforced composites. Express Polymer Letters, **1**, 345–355 (2007).
DOI: 10.3144/expresspolymlett.2007.49

[11] Panda A. B., Pathak A., Pramanik P.: Low temperature preparation of nanocrystalline solid solution of strontium-barium-niobate by chemical process. Material Letters, **52**, 180–186 (2002).
DOI: 10.1016/S0167-577X(01)00389-5

[12] Thakur A. K., Prahan D. K., Samantaray B. K., Choudhary R. N. P.: Studies on an ionically conducting polymer nanocomposite. Journal of Power Sources, **159**, 272–276 (2006).
DOI: 10.1016/j.jpowsour.2006.04.096

[13] Jamieson P. B., Abraham S. C., Bernstein J. L.: Ferroelectric tungsten bronz-type crystal structures I. Barium sodium niobate. Journal of Chemical Physics, **48**, 5048–5060 (1968).
DOI: 10.1063/1.1668176

[14] Gaudet J., Taveres A. C., Transati S., Guay D.: Physicochemical characterization of mixed RnO_2–SnO_2 solid solutions. Chemistry of Materials, **17**, 1570–1579 (2005).
DOI: 10.1021/cm048129l

[15] Bruneel E., Persyn F., Hoste.: Mechanical and superconducting properties of BiPbSrCaCuO–PE and BiPbSrCaCuO–MgO composites. Superconductor Science and Technology, **11**, 88–93 (1998).
DOI: 10.1088/0953-2048/11/1/018

[16] Vollenberg P. H. T., Heikens D.: Particle size dependence of the Young's modulus of filled polymers: 1. Preliminary experiments. Polymer, **30**, 1656–1665 (1989).
DOI: 10.1016/0032-3861(89)90326-1

[17] Saq'an S. A., Ayesh A. S., Zihlif A. M., Martuscelli E., Ragosta G.: Physical properties of polystyrene-alum composites. Polymer Testing, **23**, 739–745 (2004).
DOI: 10.1016/j.polymertesting.2004.04.008

[18] Sharatsingh N. K., Sharma N.: X-ray – A boon for elemental analysis. Resonance, **10**, 60–69 (2005).
DOI: 10.1007/BF02895795

[19] Calligaris M., Silvanio G.: Powder diffraction package verson 1.1. in 'Proceedings of third international school and workshop of rystallography on X-ray powder diffraction and its applications' Cairo, Egypt, 456–470 (1990).

[20] Zuo R., Granzow T., Lupascu D. C., Rödel J.: PMN-PT ceramics prepared by spark plasma sintering. Journal of the American Ceramic Society, **90**, 1101–1106 (2007).

[21] Warren B. E.: X-ray diffraction in random layer lattice. Physical Review, **59**, 693–698 (1941).
DOI: 10.1103/PhysRev.59.693

[22] Mori S., Yamamoto N., Koyama Y., Uesu Y.: Evolution of a ferroelastic domain structure in an incommensurate phase of barium sodium niobate ($Ba_2NaNb_5O_{15}$). Physical Review B, **52**, 6158–6165 (1995).
DOI: 10.1103/PhysRevB.52.6158

[23] Panajkar M. S., Phatak G. M., Gangadharan K., Gopalakrishnan I. K., Gopinathan C.: Preparation of high Tc-superconducting ceramic/polymer composites using gamma radiation. Journal of Material Science Letters, **16**, 218–220 (1997).
[24] Lee W. E., Arshad S. E., James P. F.: Importance of crystallization hierarchies in microstructural evolution of silicate glass-ceramics. Journal of American Ceramic Society, **90**, 727–737 (2007). DOI: 10.1111/j.1551-2916.2006.01479.x
[25] Newnham R. E.: Structure – Property relations. Springer-Verlag, Berlin (1975).
[26] Bliznakov E. D., White C. C., Shaw M. T.: Mechanical properties of blends of HDPE and recycled urea-formaldehyde resin. Journal of Applied Polymer Science, **77**, 3220–3227 (2000). DOI: 10.1002/1097-4628(20000929)77:14<3220::AID-APP250>3.0.CO;2-4
[27] Ray D. A.: On the modulus of particulate filled composites: Application of van der Poel's equation. Journal of Polymer Science Polymer Physics, **14**, 2073–2082 (2003). DOI: 10.1002/pol.1976.180141112
[28] Satish B., Sridevi K., Vijaya M. S.: Study of piezoelectric and dielectric properties of ferroelectric PZT-polymer composites prepared by hot-press technique. Journal of Physics D: Applied Physics, **35**, 2048–2050 (2002). DOI: 10.1088/0022-3727/35/16/321
[29] Huang Q-W., Wang P-L., Cheng Y-B., Yan D-S.: XRD analysis of formation of strontium barium niobate phase. Materials Letters, **56**, 915–920 (2002). DOI: 10.1016/S0167-577X(02)00637-7
[30] Prashantha K., Soulestin J., Lacrampe M. F., Claes M., Dupin G., Krawczak P.: Multi-walled carbon nanotube filled polypropylene nanocomposites based on masterbatch route: Improvement of dispersion and mechanical properties. Express Polymer Letters, **2**, 735–745 (2008). DOI: 10.3144/expresspolymlett.2008.87
[31] Cowie J. M. G.: Polymers: Chemistry and physics of modern materials. Nelson Thornes Ltd., Cheltenham (2000).
[32] Nielsen L. E., Landel R. F.: Mechanical properties of polymers and composites. Hanser Publishers, New York (1992).
[33] Selvin T. P., Kuruvilla J., Sabu T.: Mechanical properties of titanium dioxide filled polystyrene microcomposites. Material Letters, **58**, 281–289 (2004). DOI: 10.1016/S0167-577X(03)00470-1
[34] Ehrig R.: Plastic recycling. Hanser, New York (1992).
[35] van Krevelan D. W.: Properties of polymers: Their correlation with chemical structure. Elsevier, Amsterdam (1972).
[36] Joel R .F.: Polymer Science and Technology. Prentice-Hall of India, New Delhi (2000).
[37] Lubin G.: Handbook of composites. van Nostrand Reinhold, London (1982).
[38] Shang S. W., Williams J. W., Söderholm K-J. M.: Using the bond energy density to predict the reinforcing ability of a composite. Materials Science, **27**, 4949–4956 (1992). DOI: 10.1007/BF01105259
[39] Pukánszky B.: Particulate filled polypropylene: Structure and properties. in 'Polypropylene: Structure, blends and composites' (ed. Karger-Kocsis J.) Chapman and Hall, London, Vol 3, 1–70 (1995).
[40] Vollenburg P. H. T., de Haan J. W., van de Ven L. J. M., Heikens D.: Particle size dependence of the Young's modulus of filled polymers: 2. Annealing and solid-state nuclear magnetic resonance experiments. Polymer, **30**, 1663–1665 (1989). DOI: 10.1016/0032-3861(89)90327-3
[41] Nielsen L. E., Landel R. F.: Mechanical properties of polymers and composites. Marcel Dekker, New York (1994).
[42] Thomas S. P., Thomas S., Abraham R., Bandyopadhyay S.: Polystyrene/calcium phosphate nanocomposites: Contact angle studies based on water and methylene iodide. Express Polymer Letters, **2**, 528–538 (2008). DOI: 10.3144/expresspolymlett.2008.63
[43] Luo J-C., Wen H-C., Wuz W-F., Chou C-P.: Mechanical research of carbon nanotube/PMMA- composite films. Polymer Composites, **29**, 1285–1290 (2008). DOI: 10.1002/pc.20388

eXPRESS Polymer Letters Vol.3, No.3 (2009) 190–199
Available online at www.expresspolymlett.com
DOI: 10.3144/expresspolymlett.2009.24

Morphology and properties of polypropylene/ethylene vinyl acetate copolymer/wood powder blend composites

D. G. Dikobe, A. S. Luyt*

Department of Chemistry, University of the Free State (Qwaqwa Campus), Private Bag X13, Phuthaditjhaba, 9866, Republic of South Africa

Received 25 Novenber 2008; accepted in revised form 16 February 2009

Abstract. Polypropylene (PP) was blended with ethylene vinyl acetate copolymer (EVA) to form PP/EVA polymer blends. Wood powder (WP) was mixed into these blends at different weight fractions (50/50/0, 45/45/10, 40/40/20, 35/35/30 w/w PP/EVA/WP) to form PP/EVA/WP blend composites. The morphology, as well as thermal and mechanical properties, of these composites were investigated. The scanning electron microscopy (SEM) and differential scanning calorimetry (DSC) results confirm the immiscibility of EVA and PP in the blends, and show that WP is primarily concentrated in the EVA phase. DSC results further show that the EVA crystallization behaviour is significantly influenced by the presence of WP. Dynamic mechanical analysis (DMA) results confirm immiscibility of PP and EVA, as well as an interaction between EVA and WP. Interaction between EVA and WP was further confirmed by Fourier-Transform infrared spectroscopy (FTIR). TGA results show that the blend composite degradation was also influenced by the presence of WP.

Keywords: *polymer composites, polymer blends, polypropylene, ethylene vinyl acetate copolymer, wood powder*

1. Introduction

Polymer blending, which is a very important technique in industrial practices, is performed to achieve specific properties such as improved mechanical properties that individual materials do not possess [1, 2]. Polymers can be blended directly by simply mixing them under specific conditions, or by using appropriate compatibilizers. Polymer blending has the following advantages: cheap, easily processable, and specific properties can be achieved depending on the composition and preparation methods [1–4].

PP is one of the most important commodity polymers and is used in many areas, such as home appliances, automotive parts, construction and other important industrial applications. PP's applications are often limited due to its low impact strength and Young's modulus properties, particularly at low temperatures and high temperature loading conditions. Blending PP with different polymers is an economic and effective way to improve these drawbacks [5–8].

EVA with different VA contents (16 and 28 wt%) have been blended with PP to enhance PP's low impact strength. The following observations on PP/EVA blending have already been reported [5, 9, 10]:

– Two melting peaks and two glass transition peaks were observed indicating that PP/EVA blends are thermodynamically immiscible and also technologically non-compatible.
– A co-continuous phase was observed in blends with an EVA content of 50 wt% or higher.
– A mechanical locking interphase was found if the blend was kept below the crystallization temperature of PP.

*Corresponding author, e-mail: dikobedg@qwa.ufs.ac.za

– Partial compatibility was achieved by the addition of a crosslinking agent.
– EVA acts as a good impact modifier.
– When a PP/EVA blend was irradiated, chain scission was initiated in the PP phase, while crosslinking prevailed in the EVA phase.

Most polymer blends are immiscible on a molecular scale and form heterogeneous systems that affect their properties. One way of improving the properties of the blends is to introduce fillers into the systems [11–13]. Addition of fillers is favoured because it is a cheap, effective and a fast method to modify the properties of the base material. The degree of improvement often depends on the type of the filler (synthetic or natural), particle size and shape, filler content, and surface treatment which promotes interaction between the filler and the polymer matrix [5, 7].

The need for non-toxic and environmentally friendly materials favours the use of natural fibres, over inorganic and synthetic fillers, as fillers in polymeric materials. Dikobe and Luyt [14] and other researchers used lignocelluosic fillers as reinforcing material in different polymer matrices [15–20].

Although there is extensive literature on the use of natural fillers in single polymers [14–18, 21–26], there are only a few studies dealing with polymer blends filled with natural fillers. Espert *et al*. [20] compared water absorption of natural cellulosic fibres from wood and one-year crops in polypropylene composites, as well as their influence on the mechanical properties of the composites. They reported that the use of a post-consumer polypropylene with a low percentage of EVA in its composition in some cases leads to improved resistance to water absorption and better mechanical properties, and that EVA can further improve the compatibility between the fibres and the matrix.

The purpose of this study was to investigate the morphology and properties of PP/EVA binary blends and PP/EVA/WP polymer blend composite ternary systems. The paper reports on the effect of WP content on the morphology and properties of the polymer blend. We were interested in establishing the location of WP in these composites, and how this would influence the thermal and mechanical properties of these systems.

2. Materials and methods

PP, supplied by Sasol Polymers, South Africa, has a density of 0.90 g·cm^{-3}, a melting point of 165°C, a tensile strength of 30 MPa and a melt flow index of 12 g/10 min (230°C, 2.16 kg). EVA with 9% vinyl acetate (VA) content, supplied by Plastamid, Elsies River, South Africa, has a density of 0.93 g·cm^{-3}, a melting point of 95°C, melt flow index of 2.5 g/10 min (80°C; 2.16 kg), a tensile strength of 19 MPa and a 750% elongation at break. Pine WP, or pine saw dust, was obtained from FBW Taurus, Phuthaditjhaba, South Africa. WP, supplied as a light orange coloured powder with a density of 1.5 g·cm^{-3} was dried at 120°C for 48 hours. Particles with sizes ≤150 μm were obtained by sieving the dried WP using laboratory test sieves of 150 μm pore size.

Blends and blend composites were weighed according to the required ratios (100/0/0, 0/100/0, 50/50/0, 45/45/10, 40/40/20 and 35/35/30 w/w PP/EVA/WP) to make up a total of 38 g (which is the mass required for thoroughly mixing the different components in the Brabender Plastograph mixer). Mixing of the samples was done at a temperature of 180°C and a mixing speed of 30 rpm for 15 minutes. The samples were then melt pressed at 190°C and 100 bar for 3 minutes. The pressed samples were allowed to cool at room temperature for 10 minutes before touching them to avoid air from penetrating, which would promote the formation of bubbles.

DSC analyses were carried out in a Perkin Elmer DSC7 differential scanning calorimeter (Wellesley, Massachusetts, USA) under flowing nitrogen (20 ml·min^{-1}). Samples with masses of approximately 7.5 mg were heated from 25 to 190°C at a rate of 10°C·min^{-1} in order to eliminate the thermal history, cooled to 25°C at 2°C·min^{-1} and reheated under the same conditions. For each sample the melting and crystallization data were obtained from the second scan.

The morphologies of the 50/50 w/w PP/EVA blend and the 40/40/20 w/w PP/EVA/WP composite were examined using a Shimadzu 5SX-550 Superscan scanning electron microscope. The samples were immersed in liquid nitrogen to ensure perfect breakage. The fractured surface was sputter coated with gold dust (60 nm) before viewing.

A careful separation of the polymers was performed by selective Soxhlet solvent extraction. The EVA in the 50/50 w/w PP/EVA blend and the 40/40/20 w/w PP/EVA/WP blend composite were extracted using n-heptane at 20°C for 24 hours. The residues from these samples were dried in an oven at 50°C for 24 h. The dried samples were sputter coated with gold dust (60 nm) and SEM micrographs were obtained using a Shimadzu 5SX-550 Superscan scanning electron microscope.

For DMA analysis, rectangular samples of 20 mm×5 mm×0.5 mm were used. A Perkin Elmer Diamond DMA was used for the evaluation of the storage modulus, loss modulus and mechanical damping factor. The temperature range over which the properties were measured was –100 to 100°C at a heating rate of 5°C·min^{-1} under 30 ml·min^{-1} flowing nitrogen. The tests were carried out at a frequency of 1 Hz.

FTIR microscopy was performed using a Perkin Elmer Precisely Multiscope. Very thin samples were placed under the microscope, and microscope photos as well as FTIR spectra of the desired areas were collected. The samples were scanned using a Perkin Elmer Spectrum 100 FTIR spectrometer over 400–4000 cm^{-1} at a resolution of 4 cm^{-1}.

Thermogravimetric analyses (TGA) were carried out on a Pelkin-Elmer TGA7 thermogravimetric analyzer. Samples having a mass of approximately 7 mg were heated from 25 to 600°C at 20°C·min^{-1} under flowing nitrogen (20 ml·min^{-1}).

Tensile testing was performed under ambient conditions on a Hounsfield H5KS universal tester at a cross-head speed of 50 mm·min^{-1}. Tensile test specimens (gauge length 24 mm, width 5 mm, thickness 2 mm) were prepared using a dumbbell shaped hollow die punch. Six samples per composition were analysed. A statistics computer programme was used to eliminate out-of-range values, and the mean of the accepted values was reported. The tensile strength, Young's modulus, and elongation at break values were obtained from this testing.

3. Results and discussion

The DSC curves in Figure 1 show endothermic melting peaks at 99°C for EVA and 165°C for PP. The PP/EVA blend has two melting peaks at 99 and 168°C, indicating immiscibility of EVA and PP. The WP blend composites show a decrease in EVA melting point to 86°C, while the PP melting point remains around 166°C. Decreasing amounts of EVA and PP gave rise to decreasing melting enthalpies (Table 1). This was to be expected, since the melting enthalpies are related to the amounts of polymer in the sample, and since the amounts of polymer decrease with increasing WP content in the sample, the melting peak sizes and related enthalpies should correspondingly decrease. It is, however, possible that the presence of solid filler may influence the crystallization behaviour of either or both polymers, and it was decided to compare the experimentally observed enthalpy values with calculated enthalpy values. These values were calculated assuming that the composites were com-

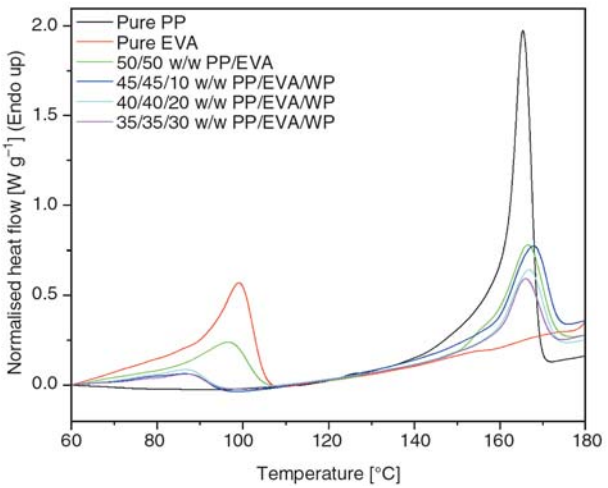

Figure 1. DSC heating curves of pure EVA, pure PP and PP/EVA/WP blend composites

Table 1. DSC melting data for pure PP, pure EVA and their blend composites (2°C·min^{-1} cooling)

PP/EVA/WP [w/w]	T_{Peak} [°C]		ΔH_{obs} [J·g^{-1}]		ΔH_{calc} [J·g^{-1}]	
	EVA	PP	EVA	PP	EVA	PP
100/0/0	–	165.3 ± 7.3	–	82.3 ± 4.2	–	82.3 ± 4.2
0/100/0	99.3 ± 3.5	–	54.2 ± 1.2	–	54.2 ± 1.2	–
50/50/0	99.7 ± 2.4	168.1 ± 6.4	26.9 ± 1.5	38.7 ± 3.1	27.1 ± 2.6	41.2 ± 0.9
45/45/10	85.5 ± 2.9	167.5 ± 6.2	10.2 ± 1.2	35.8 ± 3.4	24.4 ± 2.4	37.0 ± 0.5
40/40/20	86.1 ± 3.2	166.9 ± 5.4	9.8 ± 0.7	31.4 ± 2.5	21.7 ± 1.4	32.7 ± 0.5
35/35/30	86.2 ± 3.6	165.8 ± 4.3	6.7 ± 0.5	26.9 ± 1.9	18.9 ± 1.2	28.8 ± 0.9

pletely homogeneous and that neither blending nor the presence of WP changed the crystallization characteristics of either polymer. Table 1 shows that there is a good correlation between the experimentally observed and theoretically calculated enthalpies for both PP and EVA in the 50/50 w/w PP/EVA blend. This confirms that a completely immiscible blend was formed, and that neither polymer had an influence on the crystallization behaviour of the other polymer. Further support for this may be found in the fact that there was also very little change in the melting peak temperatures of the two polymers after blending.

In the PP/EVA/WP composites, the experimentally observed enthalpies for EVA melting were significantly lower than the calculated values. In comparison, the experimentally observed and calculated enthalpy values for PP melting are almost the same for all three investigated composites (Table 1). The peak temperatures of PP melting in the composites are also not significantly different from those of pure PP and blended PP, while those of EVA in the composites are significantly lower than those of pure EVA and blended EVA. This shows that WP is situated primarily in the EVA phase and strongly interacts with EVA. As a result of this interaction, the EVA chains are immobilized by the WP particles, which results in a reduced crystallization of EVA. This conclusion is supported by the positions of the crystallization peaks in Figure 2 that are at significantly lower temperatures for EVA. It has been reported [20] that the addition of cellulosic material to a PP/EVA blend causes a decrease in crystallization, melting and oxidation temperatures, and an insignificant increase in crystallinity of the blend. However, the authors of this paper did not distinguish between the PP and EVA phases in the blend. Salemane and Luyt [15] reported an increase in crystallinity of PP in the presence of WP, and in the absence of a compatibilizer [15].

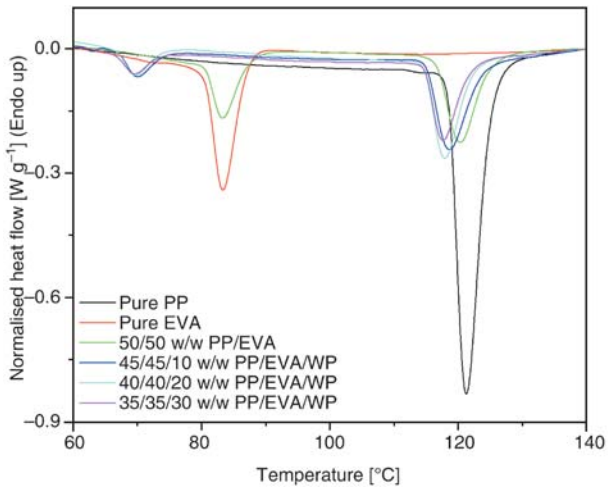

Figure 2. DSC cooling curves of pure EVA, pure PP and PP/EVA/WP blend composites

The SEM photos of the fracture surfaces of the 50/50 w/w PP/EVA blend before and after extraction are shown in Figure 3. Figure 3a shows that it is not possible to see separate PP and EVA phases on the SEM photo of the 50/50 w/w PP/EVA blend; this is in line with observations by Mihaylova *et al.* [9], who used SEM to study the supramolecular structures of PP/EVA blends. Their SEM microphotographs of the unirradiated blends show that in EVA-rich blends, EVA was the continuous phase, while PP was identified as spherical particles within the blend. When PP was the major phase, PP

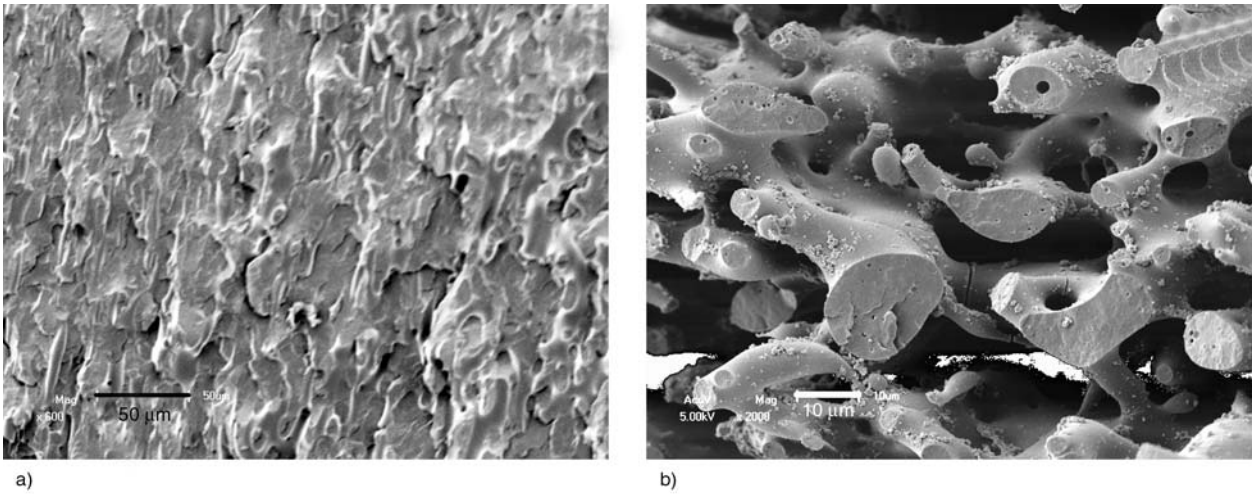

Figure 3. SEM pictures of the fracture surfaces of 50/50 w/w PP/EVA a) before extraction and b) after extraction (2000× magnification)

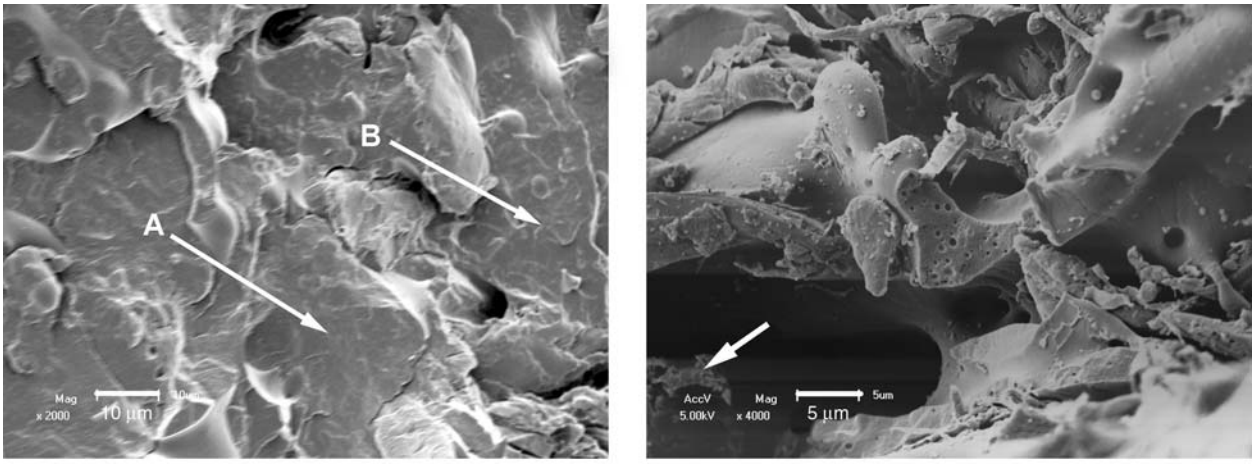

Figure 4. SEM pictures of the fracture surfaces of 40/40/20 w/w PP/EVA/WP a) before extraction and b) after extraction (2000× magnification)

formed the continuous phase, while EVA showed partially coalesced droplets. However, the authors found it difficult to distinguish the two components in the 50/50 w/w PP/EVA blend; although the images could show brittle surfaces (related to PP) and regions where plastic deformations (related to rubbery EVA) have occurred. This finding suggested a co-continuous structure for the 50/50 w/w PP/EVA sample. Gupta *et al.* [27], in a similar study on PP/EVA blends, observed the same behaviour. The SEM photo of our 50/50 w/w PP/EVA blend, after extraction in *n*-heptane, clearly confirms this co-continuous structure (Figure 3b).

The SEM photo (Figure 4a) of the 40/40/20 w/w PP/EVA/WP blend composite before extraction shows WP particles intimately covered by a polymer (arrow *A*), which probably is EVA (according to the DSC observations). Although the two polymers are not distinguishable in the photo, it may be assumed with some certainty that the smooth phase (arrow *B*) consists primarily of PP. The arrow in the SEM photo of the *n*-heptane extracted 40/40/20 w/w PP/EVA/WP blend composite clearly shows the loose WP particle in the hole left by the extracted EVA (Figure 4b). This confirms that the WP particles were primarily located in the EVA phase of the immiscible blend.

DMA storage modulus and damping factor curves of all the investigated samples are shown in Figures 5 and 6. Figure 5 shows that at low temperatures EVA has slightly lower storage moduli than PP, but the difference becomes more significant

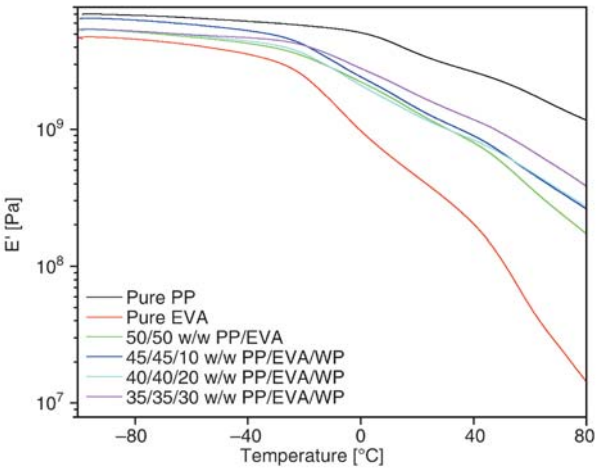

Figure 5. Storage modulus as function of temperature of pure EVA, pure PP, and PP/EVA/WP blend composites

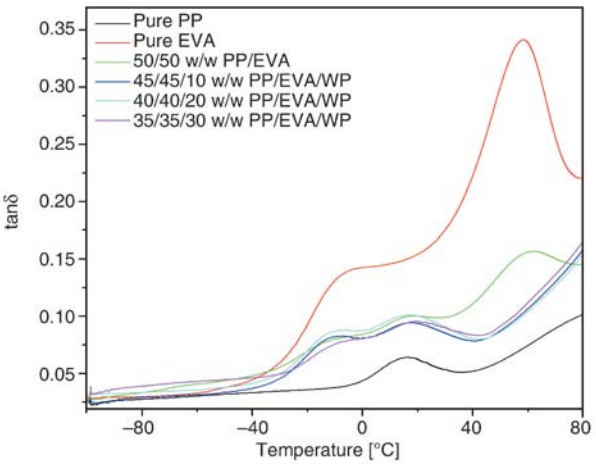

Figure 6. tanδ as function of temperature of pure EVA, pure PP, and PP/EVA/WP blend composites

with increasing temperature. The PP/EVA polymer blend and the WP blend composites have storage moduli between those of pure EVA and pure PP over the whole temperature range. It is interesting that the presence of wood powder does not seem to significantly change the storage moduli, probably because it is concentrated in the EVA phase. The damping factor curve of EVA shows two different transitions, the β-transition at about 0°C and the α-transition at about 58°C (Figure 6). The β-transition corresponds to the glass transition of EVA. PP has a β-transition peak at about 16°C. This transition corresponds to the glass transition of the amorphous region in PP [1, 22]. The PP/EVA blend shows all the characteristic peaks of pure PP and pure EVA, indicating complete immiscibility of the two components. In the case of the PP/EVA/WP blend composites, the α-transition of EVA is no longer visible, which shows that the interaction between EVA and WP has a significant influence on the interlamellar shear properties of EVA.

Figures 7 and 8 show the FTIR microscopy photo of the 40/40/20 w/w PP/EVA/WP blend composite and the FTIR spectra of pure PP, pure EVA, a 50/50 w/w PP/EVA blend and a 40/40/20 w/w PP/EVA/WP blend composite. The FTIR microscopy photo of the 40/40/20 w/w PP/EVA/WP composite in Figure 7 shows the formation of three separate phases, a dark area, a darker interface and a light area. FTIR analysis of the light areas gave a spectrum corresponding to that of PP (Figure 8). This observation confirms that WP has no affinity for PP. The dark (a) and interfacial (b) areas gave spectra corresponding to that of 40/

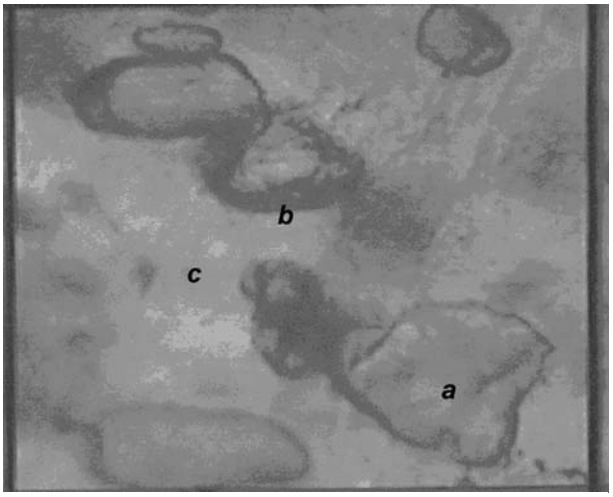

Figure 7. FTIR microscope photo of the 40/40/20 w/w PP/EVA/WP blend composite

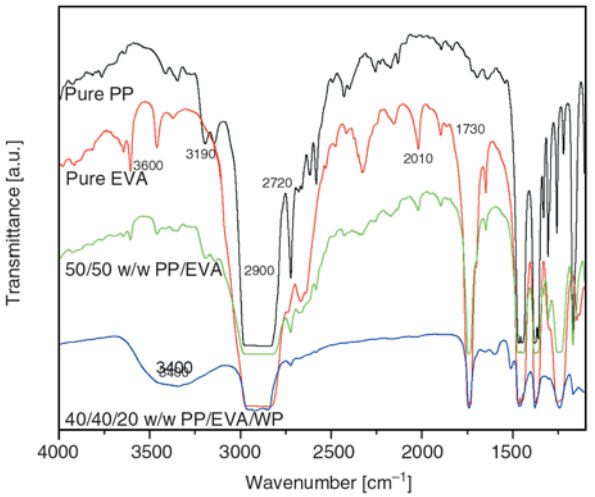

Figure 8. FTIR spectra of pure EVA, pure PP and PP/EVA/WP blend composites

40/20 w/w PP/EVA/WP. The spectrum shows the –OH peak (around 3400 cm^{-1}), indicating the presence of WP, while the other peaks are characteristic peaks of EVA and not PP (Figure 8). All the spectra show strong absorbance peaks around 2850 and 2920 cm^{-1} that are associated with the C–H asymmetric stretching of the polymers. The peak representing the vibration of the –C=O ester of the carboxyl group appears at 1750 cm^{-1} in pure EVA, the PP/EVA blend and the PP/EVA/WP blend composite. The fact that the PP/EVA blend spectrum shows all the characteristic peaks for pure EVA and pure PP, and that no new peaks are observed, indicate the absence of any reaction or interaction between EVA and PP, which supports the SEM, DSC and DMA observations. The lack of vibrational changes in PP/EVA compared to pure PP and pure EVA was also reported by Huerta-Martinez *et al.* [5], who indicated that the vibrational changes of the carbonyl group would be noticed only in miscible blends. The presence of WP in the blend composite is indicated by a strong, broad –OH functional group stretching vibration around 3400 cm^{-1}. The –C=O peak at 1750 cm^{-1} in the blend composite is much less intense than that in pure EVA and the PP/EVA blend, probably as a result of the –C=O interaction with the –OH in WP. Thermogravimetric analysis (TGA) was used to investigate the thermal stability and degradation of PP, EVA, the PP/EVA blend and the PP/EVA/WP blend composites. The TGA and derivative TGA curves of these samples are shown in Figures 9 and 10. EVA (with two degradation steps) is ther-

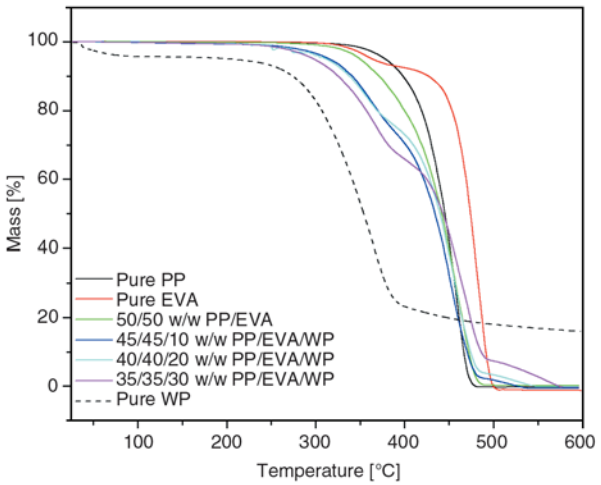

Figure 9. TGA curves of pure EVA, pure PP, WP and PP/EVA/WP blend composites

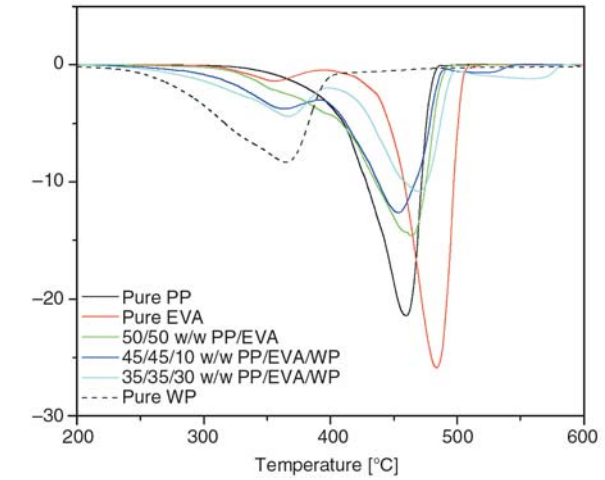

Figure 10. Derivative TGA curves of pure EVA, pure PP, PP/EVA blend, WP and PP/EVA/WP blend composites

mally more stable than PP. However, the blend degrades at a slower rate than pure PP due to the influence of the more thermally stable EVA backbone. The blend composites show two degradation steps; the first one is atrributed to the degradation of WP combined with de-acetylation, and the second one is due to the degradation of PP and the EVA backbone. The onset temperatures of the first degradation step of the composites decrease and the intensities of the derivative peaks (Figure 10) increase as the WP content increases. The second degradation step of the composites starts at higher temperatures than that for the 50/50 w/w PP/EVA blend. This may be attributed to the interfacial interaction between WP and the EVA part of the PP/EVA blend. Qui *et al.* [23] studied the structure and properties of composites of highly crystalline cellulose with PP, and reported that no significant change was observed in the thermal stability of PP in the presence of cellulose due to the lack of compatibility between the two. However, when the system was compatibilized with maleic anhydride grafted PP (MAPP), the thermo-oxidative stability of the PP/cellulose composites was enhanced due to the improvement in interfacial interaction between PP matrix and cellulosic filler, promoted by MAPP. Joseph *et al.* [26] also reported that the addition of short sisal fibre to PP yielded composites that are more thermally stable than the PP matrix. Another reason for the second degradation step starting at higher temperatures may be the retardation of the evaporation of volatile degradation products due to the char formed during the first degradation step. Peeterbroeck *et al.* [28] reported a delay in the thermal degradation with the addition of clay to EVA, mainly due to a decrease in the rate of evolution of the volatile products. Duquesne *et al.* [7] reported that the second degradation step (which corresponds to the decomposition of the polyethylenic fraction) in EVA-nanoclay systems occurred at a higher temperature in the presence of clay. This behaviour was attributed to a diffusion effect, which limited the emission of the gaseous degradation products, resulting in an increase in the thermal stability of the second degradation step of EVA.

The tensile properties of the blend and composites as a function of filler content are presented in Table 2. Generally, the filler plays an important

Table 2. Mechanical properties of PP/EVA/WP blend composites

PP/EVA/WP [w/w]	E ± sE [MPa]	$\varepsilon_b \pm s\varepsilon_b$ [%]	$\sigma_b \pm s\sigma_b$ [MPa]
100/0/0	498.5 ± 13.5	26.7 ± 2.5	29.9±1.3
0/100/0	38.2 ± 1.4	535 ± 12.3	9.9 ± 0.5
50/50/0	258 ± 3.5	12.9 ± 0.1	12.8 ± 0.1
45/45/10	265 ± 2.3	10.7± 0.1	8.9 ± 0.2
40/40/20	272 ± 3.7	9.7 ± 0.4	8.7 ± 0.1
35/35/30	285 ± 3.5	7.25 ± 0.1	7.6 ± 0.2

E – tensile modulus, ε_b – elongation at break, σ_b – tensile strength

role in determining the mechanical properties of lignocellulosic filled thermoplastics [1–5, 20, 26]. The tensile moduli of pure PP and pure EVA are 498 and 38 MPa respectively, and the modulus of the PP/EVA blend is an average of these values (Table 2). This is to be expected, because PP and EVA form a totally immiscible blend (see Figure 3), and the blend will have a tensile modulus to which both polymers contribute equally. Table 2 shows an increase in modulus of the composites with an increase in WP content, because rigid fillers normally increase the stiffness of a composite [23].

The PP/EVA blend has an elongation at break lower than those of the individual polymers, because the interfaces between the two non-compatible polymers form defect points where stress cracking will occur more easily. A further decrease in elongation at break was experienced with increasing WP content, which is normal for these types of composites [13, 18, 19, 23]. It is commonly explained as being due to the restriction in chain mobility of the matrix, and to the filler particles acting as defect points.

The tensile strengths of the composite samples decrease with an increase in WP content. This is probably the result of WP particles locating themselves in the EVA phase. Although the WP has a greater affinity for EVA, and seems to preferably locate itself inside the EVA phase, there will not be enough EVA in the blends with high WP contents, and as a result a fair amount of WP particles may locate themselves at the EVA-PP interface. The tensile strengths of these composites will therefore decrease because of the weak interaction between WP and PP. Kim *et al*. [25] reported that the tensile strength of WP filled PP composites decreased with increasing bio-flour loading due to the weak interfacial adhesion and low compatibility between the hydrophilic bio-flour and hydrophobic PP.

4. Conclusions

PP/EVA/WP polymer blend composites were prepared and their morphology as well as thermal and mechanical properties were investigated. The PP/EVA blend shows immiscibility due to a lack of interaction between PP and EVA. SEM and FTIR microscopy shows in lack of homogeneity as indicated by island formation within the blend composite. In the blend composites the WP has a higher affinity for EVA than for PP. This significantly influenced the crystallization behaviour of EVA, which was clearly observed from both the DSC and DMA results. The presence of WP in the PP/EVA blend caused a decrease in the degradation temperature of the first degradation step, which is a combination of WP degradation and EVA de-acetylation. At the same time the degradation temperature of the second step increased, probably as a result of the strong interaction between WP and EVA combined with retardation in the evolution of volatile degradation products. The stress and the strain at break of the blend composites decreased with an increase in WP content, while the modulus increased.

Acknowledgements

The National Research Foundation in South Africa (TTK2006052300007) and the University of the Free State are acknowledged for financial support of the project.

References

[1] Jayanarayan K., Thomas S., Joseph K.: Morphology, static and dynamic mechanical properties of in situ microfibrillar composites based on polypropylene/poly(ethylene terephthalate) blends. Composites Part A: Applied Science and Manufacturing, **39**, 164–175 (2008).
DOI: 10.1016/j.compositesa.2007.11.008

[2] Yu L., Dean K., Li L.: Polymer blends and composites from renewable sources. Progress in Polymer Science, **31**, 576–602 (2006).
DOI: 10.1016/j.progpolymsci.2006.03.002

[3] Si X., Guo L., Wang Y., Lau K-T.: Preparation and study of polypropylene/polyethylene terephthalate composite fibres. Composites Science and Technology, **68**, 2943–2947 (2008).
DOI: 10.1016/j.compscitech.2007.11.008

[4] Lou C-W., Lin W-L., Lei C-H., Su K-H., Hsu C-H., Liu Z-H., Lin J-H.: PET/PP blends with bamboo charcoal to produce functional composites. Journal of Materials Processing Technology, **192–193**, 428–433 (2007).
DOI: 10.1016/j.jmatprotec.2007.04.018

[5] Huerta-Martinez B. M., Ramirez-Vargas E., Medellin-Rodrequez F. J., Garcia R. C.: Compatibility mechanisms between EVA and complex impact heterophasic PP-EP*x* copolymers as a function of EP content. European Polymer Journal, **41**, 519–525 (2005).
DOI: 10.1016/j.eurpolymj.2004.10.021

[6] Albano C., Reyes J., Ichazo M., Gonzalez J., Chipara M. I.: Influence of gamma irradiation on the thermal stability of blends with previously treated sisal fibre. Polymer Degradation and Stability, **73**, 225–236 (2001).
DOI: 10.1016/S0141-3910(01)00036-2

[7] Duquesne S., Jama C., Le Bras M., Delobel R., Recourt P., Gloaguen J. M.: Elaboration of EVA-nanoclay systems-characterization, thermal behaviour and fire performance. Composites Science and Technology, **63**, 1141–1148 (2003).
DOI: 10.1016/S0266-3538(03)00035-6

[8] Liu Y., Kontopoulou M.: The structure and physical properties of polypropylene and thermoplastic olefin nanocomposites containing nanosilica. Polymer, **47**, 7723–7731 (2006).
DOI: 10.1016/j.polymer.2006.09.014

[9] Mihaylova M. D., Nedkov T. E., Krestev V. P., Kresteva M. N.: Supermolecular structures of poly(propylene-co-ethylene)/poly(ethylene-co-acetate) blends irradiated with fast electrons. SEM, SAXS and DSC studies. European Polymer Journal, **37**, 2177–2186 (2001).
DOI: 10.1016/S0014-3057(01)00118-5

[10] Mihailova M., Kresteva M., Aivazova N., Krestev V., Nedkov E.: X-ray investigation of polypropylene and poly(ethylene-co-vinyl acetate) blends irradiated with fast electrons: WAXS investigation of irradiated i-PP/EVA blends. Radiation Physics and Chemistry, **56**, 581–589(1999).
DOI: 10.1016/S0969-806X(97)00292-2

[11] Suarez J. C. M., Coutihno F. M. B., Sydentricker T. H.: SEM studies of tensile fracture surfaces of polypropylene-sawdust composites. Polymer Testing, **22**, 819–824 (2003).
DOI: 10.1016/S0142-9418(03)00017-5

[12] Premphet K., Horanont P.: Phase structure of ternary polypropylene/elastomer/filler composites: Effect of elastomer polarity. Polymer, **41**, 9283–9290(2000).
DOI: 10.1016/S0032-3861(00)00303-7

[13] Uotila R., Hippi U., Paavola S., Seppala J.: Compatibilization of PP/elastomer/ microsilica composites with functionalized polyolefins: Effect on microstructure and mechanical properties. Polymer, **46**, 7923–7930 (2005).
DOI: 10.1016/j.polymer.2005.06.099

[14] Dikobe D. G., Luyt A. S.: Effect of poly(ethylene-co-glycidyl methacrylate) compatibilizer content on the morphology and physical properties of ethylene vinyl acetate-wood fiber composites. Journal of Applied Polymer Science, **104**, 3206–3213 (2007).
DOI: 10.1002/app.26080

[15] Salemane M. G., Luyt A. S.: Thermal and mechanical properties of polypropylene-wood powder composites. Journal of Applied Polymer Science, **100**, 4173–4180 (2006).
DOI: 10.1002/app.23521

[16] Lundqiust L., Marque B., Hagstrand P-O., Leterrier Y., Manson J-A. E.: Novel pulp fibre reinforced thermoplastic composites. Composites Science and Technology, **63**, 137–152 (2003).
DOI: 10.1016/S0266-3538(02)00192-6

[17] Harper D., Wolcott M.: Interaction between coupling agent and lubricants in wood-polypropylene composites. Composites Part A: Applied Science and Manufacturing, **35**, 385–394 (2004).
DOI: 10.1016/j.compositesa.2003.09.018

[18] Felix J. M., Gatenholm P.: Effect of transcrystalline morphology on interfacial adhesion in cellulose/polypropylene composites. Journal of Materials Science, **29**, 3043–3049 (1994).
DOI: 10.1007/BF01117618

[19] Menyhárd A., Varga J.: The effect of compatibilizers on the crystallisation, melting and polymorphic composition of β-nucleated isotactic polypropylene and polyamide 6 blends. European Polymer Journal, **42**, 3257–3268 (2006).
DOI: 10.1016/j.eurpolymj.2006.09.003

[20] Espert A., Vilaplana F., Karlsson S.: Comparison of water absorption in natural cellulosic fibres from wood and one-year crops in polypropylene composites and its influence on their mechanical properties. Composites Part A: Applied Science and Manufacturing, **35**, 1267–1276 (2004).
DOI: 10.1016/j.compositesa.2004.04.004

[21] Keener T. J., Stuart R. K., Brown T. K.: Maleated coupling agents for natural fibre composites. Composites Part A: Applied Science and Manufacturing, **35**, 357–362 (2004).
DOI: 10.1016/j.compositesa.2003.09.014

[22] Qiu W., Zhang F., Endo T., Hirotsu T.: Preparation and characterization of composites of high crystalline cellulose with polypropylene: Effect of maleated polypropylene and cellulose content. Journal of Applied Polymer Science, **87**, 337–345 (2003).
DOI: 10.1002/app.11446

[23] Qui W., Endo T., Hirotsu T.: Structure and properties of composites of highly crystalline cellulose with polypropylene molecular weight: Effects of polypropylene molecular weight. European Polymer Journal, **42**, 1059–1068 (2006).
DOI: 10.1016/j.eurpolymj.2005.11.012

[24] Bledzki A. K., Gassan J.: Composites reinforced with cellulose based fibres. Progress in Polymer Science, **24**, 221–274 (1999).
DOI: 10.1016/S0079-6700(98)00018-5

[25] Kim H-O., Lee B-H., Choi S-W., Kim S., Kim H-J.: The effect of maleic anhydride-grafted polypropylene (MAPP) on the interfacial adhesion properties of bio flour filled polypropylene composites. Composites Part A: Applied Science and Manufacturing, **38**, 1473–1482 (2007).
DOI: 10.1016/j.compositesa.2007.01.004

[26] Joseph P. V., Joseph K., Thomas S., Pillai C. K. S., Prasad V. S., Groeninckx G., Sarkissova M.: The thermal and crystallization studies of short sisal fibre reinforced polypropylene composites. Composites Part A: Applied Science and Manufacturing, **34**, 253–266 (2003).
DOI: 10.1016/S1359-835X(02)00185-9

[27] Gupta A. K., Ratnam B. K., Srinivasan K. R.: Impact toughening of polypropylene by ethylene vinyl acetate copolymer. Journal of Applied Polymer Science, **45**, 1303–1312 (1992).
DOI: 10.1002/app.1992.070450718

[28] Peeterbroeck S., Alexandre M., Jérôme R., Dubois Ph.: Poly(ethylene-co-vinyl acetate)/clay nanocomposites: Effect of clay nature and organic modifiers on morphology, mechanical and thermal properties. Polymer Degradation and Stability, **90**, 288–294 (2005).
DOI: 10.1016/j.polymdegradstab.2005.03.023